

# **Silicon Photomultiplier Classification of the Pre-Production GCT Camera of CTA**

---

**Silicon Photomultiplier Klassifikation der Pre-Production GCT Kamera von CTA**

Master-Thesis von Ben Gebhardt aus Heidelberg

Tag der Einreichung:

1. Gutachten: Dr. Richard White (MPIK)
2. Gutachten: Prof. Jim Hinton (MPIK)
3. Gutachten: Prof. Tetyana Galatyuk (TU DA)



TECHNISCHE  
UNIVERSITÄT  
DARMSTADT

Fachbereich Physik  
Max Planck Institut für Kernphysik Heidelberg

**Silicon Photomultiplier Classification of the Pre-Production GCT Camera of CTA**  
**Silicon Photomultiplier Klassifikation der Pre-Production GCT Kamera von CTA**

Vorgelegte Master-Thesis von Ben Gebhardt aus Heidelberg

1. Gutachten: Dr. Richard White (MPIK)
2. Gutachten: Prof. Jim Hinton (MPIK)
3. Gutachten: Prof. Tetyana Galatyuk (TU DA)

Tag der Einreichung:

---

## Abstract

---

Earth is continuously hit by high energy gamma radiation that carries with it vast amounts of information about the most energetic phenomena in our galaxy and beyond. Part of this information is delivered to Earth in the form of a gamma ray induced particle shower in our atmosphere. While it is also possible to detect those particles directly on the ground, traveling through Earth's atmosphere those particles emit Cherenkov light. Particles in the shower produce a light cone that can be detected by telescopes on the ground. From the Cherenkov light, it is possible to reconstruct the direction and energy of the gamma ray.

One such experiment capable of observing gamma rays is the proposed Cherenkov Telescope Array. It consists of over 100 telescopes grouped in three energy ranges, deployed on two array sites, achieving whole-sky coverage. Different designs of the telescopes are able to use Silicon Photomultipliers (SiPMs) for photon detection. SiPMs are semiconductors that attracted increased attention for their possible use in astroparticle physics. Each detected photon entering the detector is converted to a measurable signal through avalanche creation. Being a fairly new technology, they are continuously being developed, and finding the most promising candidate is a task spread across many groups.

The aim of this thesis is to investigate important characteristics and their temperature dependence of five proposed candidate SiPMs for CTA. This thesis deals with developing an initial teststand for dark measurements, that can later be upgraded to support light measurements. This includes the development of data acquisition and analysis code, that are utilized to evaluate important characteristics of the candidates. Among them are the gain of a SiPM, being a measure for the signal strength through conversion of a photoelectron. The temperature dependence of the gain is important during observation, where the gain fluctuation is required to be low in order to avoid measurement errors. Other important characteristics this thesis examines are thermal and correlated noise and their potential temperature dependence. Thermal noise describes the event of a thermally induced incident in the photosensor without the presence of light. Correlated noise describes cross-talk between the photosensors mediated by avalanche photons diffusing to other photosensors. Both sources of noise have a direct impact on the single photon detection resolution of the detector, a vital parameter in gamma ray astronomy. In conclusion, the thesis compares the results of the measured devices via two methods among themselves and against results from involved groups, in order to find the most promising initial candidate.



---

## Abstract

---

Die Erde wird kontinuierlich von hoch energetischer Gammastrahlung getroffen, welche eine enorme Menge an Informationen über die energiereichsten Phänomene in unserer Galaxie und darüber hinaus enthält. Ein Teil dieser Information gelangt zur Erde durch Gammastrahlung induzierte Teilchenschauer in unserer Atmosphäre. Während es möglich ist diese Teilchen direkt am Erdboden zu messen, emittieren diese Teilchen solange sie durch die Atmosphäre fliegen Cherenkov Strahlung. Teilchen in einem Teilchenschauer produzieren einen Lichtkegel, welcher von Teleskopen am Erdboden detektiert werden kann. Mit Hilfe dieses Cherenkov Lichtes ist es möglich die Quelle und Energie der Gammastrahlung zu rekonstruieren.

Eines der Experimente, dass dazu im Stande ist Gammastrahlung zu observieren ist der vorgeschlagene Cherenkov Telescope Array. Dieser besteht aus über 100 Teleskopen, die nach ihrem Energiebereich eingeteilt sind, diese werden an zwei Standorten aufgebaut und sind dadurch in der Lage den ganzen Himmel zu observieren. Verschiedene Designs für die Teleskope sind in der Lage Silicon Photomultiplier (SiPM) als Photosensor zu nutzen. SiPM sind Halbleiter, die in der Astropartikelphysik erhöhte Beachtung finden. Jedes detektierte Photon, dass in den Detektor eintritt wird durch einen Lawinen-Effekt in ein messbares Signal umgewandelt. Es ist eine relativ neue Technologie, deshalb wird sie kontinuierlich weiterentwickelt, und den vielversprechendsten Kandidaten auszuwählen ist eine Aufgabe die auf viele Gruppen unterteilt ist.

Das Ziel dieser Thesis ist es wichtige Charakteristiken und ihre Temperaturabhängigkeit von fünf vorgeschlagenen SiPMs für CTA zu untersuchen. Diese Thesis befasst sich mit der Entwicklung eines anfänglichen Teststandes für Dunkel-Messungen, welcher in der Zukunft für Licht-Messungen erweitert werden kann. Damit verbunden ist die Entwicklung von Datenerfassungs- und Datenanalysesoftware, die verwendet werden um wichtige Charakteristiken der Kandidaten zu ermitteln. Darunter ist der Gain eines SiPM, welcher ein Maß für die Signalstärke beim konvertieren eines Photoelektrons darstellt. Die Temperaturabhängigkeit des Gain für ist wichtig während das Teleskop observiert, da die Fluktuation des Gain klein sein muss um Messfehler zu vermeiden. Weitere wichtige Charakteristiken, die diese Thesis untersucht, sind thermale und korrelierte Störgeräusche und ihre Temperaturabhängigkeit. Thermales Rauschen beschreibt den Vorgang wenn ein Photosensor ohne Anwesenheit von Licht und durch thermale Anregung ein Signal generiert. Korreliertes Rauschen beschreibt cross-talk zwischen Photosensoren ausgelöst durch ein Photon, dass in einen benachbarten Photosensor diffundiert. Die Störgeräusche haben einen direkten Einfluss auf die Einzelphotonenauflösung des Detektors, ein wichtiger Parameter in der Gammastrahlen-Astronomie. Zum Schluss vergleicht diese Thesis die Ergebnisse der gemessenen SiPM untereinander und mit Ergebnissen von externen Gruppen via zweier Methoden, um den erfolgversprechendsten Anfangskandidaten zu finden.

---



---

## List of Figures

---

1	Cosmic radiation . . . . .	7
2	Fermi LAT . . . . .	8
3	Cherenkov light cone . . . . .	10
4	GCT and CHEC-M at Meudon . . . . .	12
5	GCT optical system . . . . .	13
6	CHEC focal plane . . . . .	14
7	Structure and carrier multiplication through an avalanche inside a SiPM . . . . .	16
8	Cherenkov light spectrum . . . . .	18
9	Avalanche induced secondary effects . . . . .	21
10	Teststand outside view . . . . .	23
11	Thermal chamber inside view . . . . .	24
12	Experimental setup scheme . . . . .	25
13	Shaped versus unshaped signal . . . . .	26
14	Zero pole cancelation . . . . .	26
15	Multi p.e. persistence plot . . . . .	27
16	Pulse height spectrum generated by the oscilloscope . . . . .	27
17	Pedestal subtraction . . . . .	30
18	Peak Detection . . . . .	31
19	Fitted pulse area histogram . . . . .	32
20	Regression line plots of 1p.e. and $\Delta$ p.e. . . . .	33
21	MPD parameter challenges and the integration window . . . . .	35
22	MPD parameter challenges and the threshold . . . . .	36
23	List of examined SiPM devices . . . . .	38
24	CHEC-S SiPM . . . . .	40
25	CHEC-S average pulse shape . . . . .	40
26	CHEC-S gain . . . . .	41
27	CHEC-S DCR . . . . .	42
28	CHEC-S OCT . . . . .	43
29	LCT5 6mm SiPM . . . . .	45
30	LCT5 6mm average pulse shape . . . . .	45
31	LCT5 6mm gain . . . . .	46
32	LCT5 6mm DCR . . . . .	47
33	LCT5 6mm OCT . . . . .	48
34	LCT5 7mm SiPM . . . . .	49
35	LCT5 7mm average pulse shape . . . . .	49
36	LCT5 7mm gain . . . . .	50

---

37	LCT5 7mm DCR . . . . .	51
38	LCT5 7mm OCT . . . . .	51
39	LCT5 LVR 6mm SiPM . . . . .	53
40	LCT5 LVR 6mm average pulse shape . . . . .	53
41	LCT5 LVR 6mm gain . . . . .	54
42	LCT5 LVR 6mm DCR . . . . .	54
43	LCT5 LVR 6mm OCT . . . . .	55
44	SensL FJ60035 SiPM and average pulse shape . . . . .	56
45	SensL FJ60035 gain . . . . .	57
46	SensL FJ60035 DCR . . . . .	58
47	SensL FJ60035 OCT . . . . .	58
48	DCR device comparison . . . . .	60
49	OCT device comparison . . . . .	61
50	Comparison based on two proposed points of operation . . . . .	62
51	PDE versus OCT comparison . . . . .	64
52	CTA in Chile and the stereoscopic technique . . . . .	69
53	Current IACT experiments . . . . .	69
54	OCT dependency on the cell-size . . . . .	70
55	Pulse area spectra of three different integration windows . . . . .	73
56	S12642 pulse height and pulse area spectrum . . . . .	74
57	LCT5 6mm pulse area spectrum . . . . .	75
58	Breakdown-voltage versus temperature . . . . .	76
59	Breakdown-voltage dependency . . . . .	77
60	Full schematic of the shaper developed at the University of Leicester. With tuneable components C9 and R20 highlighted. . . . .	78
61	List of candidate SiPM devices . . . . .	79
62	CHEC-S pixel comparison of the gain . . . . .	80
63	CHEC-S pixel comparison of the DCR . . . . .	80
64	CHEC-S pixel comparison of the OCT . . . . .	81
65	Raw data pre analysis . . . . .	82
66	Peak detection level during analysis . . . . .	83
67	Number of peaks detected during analysis . . . . .	84
68	Integration window illustration . . . . .	85

---

## Contents

---

<b>1</b>	<b>Cosmic Radiation</b>	<b>7</b>
1.1	Air shower induced Cherenkov Radiation . . . . .	9
1.2	Imaging Atmospheric Cherenkov Telescopes . . . . .	10
<b>2</b>	<b>Cherenkov Telescope Array</b>	<b>12</b>
2.1	Gamma Cherenkov Telescope . . . . .	13
2.2	Compact High Energy Camera . . . . .	14
<b>3</b>	<b>Silicon Photomultipliers</b>	<b>16</b>
3.1	SiPM characteristics . . . . .	16
3.2	Gain of a Silicon Photomultiplier . . . . .	18
3.3	Thermally induced dark counts . . . . .	20
3.4	Avalanche-induced secondary effects . . . . .	20
3.5	Photon Detection Efficiency . . . . .	22
<b>4</b>	<b>Experimental Setup</b>	<b>23</b>
<b>5</b>	<b>Data Analysis</b>	<b>29</b>
5.1	Tracefile Conversion . . . . .	29
5.2	Pedestal Subtraction . . . . .	30
5.3	Peak Detection . . . . .	31
5.4	Gain Extraction . . . . .	32
5.5	Analysis improvements . . . . .	34
5.6	Data Challenges . . . . .	35
<b>6</b>	<b>Results</b>	<b>38</b>
6.1	SiPM devices for CTA . . . . .	38
6.2	Hamamatsu S12642-1616PA-50 50 $\mu$ m 3mm . . . . .	40
6.3	Hamamatsu LCT5 50 $\mu$ m 6mm . . . . .	45
6.4	Hamamatsu LCT5 75 $\mu$ m 7mm . . . . .	49
6.5	Hamamatsu IVR 50 $\mu$ m 6mm . . . . .	53
6.6	SensL FJ60035 6mm 35 $\mu$ m . . . . .	56
<b>7</b>	<b>Comparison</b>	<b>59</b>
7.1	Dark Count Rate . . . . .	59

---

---

7.2 Optical Cross Talk . . . . .	60
7.3 Point of Operation Comparison . . . . .	62
7.4 Photon Detection Efficiency . . . . .	63
<b>8 Conclusion and Outlook</b>	<b>65</b>
<b>9 Glossary</b>	<b>66</b>
<b>10 Bibliography</b>	<b>67</b>
<b>11 Appendix</b>	<b>69</b>

## 1 Cosmic Radiation

Cosmic rays consist of a single particle with energies from  $10^{10}$  to  $10^{20}$  eV and describes extra-solar charged particles arriving on Earth and hitting the atmosphere (fig(1)). The most energetic laboratory based accelerators operate in the  $10^{12}$  eV energy range. They were discovered by V.F. Hess in 1912 during the famous balloon flight experiments. He aimed to measure the conductivity of air, that until then, was believed to be an insulator resulting in some problems regarding the discharge of an electrically charged body, no matter how well it was isolated from the ground. Hess found the air's conductivity to increase with higher altitude, concluding the presence of a large amount of ionizing radiation above the atmosphere.

Cosmic rays do not include those low energy particles originating from our sun. With a particle energy up to 1 keV, those are referred to as solar wind, which means, by definition, cosmic rays arrive on Earth from outside our solar system. They consist of 87% protons, 12%  $\alpha$ -particles, 1% heavier nuclei and some electrons. High energy cosmic rays hitting Earth are very rare, averaging to one per year in an area of one square kilometer. Except at those very high energies ( $>10^{18}$  eV) cosmic rays will not reach earth directly and cannot be observed to pinpoint their source. Traveling through the interstellar medium, they get scattered by the interstellar magnetic fields, the cosmic microwave background and other hindrances and therefore have lost all directional information. However, directly observable cosmic rays, for example at the Pierre-Auger Observatory, provide an insight into cosmic particle accelerators.[2]

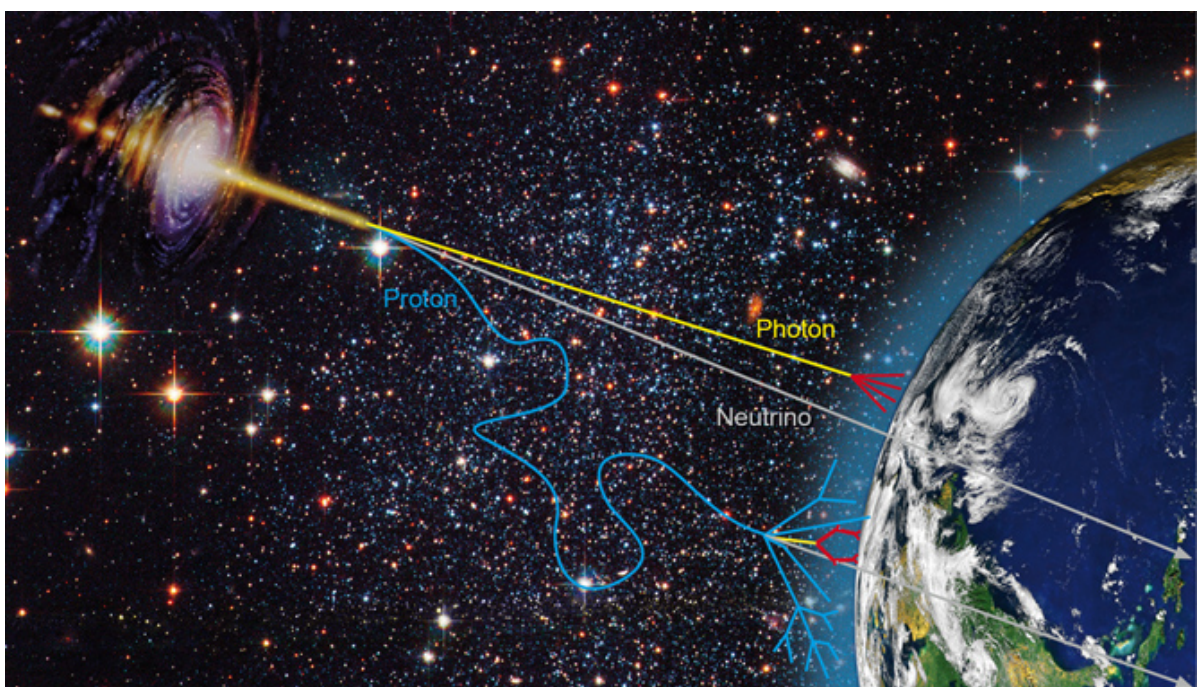


**Figure 1:** Gamma radiation photons (yellow) and scattered cosmic ray protons (blue) from an astrophysical source arriving on Earth. Neutrinos (grey) mostly do not interact. Picture from [25]

Cosmic rays of the higher energies are therefore observed via a detour: Gamma radiation.

Gamma radiation cannot be generated by thermal emission of hot stellar objects, the only event with a high enough temperature to produce thermal radiation in the range of GeV and TeV gamma radiation would be the big bang, there is and has been nothing else in the known universe. If thermal radiation reflects the temperature of the emitting body, what do gamma rays tell us?



**Figure 2:** FermiLAT Picture from [26]

Gamma radiation probe a non-thermal universe. In this other mechanisms are needed to concentrate large amounts of energy into a single quantum. The possible emission mechanisms are outlined below.

There are many diverse mechanisms of emitting gamma radiation. Gamma rays are generated by high relativistic particles, in a first step for example: accelerated by the shockwave of a supernova explosion. Those cosmic rays then collide with ambient gas, interact with photons or magnetic fields, by inverse Compton scattering, emitting high energy photons in a down-top fashion. Very-high-energy (VHE) gamma radiation is defined as gamma radiation in the energy range of  $10^{11}$  to  $10^{14}$  eV.

One such source of VHE gamma radiation and also the most famous, because the first to be discovered, lies within the Crab Nebula. The Neutron Star located inside the Crab Nebula is a Pulsar and the remnant of Supernova1054 and steadily emits gamma radiation energies up to 80 TeV. Another compound of the gamma radiation here is the so called Pulsar Wind Nebula. It is composed of highly relativistic charged particles from the Pulsars giant rotating magnetic field interacting with the expanding Supernova remnant via inverse Compton scattering. Supernova shockwaves themselves can also drive atomic nuclei to high energies which in turn emit observable gamma-rays in a top-down fashion. Additionally, binary systems consisting of a black hole or pulsar orbiting a massive star can emit a flow of high-energy particles with varying intensity, based on the elliptical orbit, where particle acceleration conditions vary.

Just like thermal radiation reflects the temperature of the emitting object, the flux and energy spectrum of the gamma rays reflect the flux and spectrum of the high energy seed particles, coming from the source. So they can be used to trace these cosmic rays and electrons in distant regions of our own galaxy or even beyond. [1]

One surprise was the discovery of so called "dark sources" , objects emitting VHE gamma-rays,

but have no counterpart in other wavelengths, meaning those objects might only be observable through gamma-rays. In extragalactic regions, gamma rays provide information on active galaxies, where a constant stream of gas feeds a supermassive black hole at the center, releasing enormous amounts of energy. From there, gamma rays are believed to be emitted, giving insight into one of the most violent but to date poorly understood environments in our universe.

Even higher energy gamma rays could also be the product of decays of heavy particles, like dark matter or cosmic strings. They therefore also provide a window to the discovery of dark matter.

Gamma Radiation carries unique information about the most energetic phenomena in our universe. The only problem is, our atmosphere is opaque for gamma radiation, gamma ray astronomy in the lower energies is done by satellite based instruments like FermiLAT. The Large Area Telescope, the principle scientific instrument on the Fermi Gamma-Ray Space Telescope Spacecraft sensitive in the energy range between 20 MeV and 100 GeV, launched in June 2008 fig(2). To reach the higher energy range through space based telescopes is very inconvenient, since the required mass the telescope active area would need to detect the gamma rays increases with gamma ray energy, and can therefore be very expensive to launch into space. Low energy gamma rays can be efficiently captured by a volume appropriate for a spacecraft, for higher energy gamma rays using other interaction and detection media, like water or Earth's atmosphere, is more viable.

---

## 1.1 Air shower induced Cherenkov Radiation

---

The effect of gamma radiation on Earth is visible through gamma-ray induced particle cascades. When a primary particle, i.e. a gamma photon or cosmic ray enters the atmosphere and collides with a nucleus of the air, it gets scattered and creates secondary electrons, positrons and photons. Those secondary particles also interact with the atmosphere creating a cascade of particles called a particle shower.

In this air shower, the initial and each subsequent particle traveling through our atmosphere emits Cherenkov light. Cherenkov radiation is a phenomenon caused by charged particles traveling faster than the local speed of light would allow in that medium. This light is emitted in a narrow cone with an increasing angle as the particles travel downward. This Cherenkov light shows as a very short ( $\sim 5\text{ns}$ ) flash with a peak in the UV-spectrum at around 330nm. Thus, we can image the particle cascade measured with the telescope and can reconstruct the direction and energy through a stereoscopic image of the shower taken by multiple telescopes (see section(A)), reconstructing the position of the source in the sky. It is also possible to reconstruct the energy of the original photon from the amount of light produced, because energy is conserved, so all energy of the original photon is now distributed between the particles of the shower.

To determine whether it is a hadronic shower, originating from cosmic rays, or a gamma shower, originating from gamma ray photons, the shape of the shower and so called Hillas parameters are used to determine the difference.

## 1.2 Imaging Atmospheric Cherenkov Telescopes

The technique, pioneered by the Wipple Collaboration, behind the ground based experiments called Imaging Atmospheric Cherenkov Telescope (IACTs) aims at measuring the time, direction and energy of flashes of Cherenkov light from extensive air showers caused by VHE gamma radiation.

Those ground based instruments have a much larger effective detection area than any satellite based instrument, which have a typical detection size of  $1\text{m}^2$ . The range of the Cherenkov flash being between 300-600nm, current generation Silicon Photomultipliers (SiPMs) are a promising candidate to replace the progenitor photon detector used in previous experiments like HESS, the Photomultiplier Tube (PMT).

Current ground based IACT experiments are HESS, MAGIC and Veritas. (see section(B)) HESS<sup>1</sup>, based in Namibia, consists of four telescopes the size of 12 m operating in the energy range of 3 GeV to 100 TeV. The chosen name is in honor of Victor Hess, the first to discover cosmic rays. The recent HESS upgrade added a fifth larger telescope in the center of the array with a mirror diameter of 28 m. MAGIC<sup>2</sup>, based in La Palma one of the Canary Islands, is a system consisting of two 17 m diameter telescopes at 2200m asl<sup>3</sup>, covering the energy range 30 GeV and 30 TeV. Veritas<sup>4</sup>, operating between 50 GeV - 50 TeV consists of four 12 m telescopes, based in Arizona, USA.

Due to the limited effective area, caused by the number of telescopes spread over a wide area, most cascades are viewed by only 2 or 3 of the telescopes. Additionally, due to the low flux of VHE gamma radiation, detectors for this energy range are spread over a large area, mak-

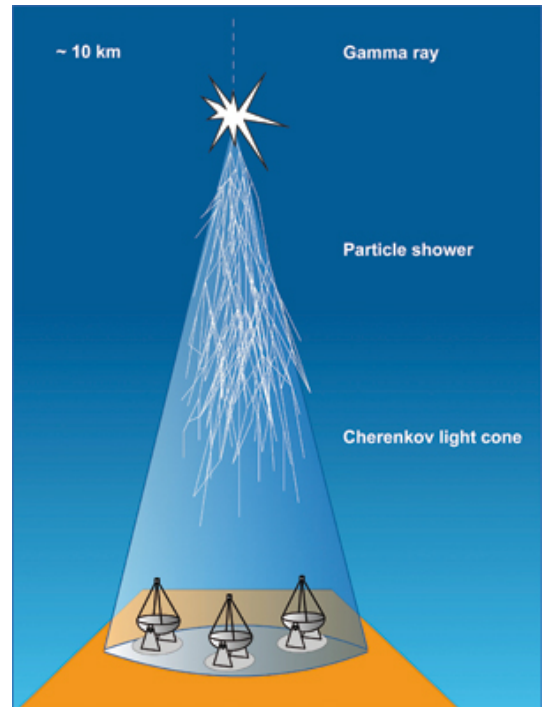


**Figure 3:** The cone of Cherenkov light emitted by an extensive air shower. Picture from [27]

<sup>1</sup> High Energy Stereoscopic System

<sup>2</sup> Major Atmospheric Gamma Imaging Cherenkov Telescopes

<sup>3</sup> above sea level

<sup>4</sup> Very Energetic Radiation Imaging Telescope Array System

---

ing space based instruments, which detect the incident gamma ray, an inconvenient and costly choice.

Another detection concept for VHE gamma radiation are ground based air shower particle detectors such as the High-Altitude-Water-Cherenkov observatory (HAWC) [6]. It employs a similar detection principle, recording shower particles reaching arrays of ground based particle detectors filled with water as detection medium, in contrast to air in IACTs. Those have the advantage of a larger duty cycle than IACTs, as they are able to operate during the day. Their limited sensitivity even with high observation time however will not allow them to compete with the sensitivity and resolution of IACTs such as in the CTA. The array will however be able to provide useful complementary information.

## 2 Cherenkov Telescope Array

The Cherenkov Telescope Array, CTA, is a proposed ground-based observatory array of many tens of telescopes distributed over a larger energy range than before. It will allow detection of gamma rays over a large area on the ground and from multiple different directions. The array will consist of 60 - 100 telescopes of different designs and sizes to cover the aimed for energy range and area. Science goals of CTA are the understanding of cosmic rays and their role in the universe, including the study of cosmic particle accelerators, such as pulsars, pulsar wind nebulae , supernova remnants and gamma ray binaries. Secondly particle acceleration around black holes of supermassive or stellar size and lastly physics beyond the Standard Model. There are currently three groups of telescopes planned, differing in their size and achievable energy range:[2]



**Figure 4:** The prototype GCT Structure with mounted CHEC-M at the Observatory at Meudon, Paris, one of the telescopes of CTA.

1. LST<sup>5</sup> The low energy instrument, between 20 and 200 GeV, is a 23 meter class telescope with a moderate field of view (FoV) of the order of about 4.5°.
2. MST<sup>6</sup> The medium energy range, from around 100 GeV to 10 TeV, is covered by a telescope of the 12 meter class with a FoV of 7°.
3. SST<sup>7</sup> The high energy instrument, operating between a few TeV to 300 TeV, is a 4 meter telescope with a FoV ranging from 9.1° to 9.6°.

There are currently two sites planned, which when deployed, will achieve full-sky coverage. The southern site in the Atacama Desert in Chile, one of the most driest and isolated regions on Earth, will consist of four LSTs, 24 MSTs, and about 70 SSTs covering an area of 4 km<sup>2</sup>. The

<sup>5</sup> LST large sized telescope

<sup>6</sup> MST medium sized telescope

<sup>7</sup> SST small sized telescope

northern site will only cover  $0.4 \text{ km}^2$  and will only contain four LSTs and 15 MSTs due to spacing reasons with the MAGIC observatory at the same location at the Roque de los Muchachos Observatory on La Palma, one of the Canary Islands.

One proposed concept for the SST is the Gamma Cherenkov Telescope (GCT) (fig(4)).

## 2.1 Gamma Cherenkov Telescope

The reflector design of IACTs traditionally consists of multiple mirror segments, which focus the incident light onto a camera covering  $\sim 1 \text{ m}$  with pixels  $1'' - 1.5''$  in diameter. Such a reflector design is proposed for both, the LST and the MST of CTA resulting in the telescope sizes mentioned in section(2) above, that will use the traditional PMTs.

For the SST such a design would result in a cheap telescope structure, but a disproportionately expensive camera, i.e. the cost and size of the structure is reduced, while the cost of the camera is not. The cost of one SST camera would be near the cost of a MST camera, which given the

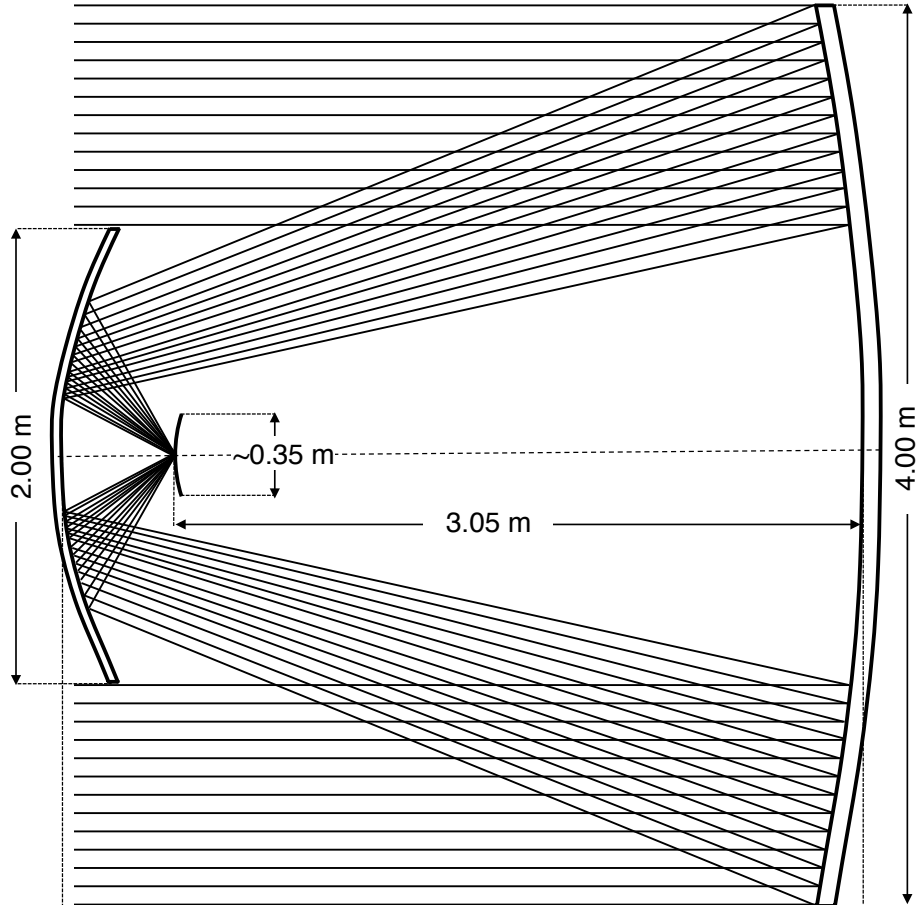


**Figure 5:** Optical mirror system of the GCT telescope. A primary(4 m)-secondary(2 m) mirror optics system focuses the light onto a 0.35 m camera focal plane.

number of SST telescopes at the southern site is sub-optimal.

The alternative solution is the reduction of the camera plate scale through a dual-mirro design allowing the use of more affordable photosensors. The optical system of the telescope is complemented with a secondary mirror added to the primary mirror. This shortens the effective focal length so the focal surface will lie between primary and secondary mirror fig(5). This optical design is based on the Schwarzschild-Couder design first produced by Karl Schwarzschild (Schwarzschild, 1905) and later refined by Couder (Couder, 1926) and then adapted for use in IACTs by Vassiliev and Fegan [10]. With the dual-mirror design optimized for GCT by Blake et al. [11] the camera plate scale is reduced, allowing the use of more affordable photosensors, Silicon Photomultipliers (SiPMs) and multi-anode photomultipliertubes (MAPMs) among them, potentially reducing the cost of each SST.

## 2.2 Compact High Energy Camera

The Compact High Energy Camera, or CHEC (fig(6)) is one of three prototype camera concepts in development for one of the SST structures within CTA. One camera features 2048 photosensors, building equally many readout channels per camera. The readout is done by so called TARGET<sup>8</sup> modules for sampling, digitization and triggering, one of those consists of 4 ASICS<sup>9</sup> with 16 channels each. The camera houses 32 TARGET modules, one of them responsible for readout of 64 photosensors. The TARGET modules build the front-end of the integrated electronics<sup>10</sup> inside the CHEC camera connecting the buffer to the cameras backplane. After the

<sup>8</sup> TARGET TeV Array Readout with GS/s sampling and Event Trigger

<sup>9</sup> ASIC Application Specific Integrated Circuit

<sup>10</sup> FEE front end electronics

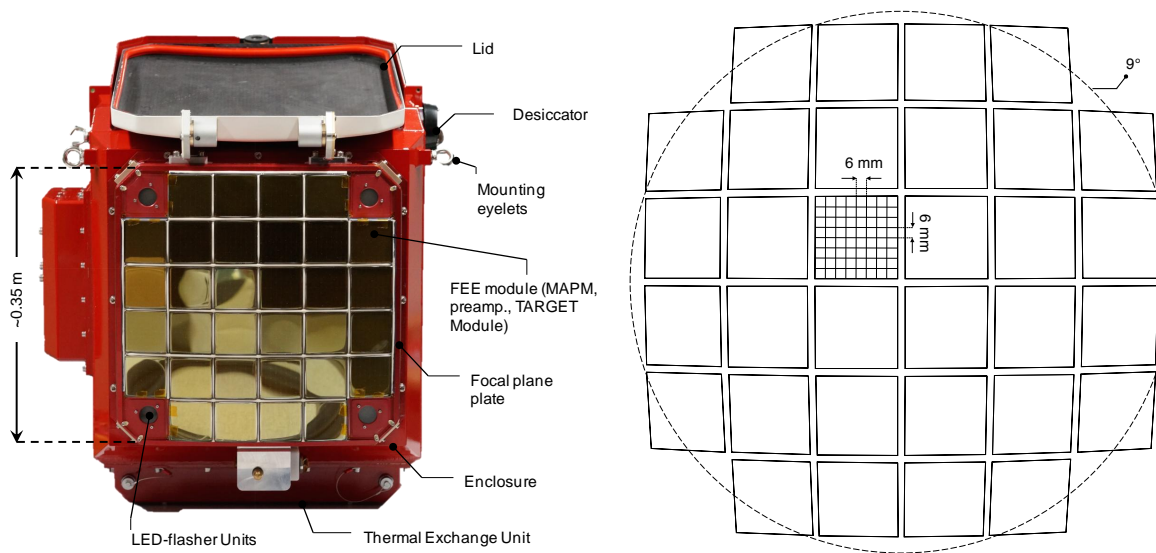


**Figure 6:** Front view of the CHEC-M prototype (left), view of the camera focal plane. Schematic of the focal plane (right), illustrating the 9° FoV with 6 mm pixels. Pictures from [18]

---

photosensor is triggered the buffer amplifies the signal, that is then send to the ASIC inside the TARGET module, where an analog-to-digital converter and a shaper convert the signal before it is send to the backplane for transfer to the main array hub. Two iterations of the CHEC camera are tested, CHEC-M is the first design based on MAPMs as photosensors and was the initial prototype platform all improvements to the electronics are tested on. CHEC-M since then moved to Meudon in Paris and is now mounted on the GCT structure for further testing of the entire GCT prototype. The second iteration of the camera: CHEC-S, based on SiPMs as photosensors is a similar concept, with applied improvements to electronics and mechanical design. The two cameras are very similar in shape and can both be mounted on the GCT structure without alterations.

In order to make an educated choice on the best SiPM candidate to use to populate the camera focal plane of the camera, an in-depth characteristic study on pulse-shape, gain, temperature-dependence, detection efficiency, thermal noise and correlated secondary effects is conducted by multiple groups within the CTA collaboration.

This work studies the gain, noise from thermal, as well as correlated secondary effects and their temperature dependence.

## 3 Silicon Photomultipliers

Silicon Photomultipliers (SiPMs) are semiconductor photo detectors, that have attracted increased attention over the last decade for their possible use in astroparticle physics. The sensor consists of an array of avalanche photo-diodes, typically  $\sim 50 \mu\text{m}$  in size. Depending on the pixel-size, one pixel contains several 1000 diodes, hereafter called cells. Each cell is a PN junction (fig(7)) supplied with a reverse bias-voltage above breakdown, which is called operation in Geiger-mode, in analogy to the Geiger counter. In this mode, a photon or thermal excitation will produce an electron-hole pair in the depleted region. Through impact ionization these charge carriers will in turn trigger an avalanche in a cell, which in turn generates a large output pulse typically in the range of several Mega electronvolt. This avalanche is then passively quenched by a resistor to limit the current in the substrate and to reset the cell to a quiet state so it is photosensitive again. The signal of the SiPM is the sum of the signal of all cells, read out over their quenching resistor via a common output.

### 3.1 SiPM characteristics

SiPMs posses major advantages over their progenitor, the Photomultipliertubes, or PMT. They are more resistant to mechanical and accidental light-exposure damage through ambient light. Single SiPM cells have a lower power consumption, but more SiPM cells are needed to cover the same space as a PMT. Operating at a much lower bias-voltage, there is no need for high-voltage as in PMTs. They possess a high PDE and are insensitive to magnetic field changes. There is rapid improvement, being a fairly new technology, with new generations every  $\sim 5$  months and decreasing costs per  $\text{mm}^2$ . Viewed over all cells of the whole pixel, fluctuations in the gain are

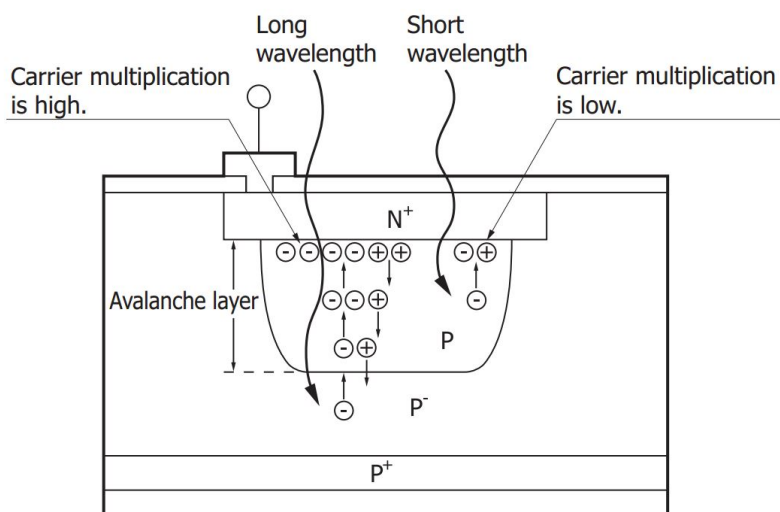


**Figure 7:** Structure and carrier multiplication through an avalanche inside a SiPM. Picture from [16]

very small. This is because of the uniformity during manufacture and visible in the width and the clear resolution of the p.e. peaks in the pulse area spectrum. See section(E) for examples. MAPMs on the other hand posses larger gain fluctuations, which is due to their structure. These make SiPMs an interesting candidate in astrophysics experiments for both, space- and ground-based telescopes (like IACTs). However SiPMs also posses drawbacks, one of which is their temperature dependence through their gain and Dark Count Rate (DCR). Another source of worry is their Optical Cross Talk (OCT), although manufacturers advance to reduce this source of noise.

Advantages:

- 1. Sturdiness
- 2. May be exposed to ambient light (observation during bright moonlight periods possible)
- 3. Low power consumption ( $\leq 50\mu\text{W}/\text{mm}^2$ )
- 4. Low operation voltage (typically  $\sim 20 - 100$  Volts)
- 5. No need for HV as in PMTs
- 6. High PDE
- 7. Insensitivity to magnetic fields
- 8. Being a fairly new technology it is steadily improved, meaning a new generation of SiPMs every 5months
- 9. Rapidly decreasing cost per  $\text{mm}^2$

Drawbacks:

- 1. temperature dependence of gain and DCR
- 2. Noise through OCT
- 3. cost per  $\text{mm}^2$  larger than PMTs

There is a multitude of attributes of SiPMs that are desired by CHEC, and CTA in general, among them is a high enough fill-factor (detector space versus dead space) to guarantee high Photon Detection Efficiency (PDE) (section(3.5)). The PDE quantifies the absolute efficiency of any photon detector to absorb a photon and produce a measurable signal at its output. To achieve a high PDE in the 400 nm regime, the design moves to very thin implantation layers on the surface in order to minimize the absorption of shorter wavelength photons in insensitive areas (fig(??)). Different entry window coatings and avalanche structures explore the capable enhancements in the blue sensitive UV region.

The peak of the spectral response of the SiPM is desired to be around the spectral peak of the Cherenkov light at  $\sim 400$  nm and at the same time, must have a fast enough drop to ensure less Night Sky Background (NSB) pick up (fig(8)). The overall noise from thermal and correlated secondary effects, like cross-talk, of the SiPM must be sufficiently below the expected NSB rate at the location (usually around  $\sim 20\text{-}80$  MHz[9]). It is common practice to compare those two characteristics directly to showcase the behavior of the PDE versus OCT. A point of low cross-

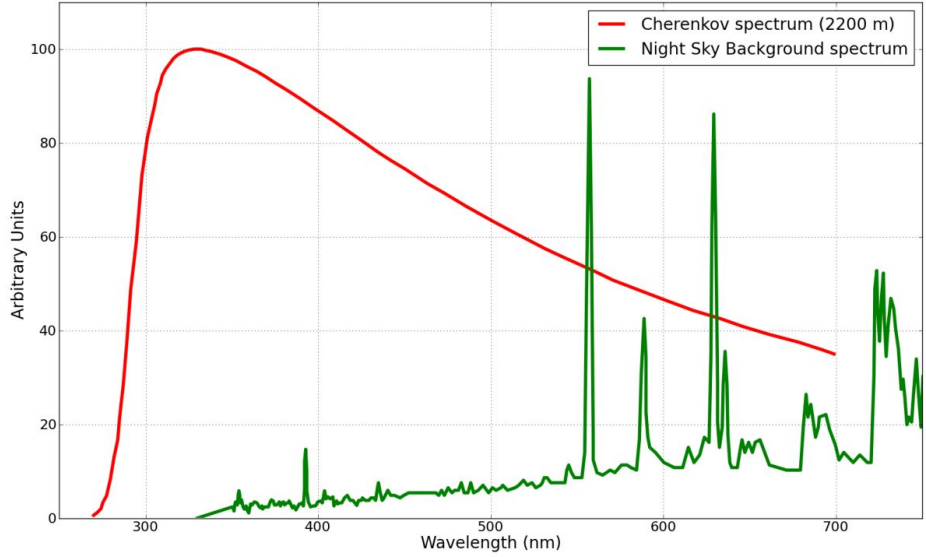


**Figure 8:** The spectrum of Cherenkov light observed from an extended air shower at 2200m asl. compared to the expected NSB measured in La Palma. Cut-off of the spectrum at wavelengths below  $\sim 300$  nm due to atmospheric absorption. The emission peaks above  $\sim 550$  nm in the NSB spectrum are mostly attributed to atomic oxygen, hydroxide and sodium in the atmosphere. Units on the y-axis are arbitrary because NSB and Cherenkov light vary by different parameters. There is a region between 550 and 650 nm, where the average Cherenkov light spectrum across the focal plane and contributions from the NSB overlap. Image from [9]

talk, where the PDE is still at maximum is desired.

Another important characteristic is the temperature dependence of the gain. While the CHEC camera is observing, the preferred fluctuation of the gain is  $\leq 10\%$ . The camera focal plane underlies temperature shifts during operation, which will be slightly countered by cooling the photosensing area. Despite that the focal plane will still be warming up, so a lower gain dependence on temperature is desired in order to minimize the gain fluctuations.

### 3.2 Gain of a Silicon Photomultiplier

The gain of a SiPM measures the internal conversion of a photon incident into a signal at the output. The amplification of the device is expressed as the average number of charge carriers produced. There is no distinction whether the incident was caused by a single original photon or a thermal electron. The gain ( $M$ ) (eq 1) of a SiPM results from the deposited charge ( $Q$ ) of the pulse generated from one cell when it detects one photon, divided by the charge per electron ( $e$ ). The charge deposited per event is proportional to the cells capacitance ( $C$ ) and

the supplied over-voltage ( $V_{bias} - V_{breakdown}$ ).[9] This results in the gain (M) in units of total number of charge carriers, usually in the several  $10^6$  range.

$$M = \frac{Q}{e} \quad (1)$$

$$Q = C \times (V_{bias} - V_{breakdown})$$

Estimation can be done via the voltage mean of the 1 p.e. amplitude: (e.g. see figure(25)). For a better understanding, stating the gain in units of mV per photoelectron or mV/p.e. is more suitable, as it gives a direct correlation between detected photoelectron and expected voltage amplitude. Given the very narrow pulse shapes, using the average pulse amplitude and extracting FWHM as a time measure of the total charge flowing during discharge and using the formula (eq 2):

$$Q(p.e.) = C \times (V_{bias} - V_{breakdown}) \quad (2)$$

$$U(p.e.) = \frac{Q(p.e.)}{t(FWHM)} \times 50\text{ohm}$$

Resulting in the expected event charge flowing during capacitor discharge. Given the bias-voltage and C as capacitance of one cell and the resistance (50ohm) of the quenching resistor, a conversion factor and the average amplitude per photoelectron can be extracted.

The gain is obviously higher the larger the cell capacitance or the higher the bias-voltage (eq 1) will be. But increasing the bias-voltage also increases dark counts and crosstalk. The gain is also dependent on the temperature, mainly through the quenching resistor but also from the silicon bulk itself, at a certain bias-voltage decreasing as temperature rises. The quenching resistor is affected by a lowering of the electrical conductivity with rising temperature, in accordance to the Wiedemann-Franz law, stating that the ratio of electrical and thermal conductivity remains constant. The silicon bulk at rising temperatures underlies increased crystal lattice movement. This impinges charge transport by increasing the probability that carriers might impact on the lattice before the carrier energy has become large enough for continued ionization. In order to counteract this, the electric field must be increased by increasing the supplied bias-voltage so ionization is more likely. Doing this has drawbacks as discussed before. For application as a photon detector, keeping the gain constant is an inevitable step, otherwise the shifting gain leads to problems. To do that, either the bias-voltage need to be adjusted to match ambient temperature, leading to problems with varying dark counts and crosstalk. Or the surface temperature must be regulated to be kept constant. Although more challenging hardware would be required, the latter option has obvious advantages, keeping dark counts and crosstalk and more important the gain constant by simply regulating the surface temperature.

Taking into account equation 1, it appears that the breakdown-voltage can be estimated from the zero-crossing of a linear extrapolation of the gain at every bias-voltage per temperature. By doing this a linear breakdown-voltage dependence of the temperature can be observed. See section(F)

When parametrized over over-voltage, the gain is essentially temperature independent.

For gain measurements see section(6).

---

### 3.3 Thermally induced dark counts

---

Inside the SiPMs depleted region a dark pulse originates from thermal excitation of an electron to the conduction band. Without an event photon present to trigger the avalanche, it is still indistinguishable from a photoelectron pulse. These thermally generated carriers are observed along with the signal from a real photoelectron, presenting an irreducible source of noise. The number of dark pulses observed is referred to as dark counts ant the number per second as the Dark Count Rate (DCR). For applications that need to operate in an environment with low noise, those dark counts are a concern. In IACT application of SiPMs however, this is only a minor problem, since IACTs operate in a naturally noisy environment. Even though sky darkness is one of the prime criteria of the proposed site selections for CTA, the surrounding NSB at the most darkest side in Chile will still exceed any random noise in the detector. The pollution of those NSB photons is unavoidable noise and will essentially limit the low energy resolution of the telescope to the NSB rate. As long as any random noise, being dark counts or other, is significantly below the NSB rate, it will not affect the telescopes performance.

Telescope performance simulations of the Schwarzschild-Couder MST of CTA at the site of Chile showed a rate of  $\sim 20 - 80$  MHz per pixel for one of the older SiPM iterations from Hamamatsu.[9] This is purely for NSB photons and pixels with a size of  $6 \times 6$  mm $^2$ , the covered range originates from differences in illumination level of the night sky by galactic- and extragalactic-fields.

---

### 3.4 Avalanche-induced secondary effects

---

An avalanche originating from the primary cell can sometimes, either directly or by reflection, propagate outside the cell and trigger an avalanche almost simultaneously in a secondary cell. This will, unless accounted for, degrade the SiPMs photon counting resolution, since the signal will be a merge of cross-talk cells and real incident cells. This effect is referred to as the OCT, since it is conveyed via secondary photons generated in the primary avalanche. Afterpulsing also falls under this category, with the main difference to cross-talk being that the carrier triggers a secondary avalanche in the primary cell, basically generating a parasitic pulse inside the previously fired cell. Contained in a single cell, afterpulsing increases the measured charge registered for an incident photon. The difference in arrival time of the secondary avalanche distinguishes different components comprising the cross-talk and afterpulsing. Those secondary

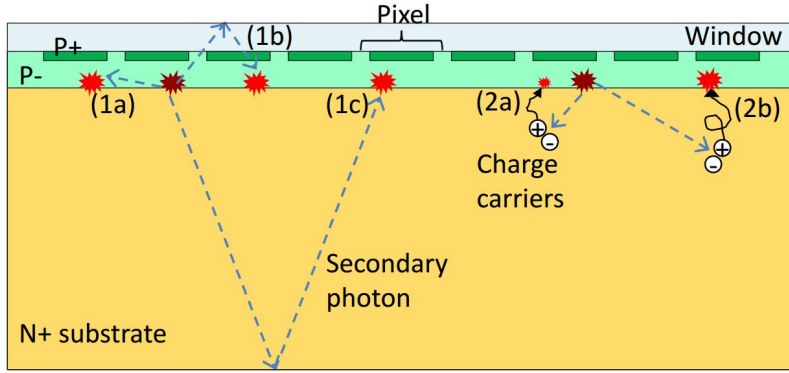


**Figure 9:** Secondary effects (bright red) caused by primary avalanches (dark red) in a Silicon Photomultiplier. In this work a single pixel, in this figure, is referred to as a cell (see section(3)). Everything labeled under 1 is associated with prompt cross-talk, afterpulsing labeled as 2a, and delayed cross-talk labeled as 2b. Image adapted from [13]

avalanches can again emit photons, that can trigger secondary avalanches themselves, leading to high amplitudes, even in dark conditions. Cross-talk is dependent on the ability of the secondary photons to reach a neighboring cell. This means, that an increase in cell-size and therefore cell-area should directly correlate with the OCT of a pixel. The OCT dependency on the cellsize was tested and can be found in section(C).

Figure(9) shows different physical processes causing secondary effects in SiPMs based on their delay time. Cause of the delay time is the dependence on the penetration depth of the incident photon, or the region the dark count generated, and the diffusion time inside the substrate. At long delay times of up to 70ns afterpulsing and cross-talk are not distinguishable.[13] The prompt OCT happens basically simultaneous to the primary avalanche, since it is unaffected by the primary cells recovery time and is labeled 1 in Figure(9). It is either triggered by the secondary photon directly (1a) reaching the neighboring cell, or after first reflecting on the surface layer (1b) or the bottom surface (1c). If the cross-talk avalanche delay time is shorter than the detection resolution, the difference in signal between an OCT event or an incident photon being detected, is not observable.

Time delayed OCT is caused by a carrier generated in the non-depleted substrate diffusing to a neighboring cell and triggering an avalanche in the depleted region (2b). If the carrier stays in the primary cell, the triggered avalanche is labeled afterpulsing (2a) and will have a lower amplitude, due to the cell not being recovered yet. The delay time is influenced by how deep the carriers are being trapped in the substrate, the time they need to diffuse to the surface, and also distinguished by traps with different lifetimes.

This is very important in IACT performance, since this effect gives random NSB and dark count photons the ability to rise to larger amplitudes. The consequent need to raise the trigger threshold to counteract the resulting rising accidental-triggerate has a negative impact on the low

---

energy resolution of the telescope.

Parametrized with over-voltage, the secondary avalanche effects are temperature independent, for OCT measurements see section(6).

---

### 3.5 Photon Detection Efficiency

---

$$PDE = \frac{N_{detected\ photons}}{N_{total\ photons}} \quad (3)$$

The PDE is the probability of a detector to absorb an incoming photon and produce a measurable signal at its output, and depends on a number of factors. First the photon must enter the depleted region via transmission through the surface of bare silicon, which has a reflectivity of 30%. However, the transmission probability can be improved by coating the surface with a substrate with adequate thickness and a refraction index between air  $\eta_{air} = 1$ . and silicon  $\eta_{silicon} = 3.4$ . Devices presented in this work are coated with a silicon resin and glass. The coating also has the added benefit of insulating and protecting the cells against environmental influence. A possible negative effect of coating is an increase in prompt cross-talk and a larger dependency of the overall cross-talk on the cellsize.[20] The second factor is quantum efficiency, describing how susceptible the depleted region is to photons exciting electrons from the valence band to the conduction band. This is also referred to as spectral response of a detector to reflect the wavelength dependence of a detector and makes the PDE wavelength dependent. The over-voltage dependency of the PDE is conveyed by the third factor, the avalanche probability. It depends on the electric field present, and thus on the applied over-voltage. The last factor is the fill-factor: the more the surface area of the detector is covered with active-area cells and the less dead-area exists between cells the higher the fill-factor is.

The PDE is commonly measured by illumination of the pixel and a calibrated reference photodiode with a flashing light source, and determining the average number of photons hitting the photosensor during a light pulse.

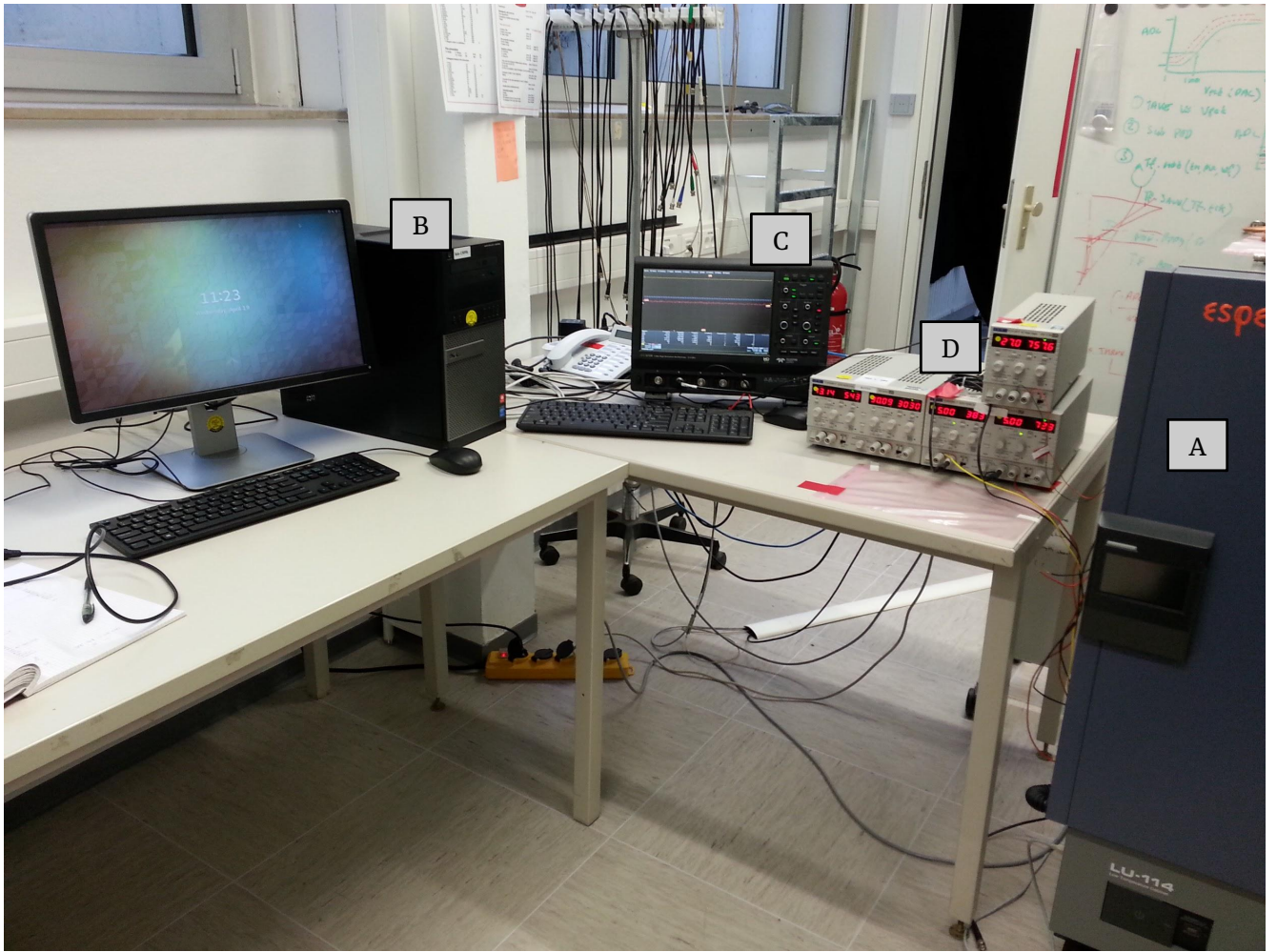


**Figure 10:** Outside view of the teststand with the ESPEC LU-114 thermal chamber (A), the Lab-PC (B), the Lecroy HD6104 oscilloscope (C) and the TTi power supplies (D).

## 4 Experimental Setup

The experimental setup in general is designed to house a variety of SiPM devices. Over the course of this work, 5 different types of SiPMs were mounted on the setup and evaluated. It involves a thermal chamber fig(12)(A) for temperature regulation which proved light tight and thus also serves as a dark box, to prevent any stray light to reach the SiPMs surface. The thermal chamber in question is a LU-114 constant climate cabinet from ESPEC with a programmable interface for remote control. The chamber is able to raise and lower the inside temperature with a  $\pm 0.5^\circ\text{C}$  accuracy, direct measurements of the SiPMs surface with a temperature probe confirmed this. In the absence of light tests, heating of the SiPM surface through the dark current proved no concern.

Depending if the SiPM fig(12)(A1) in testing is pre-manufactured on a test-array or supplied as a standalone chip, it is either mounted directly on a mechanical arm inside the chamber in the former case, or in the latter the mechanical arm supports a specifically designed PCB

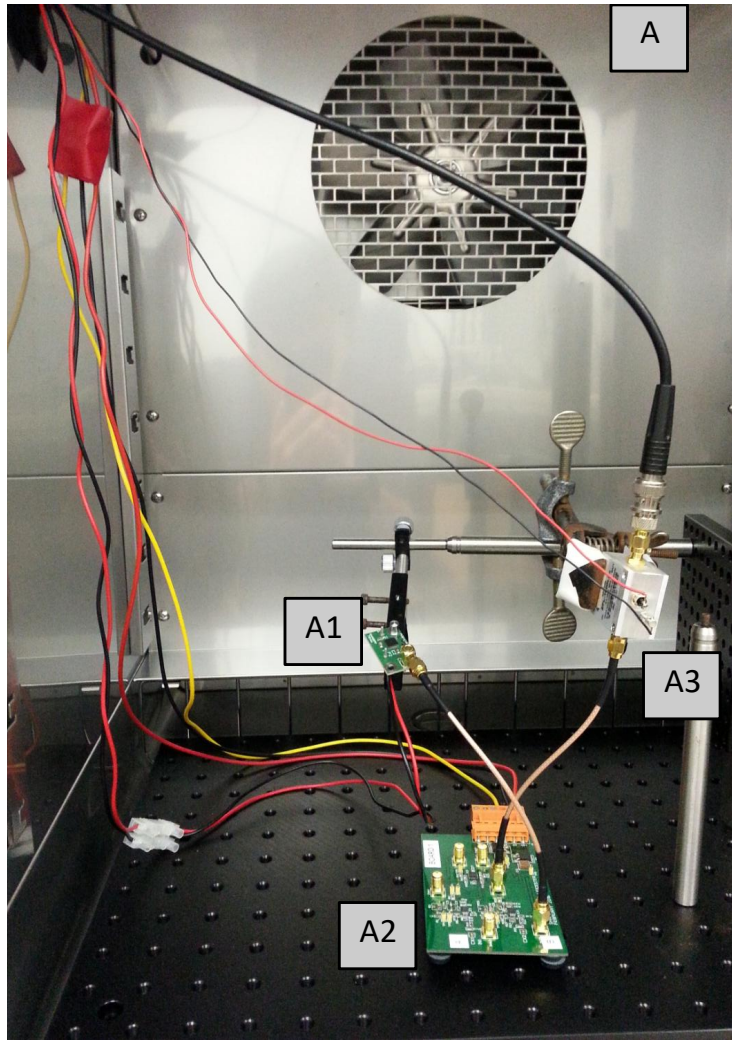


**Figure 11:** Inside view of the thermal chamber (A), with the SiPM (A1), the shaping electronics (A2) and the MiniCircuits PreAMP (A3). Signal throughput in the top left corner.

connecting to the device. Via the mount, bias-voltage is supplied and signal is transferred to the shaper fig(12)(A2). In some cases the output signals amplitude is to low to trigger the oscilloscope, therefore amplification is needed. I used a ZFL-1000-LN+ amplifier from MiniCircuits fig(12)(A3) supplied with different voltages depending on the tested device to amplify the shaped signal.

Data acquisition in the Laboratory is realized by a Lab-PC fig(12)(B), that forms the central control station for multiple pieces of equipment. It is connected to the oscilloscope fig(12)(C), which records the waveforms of the device in testing, and then sends the data back to the PC via Ethernet. The oscilloscope is a Lecroy HDO6104 1GHz HD Oscilloscope capable of 2.5 GS/s.

The TTI power supplies fig(12)(D) control the bias-voltage of the SiPMs, ramping of the bias-voltage is controlled by the PC. Lastly the thermal chamber is connected to the Lab-PC, where

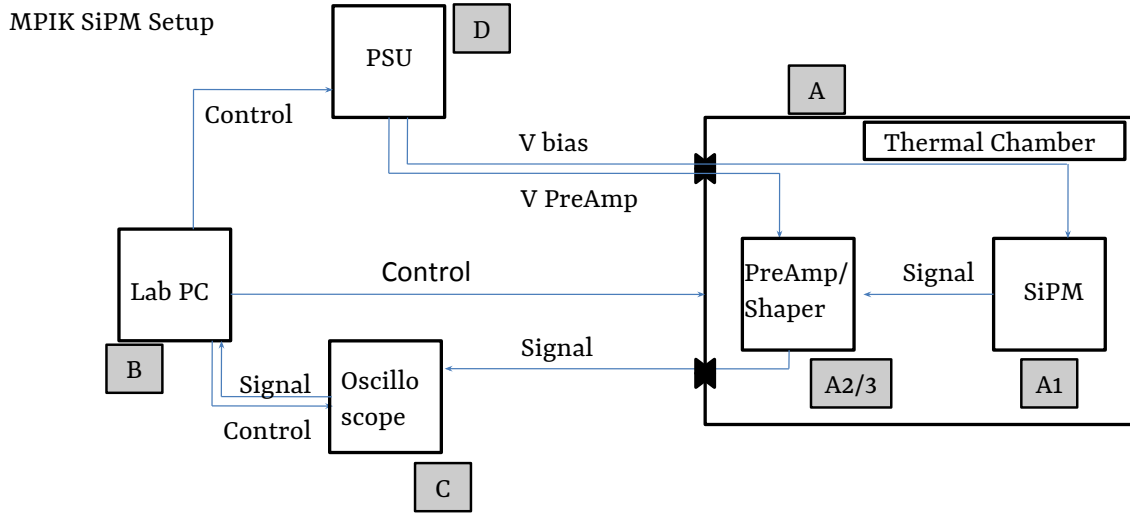


**Figure 12:** Experimental setup scheme, Annotations see text

the data acquisition script controls the temperature, and continuously rechecks it during temperature ramps. Signal transfer from the shaper to the oscilloscope is via a throughput on the side. All equipment is connected via ethernet, plugged into a common hub, to form a local network. While the temperature of the thermal chamber is ramping from the previous to the next set-point, the data is send to the Lab-PC.

Temperature regulation is an issue in the teststand, as there is no way of controlling the SiPMs surface temperature. In dark conditions however, without conducting illumination tests, the shift in temperature on the SiPMs surface is only minimal. See section(F) for the breakdown-voltage dependence on temperature. Checking the surface temperature of all devices with a temperature probe during testing showed minimal rising temperatures. So the influence of the temperature on the breakdown-voltage is only of minor concern. However, once illumination tests begin, the rising temperature on the SiPMs surface will no longer be negligible and the temperature must be regulated, either by cooling of the surface or including the temperature parameter.

There is also the issue of the saturation of the input of the oscilloscope making the higher over-voltage range difficult to reach, due to potential multi p.e. pulses being amplified and reaching the input. This is possible because of the difference in amplitude between a 1 p.e. and a multi p.e. event and the electronic noise, forcing a high resolution of the amplitude in the oscilloscope. Different couplings were tried to circumvent the problem, which showed no improvement.



**Figure 13:** The shaped and unshaped pulse from a pulse generator emulating the output of the front-end buffer of the CHEC-S SiPM. The unshaped pulse in yellow and negative, due to the buffer-output. The shaped pulse is flipped to the negative through the electronics in green. Image credit [21]

The shaper consists of two stages, the main components are an Op-Amp amplifier serving as an input buffer followed by a zero pole cancellation circuit for pulse shaping and is commonly used in photon-counting applications. A zero pole cancellation circuit is basically a RC circuit eq(4) ( $C_Z, R_0$ ) suppressing the high frequencies to narrow the pulses from the usual  $\sim 50$  ns to  $\sim 10$  ns, using a high-pass filter with a tunable time constant, through  $f_C$  which gives control over the frequency response of the circuit.[22]

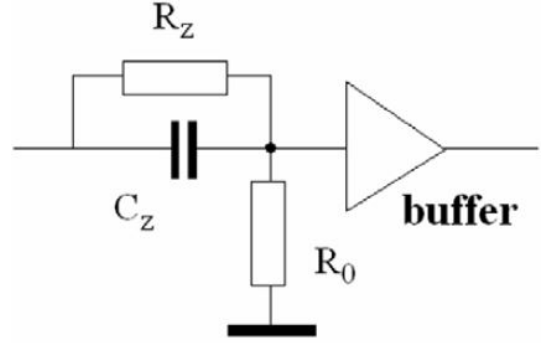


**Figure 14:** A Zero Pole cancellation circuit commonly used in photon counting applications. Taken from [22]

$$R_0 \times C_Z = 1/(2\pi \times f_C) \quad (4)$$

In Figure(13), the shaped and unshaped pulse is shown, the negative amplitude (yellow) corresponds to the unshaped signal mimicked by a function generator to emulate the output of the front-end buffer of the CHEC-S SiPM. These tests correspond to an initial design of the shaper and do not correspond to the final setup.

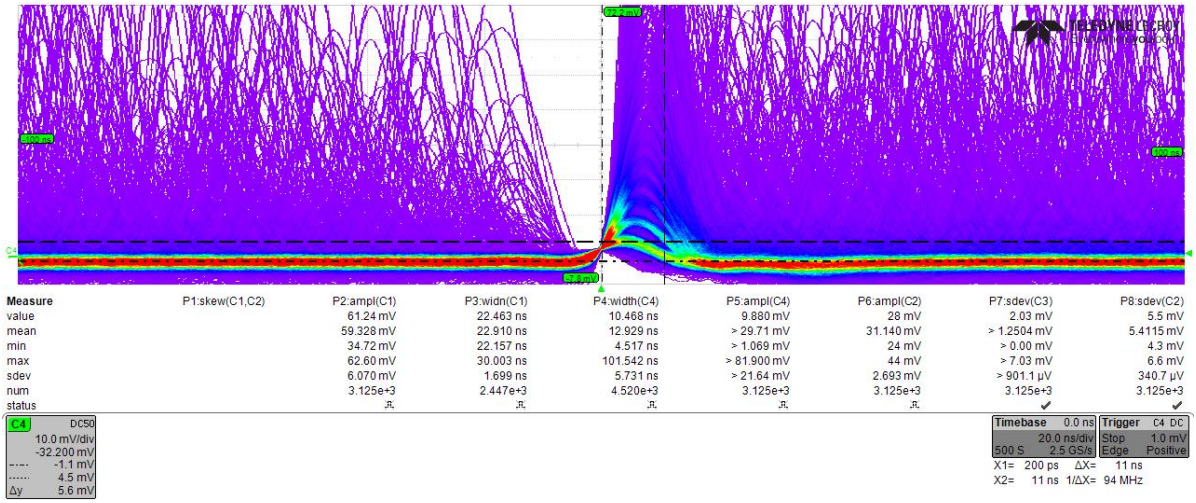


**Figure 15:** Persistence figure of the shaped pulse after adapting the electronics to a preferable pulse shape. In the center, a row of pulses with rising quantified amplitudes is visible. These are the multiple N p.e. pulses, differing by  $\sim 5$ mV. The purple area off-center is due to delayed cross-talk and after-pulsing. Image credit [21]

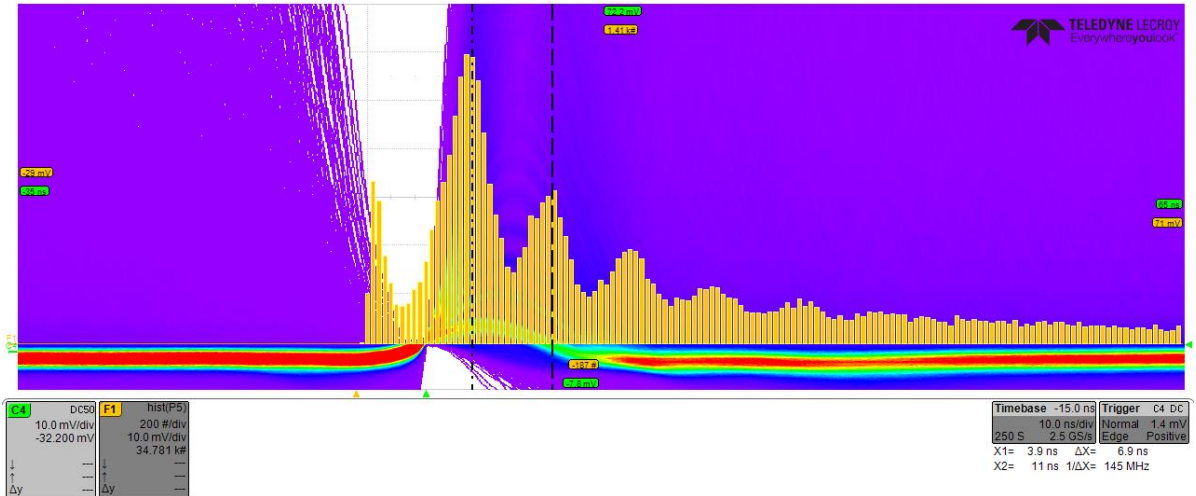


**Figure 16:** An oscilloscope based pulse height spectrum in the same scheme as the persistence plot fig(15). The distance between the peak maxima delivers an estimation of the gain of the SiPM at this bias-voltage. Image credit [21]

The shaper board contains tunable capacitors (C9) and resistors (R20) (see schematic in section(G)), that can be tuned and optimized for ideal pulse layout. The green pulse in figure(13) shows the output after shaping, with a width of FWHM of 9 ns. The output pulse has some ringing after the main pulse.

After tweaking the tunable electronics on the shaper to a preferable pulse shape, clear quantified single p.e. peaks are visible in a persistence plot. fig(15). The peaks have an amplitude of  $\sim 5$  mV/p.e., from this and from the following, a gain estimate for the peak finding threshold in

---

the analysis can be made. With the same configuration a gain estimate at different bias-voltages of the SiPM is possible through an on-oscilloscope pulse height spectrum fig(16). The distance in peak maxima is a reference to the gain of the SiPM, in the case of figure(16) close to  $\sim 5$  mV/p.e..

This chain of shaper modification is done for every single SiPM cell from Hamamatsu Photonics K.K. tested in this work (three in total) as they arrived as a single unmounted device, in need of shaping and amplification. The device from SensL is premounted on a test array, preshaped and only externally amplified.

---

## 5 Data Analysis

---

The analysis of the SiPM waveforms is done exclusively in python following the sequence:

1. data conversion
2. pedestal subtraction
3. peak detection
4. gain extraction
5. calculation

The waveform data, after being transferred to a separate PC, is analyzed offline. The goal is to extract event-data from the waveforms in order to produce pulse-area spectra for every bias-voltage at every temperature. To that end, the pedestal of the electronic noise must be found and subtracted from the data. After that, event-pulses are detected and integrated. This generates a list of pulse-areas, which is in turn used to fill a pulse-area histogram. To this pulse-area histogram, a model is fitted from which the gain can be extracted. Due to the linear behavior of the gain with rising bias-voltage, a regression line is fitted, from which the DCR and the OCT are calculated using the original pulse-area histogram.

---

### 5.1 Tracefile Conversion

---

The oscilloscope produces the waveform data in its intrinsic data format, called a trace with the data suffix trc in binary. A trace file contains a header and two binary lists, an amplitude based on the oscilloscopes voltage-range and offset, and a list of the same length containing the associated event-time, based on the time-range and horizontal offset. The first step is therefore a conversion of the amplitude and associated event-time of all segments of a waveform trace file into two lists of floats.

## 5.2 Pedestal Subtraction

A single waveform from the oscilloscope is anticipated to be uncentered fig(17)(grey), it will be slightly above or below zero, depending on the device setup (some devices produce inverted signals). The signal is mixed with electronic noise when it is observed and forms a pedestal, shifting the mean of the waveform from its original position to zero. Pedestal subtraction removes this average noise.

The first step of the process is reading in the uncentered waveform fig(17)(grey) and calculating an initial mean(mean0), expected to be slightly higher than the actual mean of the noise, due to the presence of event-pulses. The waveform is then shifted to about zero,

by subtracting the mean0. A second mean of the now nearly centered waveform is taken (mean1). Now a new, same-sized array is formed and filled with the data from the waveform that is smaller than mean1, this represents the negative part of the noise. The data larger than mean1, the positive noise, is also filled into the array, but is negative-signed. This creates an array of the waveform centered around zero and, above the mean1, folded towards the negative. It proved reliably, that calculating the root-mean-square of this helper-array is a solid possibility of stripping the waveform of event-peaks. Taking the root-mean-square with a factor 3 of the helper-array, a cut is now applied to the waveform on both, the positive and negative side. In that fashion, the remnant is the waveform between the positive and the negative root-mean-square and is now called a peakless-signal, representing the noise of the waveform.

Pedestal subtraction is done by calculating the mean of this peakless signal and subtracting it from the waveform. After that, the peakless signal is also smoothed by convolving it with a wide-windowed gaussian and subtracted from the waveform to eliminate any slow moving noise, the resulting waveform is called "Filtered Signal 1" fig(17)(blue).

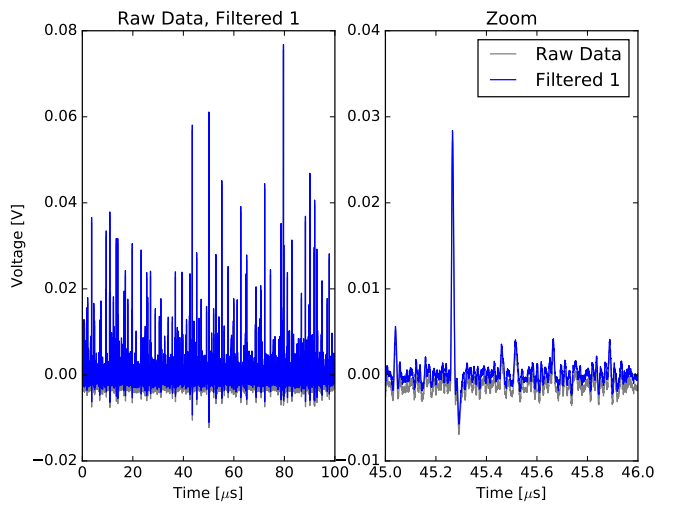


**Figure 17:** Raw, real data from a HPK SiPM in grey, in blue the pedestal subtracted and smoothed "Filtered Signal 1"

### 5.3 Peak Detection

Peak detection exploits the fact, that the first derivative of an event-peak will cross zero into the negative at the time of the peak maximum. The presence of random noise in the signal however will lead to many false detections. Therefore, before the detection of the event-peaks, the waveform fig(18)(grey) is smoothed with a narrow-window gaussian with a width of about the FWHM of the devices characteristic event-pulse, in order to attenuate non-event peaks fig(18)(blue). After the first derivative of the signal is calculated, which in python is a fast process if using arrays, a number of parameters decide the validity of the detected peaks. Most important parameters are a certain predetermined minimum amplitude, called the amplitude threshold or: minimum peak height. This is determined from initial examination of pulses on the oscilloscope and entered as a parameter to the analysis chain, but could later be calculated based on the noise level. The second important parameter defining validity is the minimum peak distance, which defines how close two events can occur after another. The value is determined by the FWHM of the device in testing, which is expected to be sensible enough to resolve two events happening close after another.

While peak detection is done with help of "Filtered Signal 2", the integration of the pulses uses "Filtered Signal 1", as to not falsify the data, because "Filtered Signal 2" is subject to attenuation during the smoothing. The difference in amplitude can be seen in figure(18).

The peak detection algorithm cannot distinguish between instantaneous and delayed Optical Cross Talk, but nonetheless, due to the fact, that the signal data is taken over many micro-seconds, all events are detected, independent of their source. On the other hand, this also means, that it is possible for two events to happen at the same time, for example a real photoelectron-event coinciding with delayed OCT or two simultaneous dark events being misinterpreted as one dark event + prompt cross-talk. This cannot be distinguished and will lead to a slight shift of the amplitude, due to the mostly lower amplitude of afterpulsing and cross-talk events.

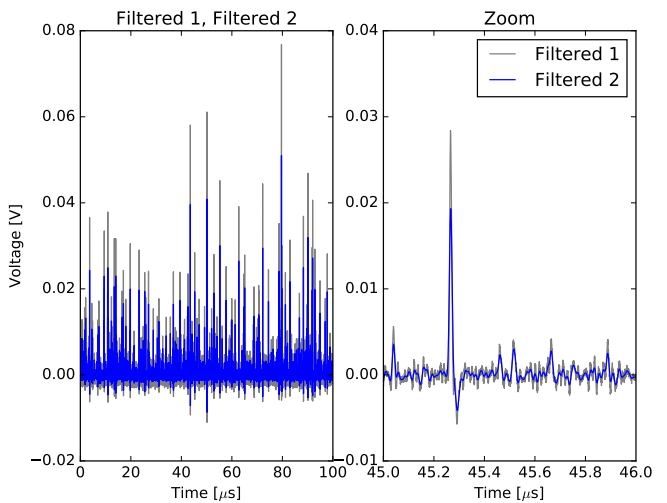


**Figure 18:** "Filtered Signal 1" in grey before smoothing with a narrow gaussian to generate "Filtered Signal 2" in blue, which is used for peak finding.

## 5.4 Gain Extraction

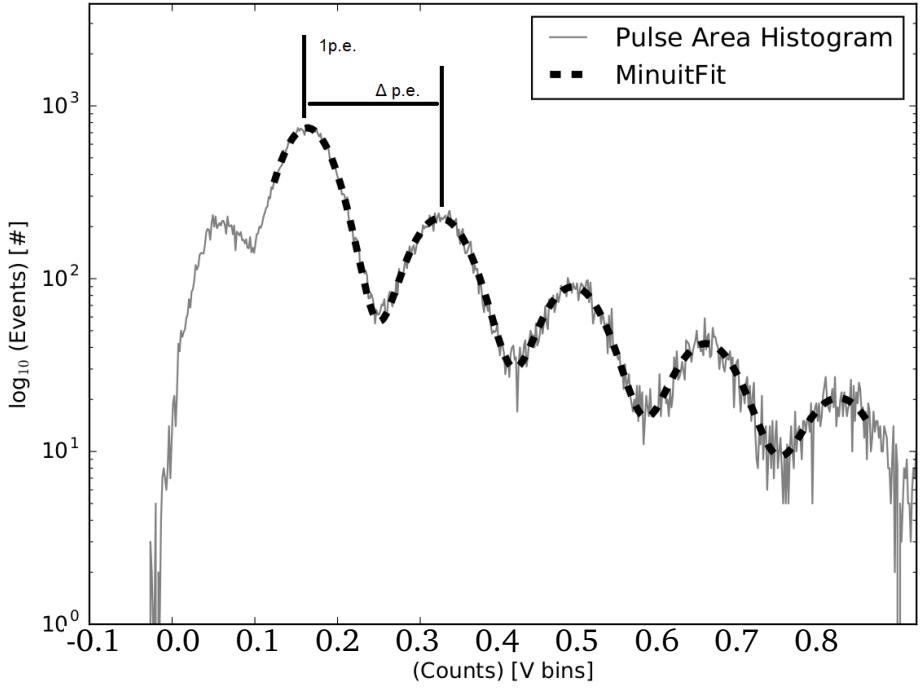


**Figure 19:** Pulse Area Histogram of a HPK S12642 with 1p.e. and  $\Delta$ p.e. positions. Multi gaussian fitted function eq(5) as black dashed line.

The detected peaks are integrated with “Filtered Signal 1” and with a window extending symmetrically from the peak maximum, the width is chosen as slightly wider than the peaks FWHM. The generated list of peak areas is generating a peak area histogram (see section(E)). The amplitude, position and sigma of the first p.e. peak is calculated and fitted with a single gaussian using pythons scipy curvefit, the fitted parameters serve as a first guess. After the first guess parameters are determined, the histogram is fitted with a function of multiple gaussians eq(5) using iMinuit in python, seen in figure(19). To determine the number of gaussians to fit, another function checks the viability of each N p.e. peak, among the checked parameters is the ratio in height to the 1 p.e. peak and the amplitude of the checked Nth p.e. peak in the histogramm. The fit function  $F(x)$  is a function of multiple gaussians with equal spacing eq(5).  $N$  is the multiplicity of the function or range the fit function is to be applied.  $A$  is the Amplitude of the Nth p.e. peak with  $\sigma$ ,  $\chi_0$  is the x-position of the 1 p.e. peak,  $\Delta x$  is the p.e. spacing distance.

$$F(x) = (N \times \left[ A \times e^{\frac{-(x-(\chi_0+N \times \Delta x))^2}{2 \times \sigma^2}} \right]) \quad (5)$$

Two parameters are extracted from the fit to the peak area histogram. The first  $\chi_0$ , the position of the 1p.e. peak is the position of the maximum of the first peak in the histogram, and the

position of corresponding multiple p.e. events should be integral factors of the 1p.e. position. This proved to not be the case for some devices, the suspected source of this error is a pedestal generated during the peak integration. For a more detailed study of the effect of the integration window see section(5.6).

A second parameter is extracted from the peak area histogram to deal with this problem, which is the distance between N p.e. peak maxima of the histogram, labeled  $\Delta$ p.e. This distance defines the gain, as it gives a measure of the difference of the generated signal of a 1p.e. signal and a 2p.e. signal. The apparent pedestal of the pulse area histogram makes extraction of the two parameters necessary in order to calculate the DCR and the OCT.

The gain of a SiPM has a linear dependence of the supplied bias-voltage. Given that the bias-voltage range is deliberately chosen such that the over-voltage ranges from about 1V growing upwards, the range of linearity only starts at around the point of operation given by the manufacturer of the device. At the higher end of the bias-voltage range the behaviour usually starts to divert from the linearity. In order to get an estimation of the gain over a large range, both previously extracted parameters, the 1p.e. peak and the distance  $\Delta$ p.e. are fitted with a linear regression line. The fit assumes linearity utilizing weighted least squares inherited from pythons statsmodels package. For the fit, the data, where more than two gaussians are fitted to the peak area histogram has a stronger weight.

Plotting both extracted parameters, as well as their respective regression lines versus bias-voltage, as in fig(20), shows the difference between the two parameters. Comparing the manufacturer supplied breakdown-voltage from the datasheet for all devices showed, that the zero-crossing of the 1 p.e. regression line is more consistent with datasheet values, in contrast to the zero-crossing of  $\Delta$ p.e. , which lies slightly higher. The over-voltage, corresponding to the set bias-voltage at any given temperature is calculated from this breakdown-voltage.

DCR and OCT are calculated utilizing 1p.e. position and  $\Delta$ p.e. derived from the regression line. Both values are applied, in the calculation, to the peak area histogram with the DCR of a

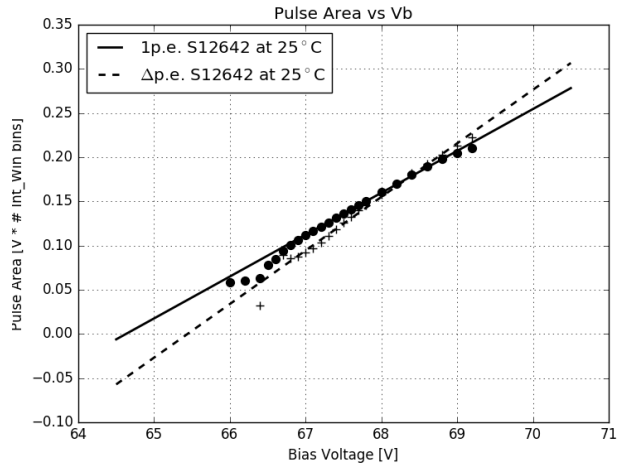


**Figure 20:** 1p.e. position and  $\Delta$ p.e. extracted from the Pulse Area histogram at every bias-voltage for HPK S12642 with their respective regression lines.

SiPM being defined as all events exceeding 0.5 p.e. in amplitude  $N_{events(\geq 0.5p.e.)}$  occurring over the experiment time  $t_{experiment}$  eq(6). Included in the measurement are thermally generated dark counts, as well as delayed cross-talk and afterpulsing with only a minor contribution.

$$DCR = \frac{N_{events(\geq 0.5p.e.)}}{t_{experiment}} \quad (6)$$

The OCT of a SiPM is defined as all events exceeding 1.5 p.e. in amplitude  $N_{events(\geq 1.5p.e.)}$  devided by all events exceeding 0.5 p.e. in amplitude  $N_{events(\geq 0.5p.e.)}$  eq 7. It scales with the number of photons produced inside an avalanche, as well as the probability of these photons to trigger a neighboring cell

$$OCT = \frac{N_{events(\geq 1.5p.e.)}}{N_{events(\geq 0.5p.e.)}}. \quad (7)$$

---

## 5.5 Analysis improvements

---

For one, at higher DCR the multi hit coincidence of two 1p.e. pulses rises and together with the resolution of the waveforms this could lead to the OCT being calculated high (see section(K)). Changing the determination of the threshold from being measured with an oscilloscope and added as a parameter by hand, to being determined on a per-waveform basis before peak-finding could improve the lower over-voltage resolution depending on electronic noise.

The source of the 'pedestal' in the pulse area spectra is suspected to originate from the pulse integration, but this is not certain.

## 5.6 Data Challenges

### 5.6.1 The influence of the minimum peak distance

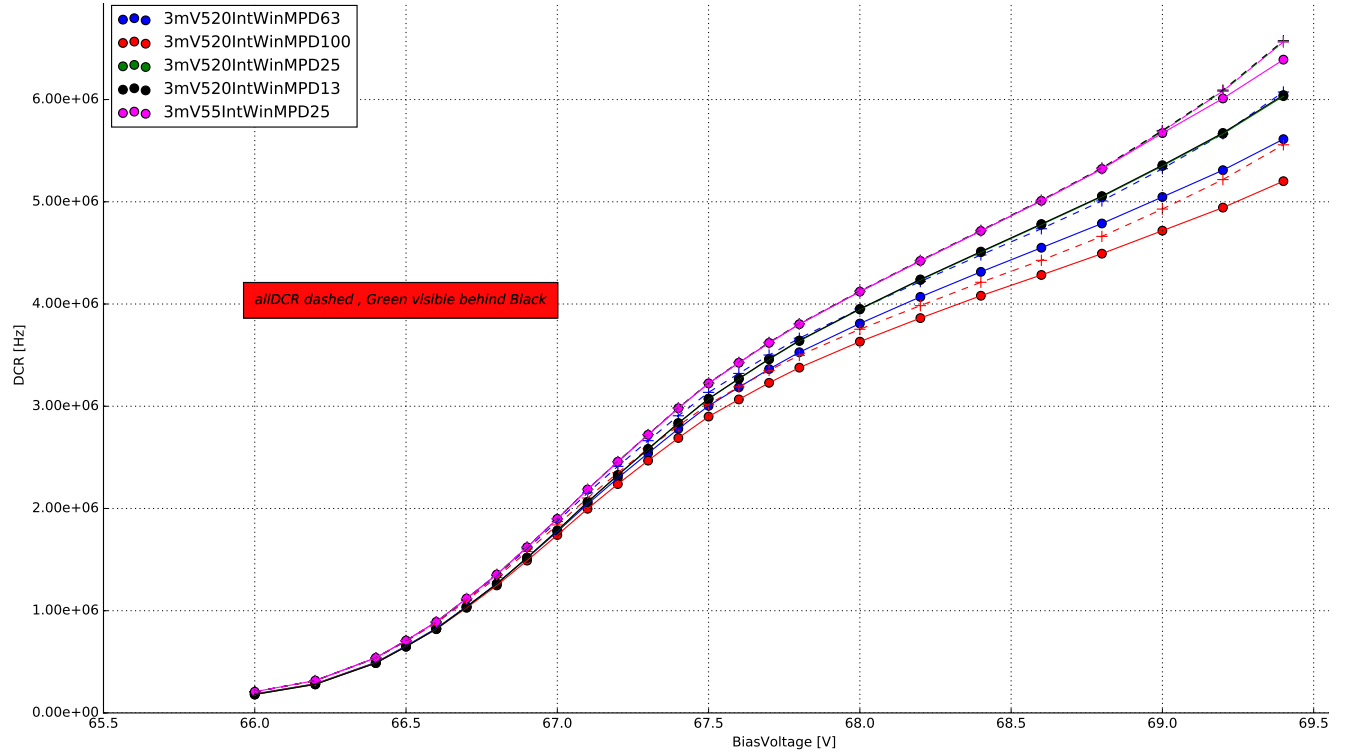


**Figure 21:** The difference between 4 minimum peak distance windows, in time-bins, during the peak detection. The dashed lines are the DCR considering all recorded events, forming an upper limit. In pink, the effect of a different integration window is shown.

The influence of the minimum peak distance is shown in fig(21) . Based on their bin-width, four different peak-distance-windows are tested. With the oscilloscopes sampling rate of 2.5 GS/s, the windows of 100, 63, 25 and 13 time-bins, correspond to 40, 25, 10, 5 ns windows respectively. With a event pulse FWHM of  $\sim 10$  ns, setting the minimum peak distance to 100 bins, resulting in a 40ns window is visibly to large, as the algorithm will skip over valid data fig(21)(red). After an event is detected, skipping over 40ns worth of data will result in errors of the DCR, since the calculation uses the complete experiment time. Therefore a more reliable distance window must be chosen. The second window of 25 ns was the next approach, originating from the length of the pulse-tail fig(21)(blue). This would lead to no detected events overlapping with the tail of one previously detected, resulting in a sharper pulse-area spectrum. Compared to a window of approximately the pulse FWHM, the previously discussed window would still lead to lost event-data. Since the sharpness of the pulse-area spectrum is already sufficient, a window around the pulse FWHM was chosen as reference for all measured devices

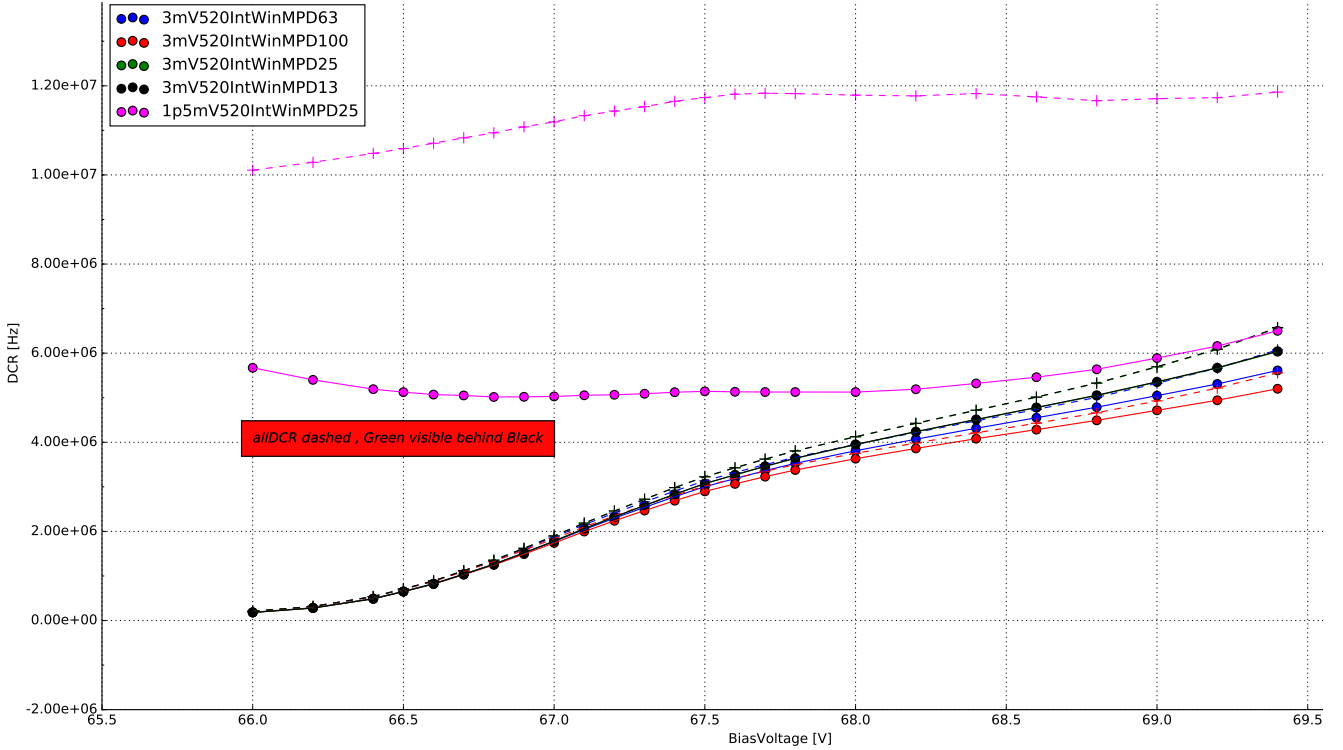


**Figure 22:** The difference between 4 minimum peak distance windows, in time-bins, during the peak detection. In pink, the effect of a lowered peak detection threshold is shown. The dashed lines are the DCR considering all recorded events, forming an upper limit.

fig(21)(green, obscured by black). Going lower than the pulse FWHM showed no improvement fig(21)(black).

### 5.6.2 The influence of the integration window

Figure(21) also shows the influence of the size and shape of the integration window on the DCR. The influence of the chosen integration window is most visible in their respective pulse area spectra. Choosing a narrow, symmetrical integration window of 5ns left and right of the peak maxima, the noise peak, or zero-peak, is much more prominent compared to the pulse area spectrum of a symmetrical 10 ns window. This leads to errors in the multi-gauss fitting step, or the fitting will fail altogether. An asymmetrical integration window of 5ns left, 20ns right, to capture the influence of the pulse-tail proved, at first, to be the best solution as there was no visible zero-peak present. The low amplitude pulses are averaged out by the extended integration window to the right of the pulse-maximum. The downside of the asymmetrical window is the shifting of the pulse area spectrum and the fact, that the N p.e. peaks get blurred. The next step was widening the window on both sides. This proved the best solution, since there is no zero-peak visible and the N p.e. peaks are gaussian shaped. Please see section(D) for the respective plots of pulse area spectra of the different windows.

---

### 5.6.3 The influence of the peak detection threshold

---

Choosing an adequate peak-finding threshold is a crucial step. Lowering of the threshold to  $\sim 0.5$  p.e. will cause the peak finding algorithm to misinterpret a lot of noise peaks as actual dark incidents. This, of course, leads to errors in the gain extraction and even if a gain regression line can be extracted, the resulting DCR and OCT will be incorrect. Figure(22)(pink), shows the effect a low peak finding threshold has on the DCR.

## 6 Results

### 6.1 SiPM devices for CTA

Manufacturer	pixel size [mm]	cell size [μm]	coating	connection	specifics	pre-Amp
HPK S12642-1616PA-50 *CHEC-S SiPM	3	50	SR	TSV	no trenches	CHEC-S buffer
HPK LCT5 S13360-6050CS	6	50	SR	wire-bonds	trenches	MS 13V
HPK LCT5 6.975MM-SIL Single	6.915	75	SR	wire-bonds	trenches	MS 8V
HPK 6050HWB-LVR-LCT	6	50	SR	TSV	trenches	MS 13V
SensL FJ60035	6	35	glass	TSV	no trenches	MS 15V

**Figure 23:** List of SiPM devices which results are presented in this work. \*(SR: silicon resin , MS: MiniCircuits , TSV: through silicon via)

SiPM devices for CTA are researched by many different groups, validating different characteristics. Besides the current SiPM for CHEC-S, newly developed prototypes offer a diverse range of pixel- and cellsizes. The majority of the devices are tested in Japan, at the University of Nagoya, conducting in depth analysis of the characteristics over a wide over-voltage range at one static temperature, mainly focusing on PDE and OCT, and their correlation. This correlation of OCT and PDE for all devices determines the candidate for CHEC-S, by comparing the highest PDE at the lowest possible OCT for each device. At MPIK, chosen candidate devices are examined regarding different characteristics and their temperature dependence and as to assist in the final decision by confirming results with a different analysis technique.

The chosen devices include the current CHEC-S device HPK S12642-1616PA-50, from Hamamatsu Photonics K.K., to be implemented in the first prototype camera. It is a previous generation SiPM, which was decided for use in 2014, due to the limited availability in high PDE devices at that time. The manufacturer supplies a 16\*16 channel premounted tile of  $3 \times 3 \text{ mm}^2$  pixels with a cell-size of  $50 \mu\text{m}$ . To emulate the usage in a TARGET module, four  $3 \times 3 \text{ mm}^2$  pixels are electrically connected to form a  $6 \times 6 \text{ mm}^2$  superpixel. The tile is typically coated with epoxy resin, but due to specific requirements regarding the uniformity of the coating, it was replaced with a very thin layer of silicon resin equivalent to later prototypes. The CHEC-S devices electronical connection is realized via the new through-silicon-via (TSV) concept of running a

---

connecting solder through the silicon bulk, instead of wiring on the outside, greatly increasing the fill-factor, but also including some disadvantageous sideeffects later shown.

Additional tested devices include the LCT5 generation from Hamamatsu Photonics K.K., so called due to their low cross talk properties, namely the commercial available S13360-5050CS. This device is the first to include physical trenches between the cells, effectively dividing the cells optically and thus reducing prompt cross-talk probability.

The LCT5 generation also made two prototype devices available for testing at MPIK, the first, HPK LCT5 6.975MM-SIL Single, is a larger iteration with a cellsize of 75  $\mu\text{m}$  and a pixelsize of 6.915 mm, leading to larger fill-factor, which would imply higher PDE, but also DCR and OCT. Being from the LCT5 generation it also includes optical trenches. The second device available is a LCT5 prototype designated 6050HWB-LVR-LCT , LVR meaning low-voltage-range, with the same physical dimensions and properties as the S13360 device but incorporating TSV technology and possibly other unknown deviations.

The final device is a commercially available test-array designated FJ60035 from SensL, pre-mounted on a test-array by the manufacturer. It has the same pixel-size, but a much smaller cell-size 35 $\mu\text{m}$  than the previous mentioned devices, and such a lower fill-factor, and a different coating (glass).

The tests conducted in Nagoya contain many different iterations of the LCT5 generation with varying pixel- and cell-sizes[19]. For a full overview of the considered SiPMs, please refer to section(H).

## 6.2 Hamamatsu S12642-1616PA-50 50 $\mu$ m 3mm

The SiPM by Hamamatsu Photonics designated S12642-1616PA-50 is a 3 mm by 3 mm device. The array uses the TSV technology, meaning there are no wire-bonds present, the electrical connection is realized through the silicon-body. The pixels are coated with a thin film of silicon resin, after the previously used epoxy resin proved not uniform enough. The electrical contact is realized through the TSV technology, establishing connection through the silicon bulk, allowing a tighter fit of the cells, with minimal dead-space. One array consists of 256 pixels, four of which are electrically tied together to form a 6 mm by 6 mm superpixel respectively, due to limited availability at the time of 6x6  $mm^2$  pixels. Simulations showed 6x6  $mm^2$  pixels to be the best choice, balancing FoV and angular resolution.

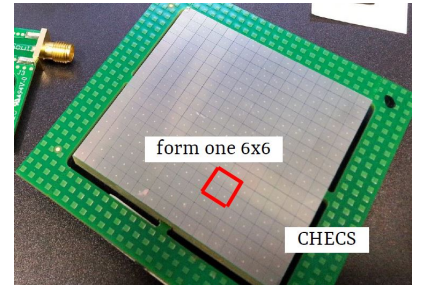


**Figure 24:** CHEC-S tile

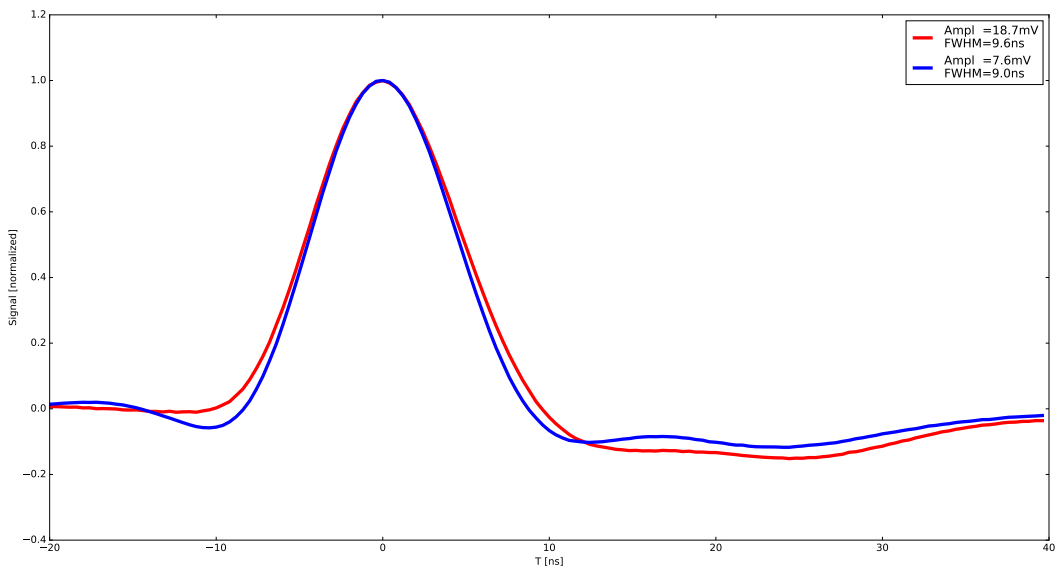


**Figure 25:** The average pulse shape of the 1 photoelectron in blue and the 2 photoelectron pulse in red of HPK S12642 at 25° C and 67.8V, which is around the proposed operating point. Both pulses are averaged over »1000 events and normalized to illustrate possible differences in pulsedshape resulting from the utilized shaping electronics. Both pulses have a FWHM of around 10ns and are nearly free of ringing. The resulting average amplitude of the 1 p.e. pulse is later used to calculate the Gain in [mV/p.e.] instead of [V\*IntWin] by cross-referencing the 1 p.e. amplitude at multiple bias-voltages.

The measurements of the CHEC-S tile concentrate on the array as an as-is device. This means their performance, influenced by external factors outside the actual SiPMs physics, are valid on the assumption, that the way the measurements were conducted is the way the photomultiplier

will later be incorporated into the camera. On that ground, deviations of results of this works from the results of other groups and the manufacturer itself are expected. To clarify this further, for example, it is expected that the tests done at Hamamatsu Photonics where conducted on a single 3 mm pixel, not an array of 256 pixels, where four are tied together. Also divergence of shaping and amplification electronics between the groups will result in some differences. For this test, the CHEC-S tile is connected to the CHEC-S buffer, supplied with  $\pm 4$  V, where the signal is amplified. This signal in turn is then shaped via the CHEC-S shaper, developed by the University of Leicester, see section(4). This whole amplification and shaping chain is simulating later usage in the TARGET modules. Multiple measurements were conducted on many different pixels of the CHEC-S tile, see section(I). The deviation between the pixels showed larger than measurement errors.

### 6.2.1 Gain

As described in section(3.2), the average pulse shape fig(25) is used to convert the relative gain from the analysis procedure to an absolute gain in sensible units. This is necessary, because the analysis aims to use pulse-area rather than -height, which results in this relative gain being in units of  $V \times \text{timebins}$ , instead of voltage. Figure(26) shows the gain after conversion. A lower gain with increasing temperature is expected and described in detail in section(3.2). In short, increased lattice movement due to higher temperature hinders photoelectron transport. The effects visible at extreme bias-voltages at both ends are partially analysis related. The gain of a SiPM is expected to be linear over bias-voltage at a constant temperature.

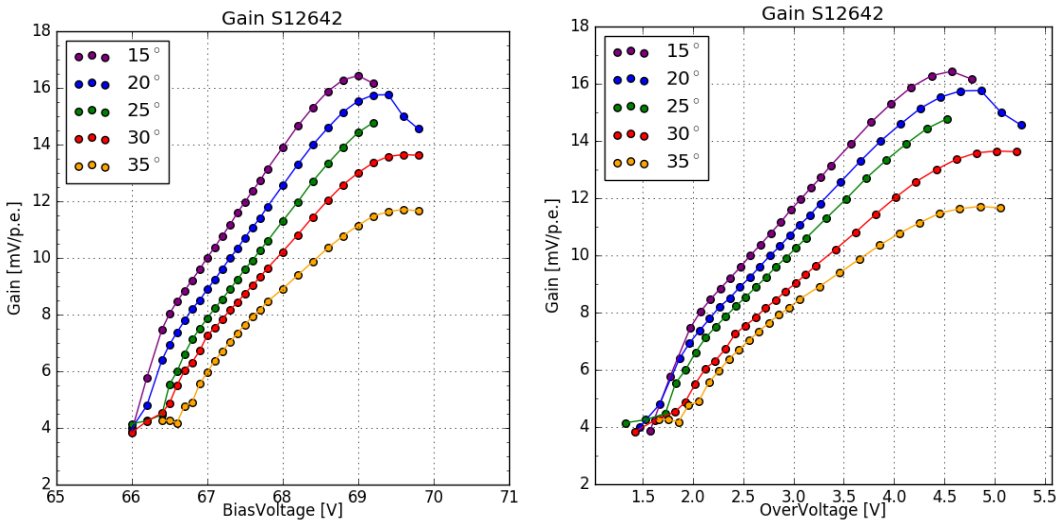


**Figure 26:** Gain of the HPK S12642 pixel, plotted against over-voltage , bias-voltage and temperature.

In the lower regime at bias-voltages  $\sim 66.5$  V the gain is low compared to the noise, so the analysis struggles to pick up pulses. Depending on the determined peak-finding threshold, the analysis is suspected to interpret noise peaks as 1p.e. peaks at an increasing rate, the lower the

overvoltage is. This is visible in the sudden break in linearity at 30 °C and 35 °C , where the gain is almost in a plateau, due to this effect. The roll-over of the gain at the highest bias-voltages is in part a result of a voltage drop across the bias resistor occurring, because of high current flow through the SiPM. At higher temperatures, and therefore higher dark rates, the effect occurs at lower over-voltages. A second influence is caused again, by the noise at over-voltages of ~5 V, which is very high compared to the proposed point of operation at over-voltages of ~3 V. The same threshold is again counting the now increased noise peaks as 1p.e. peaks, but due to the abundance of 1p.e. pulses this results in an apparent lowering of the gain.

### 6.2.2 Dark Count Rate

The DCR is expected to increase with temperature, which is the case for S12642 shown in Figure(27) and to follow a nearly linear progression, a sudden turn-up or turn-down of the DCR would be analysis related. The turn-up at a certain point is visible in fig(27), particularly for 15° C (purple) and 20° C (blue) respectively. At 15° C and an over-voltage of ~4V, the DCR starts to deviate from the previously linear behaviour. It starts to rise more rapid than before, the OCT at that point is also very high; exceeding 50% fig(28) (left). For the higher temperatures of 25° C (green) and 30° C (red) this critical point is not reached, so the effect is barely, if not at all visible. At 35° C (yellow), due to the high rate of 9-10 MHz, slight heating of

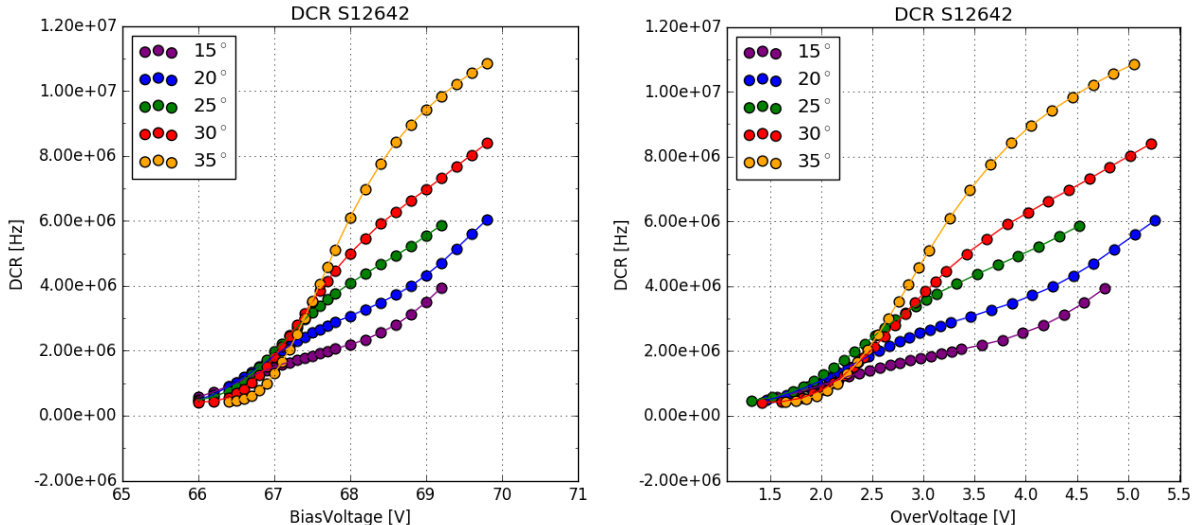


**Figure 27:** Dark Count Rate of the HPK S12642 pixel, plotted against over-voltage , bias-voltage and temperature. DCR at 2 - 3 MHz from datasheet at operation voltage = 2.4V and 25°C measured by current.

the SiPMs surface could also affect the DCR through a slight shift of the temperature upwards, away from 35° C . So that the DCR declared at 35° C is in reality the rate at higher temperatures.

At the lowest end of the bias-voltage range, part of the found 1p.e. pulses are suspected

to be noise related. So the DCR changing to a plateau is expected. This is also due to the fact, that the measurements are done with a fixed bias-voltage range. Due to the increase of the breakdown-voltage with rising temperature, part of the measured bias-voltage range corresponding to a very low over-voltage, attributes to this effect. In order to reliably measure beyond an overvoltage of 2.5V in the lower range, the noise would need to be improved.

### 6.2.3 Optical Cross Talk

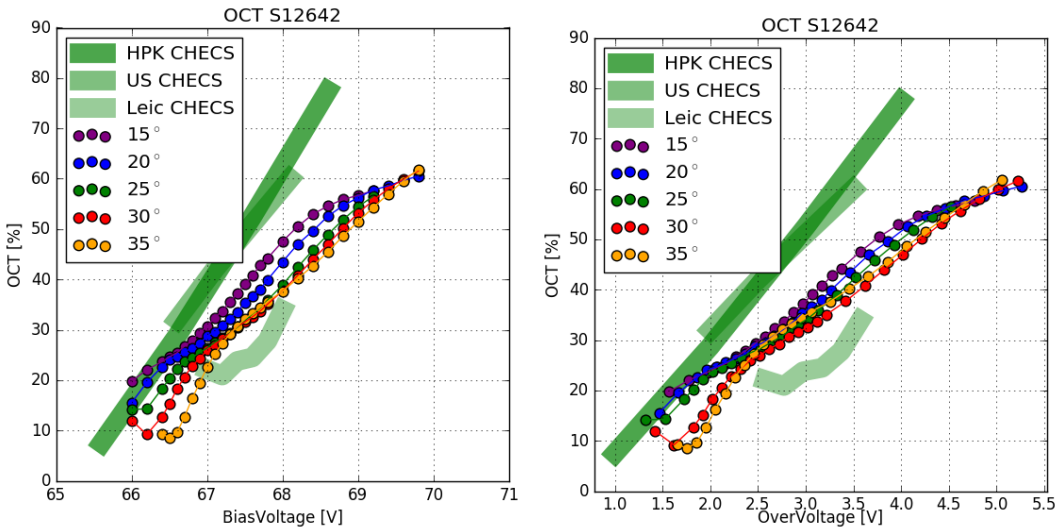


**Figure 28:** Optical Cross Talk of the HPK S12642 pixel, plotted against over-voltage , bias-voltage and temperature.

The OCT is expected to be linear and independent from temperature. This is confirmed for HPK S12642. Minor deviations from that are probably due to slight errors in the breakdown-voltage calculation from the gain regression line. At higher DCR the multi incident probability rises, an event of two simultaneous dark counts could easily be interpreted as a dark event + cross-talk. This leads to a systematic increase in OCT at the higher DCR, for examples see section(K).

The deviation of 30° C and 35° C below an over-voltage of 2V stems from the way the gain regression line is used to calculate both DCR and OCT. At higher temperatures the lower voltage range consists partly of noise, so using the gain regression line to calculate the OCT at those low voltages leads to the visible effect of the first few datapoints of 30° C and 35° C.

The deviations between the different groups results at 25° C (green) are caused by 4 major factors. Firstly the difference in the tested device. While the device measurements in this work has every four  $3 \times 3 \text{mm}^2$  pixels electrically tied together, the way the device will later be implemented into CHEC-S, the groups in the US[17] and Hamamatsu Photonics[16] are likely to run tests on one  $3 \times 3 \text{mm}^2$  pixel only. Secondly a slight difference in amplification and shaping electronics is suspected. The measurements conducted in this work as well as the measurements of Leicester are done with the same shaper and buffer configuration. The difference here is,

---

thirdly, measurements are done with dark counts only, while measurements from other groups are conducted with a pulsed light source and reading out timed windows. This causes the results from Leicester to be difficult to compare against, their surface temperature of the SiPM is likely much higher than 25° C, and thus, a misinterpreted breakdown-voltage at 25° C causes a shift of the OCT to the right. Lastly the difference in actual data taking and analysis procedure must be mentioned, also this is only of minor concern, as we will see with other measured devices.

### 6.3 Hamamatsu LCT5 50 $\mu$ m 6mm

The SiPM designated HPK S13360 6050CS fig(29) is an LCT5, meaning Low Cross Talk 5th iteration device from Hamamatsu Photonics. It is one of the most promising candidates for later usage in CHEC-S. It has a pixelsize of 6 mm consisting of 14400 cells with a cellsize of 50 $\mu$ m. The present device and its similar iterations are the first to incorporate trenches bordering each cell, effectively insulating the cells and reducing the prompt OCT. Tests are done with a single pixel only, in contrast to measurements done on S12642. It is mounted on a ceramic chip and coated with a silicon resin that is UV-transparent. Wire-bonds supply the electrical contact. A similar, but not tested, device from the same generation uses TSV technology.

## LCT5 6mm

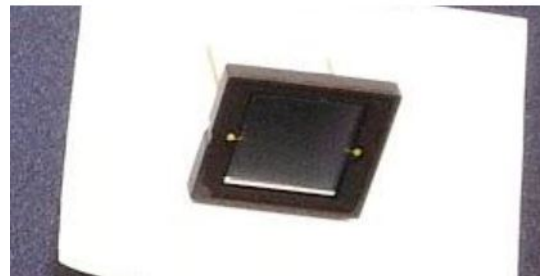


Figure 29: HPK S13360 6050CS pixel

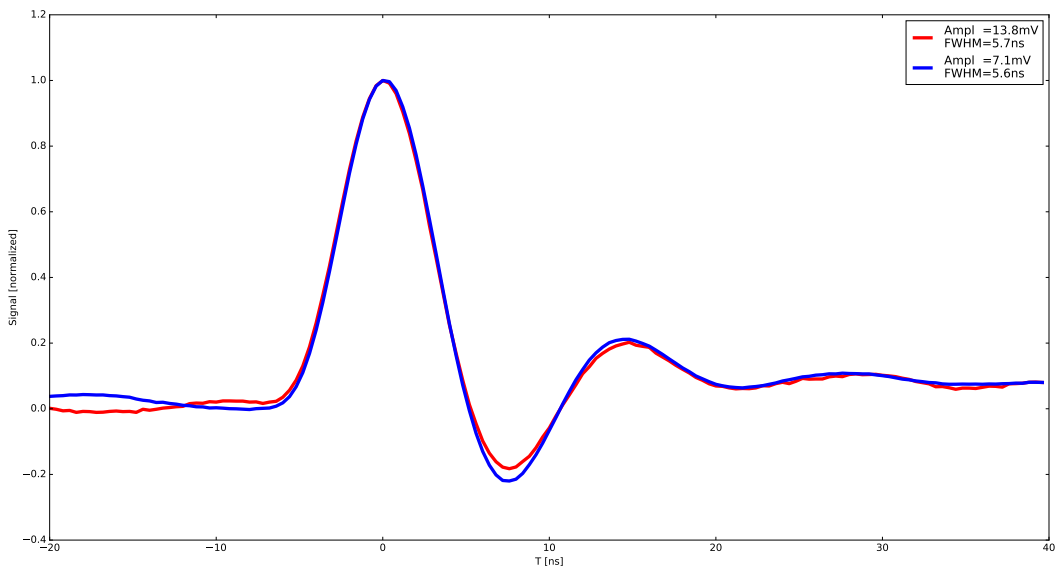
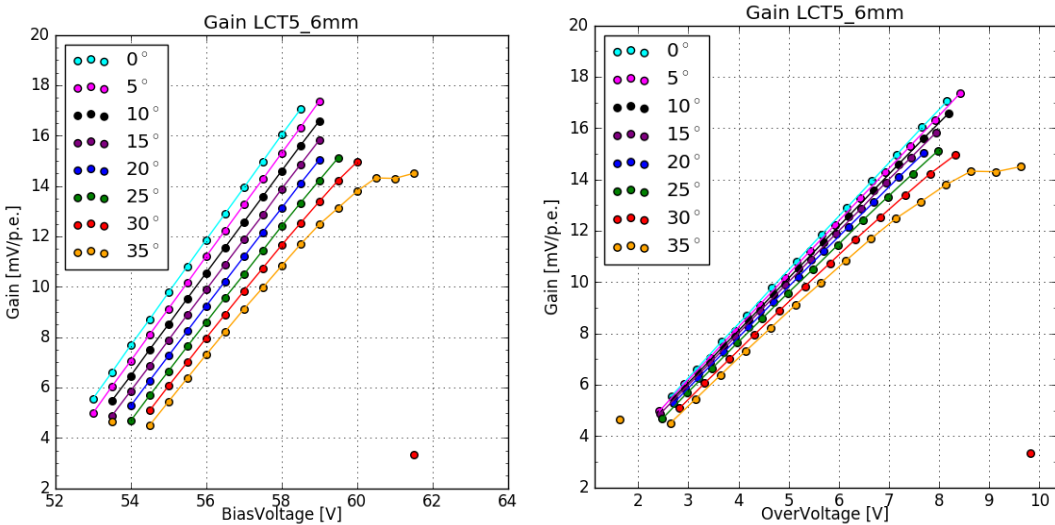


Figure 30: The average pulse shape of the 1photoelectron in blue and the 2photoelectron pulse in red of HPK S13360 6050CS at 25° C and at point of operation. Both pulses have a FWHM of around 5ns and ring for approximately 20ns with an undershoot of 20%.

The layout of the single pixel test device made external amplification necessary. An amplifier from MiniCircuits was supplied with 13V during this test. Shaping of the pulse is conducted by a CHEC-S shaper, modified to fit the new unshaped pulse. The pulse shape fig(30) makes the pulses appear much harder to analyze, due to the possibility of events occurring during the ringing window. This assumption proved untrue, due to the devices low DCR and OCT, resulting in a low multi incident probability.

### 6.3.1 Gain

The gain of the LCT5 50 $\mu$ m 6mm device is clearly linear with some minor outliers at 30°C. The same effect as with S12642 is visible at 35°C, again counting noise peaks as 1p.e. peaks, resulting in an apparent lowering of the gain and the slope changing over into a plateau. In figure(31)(left) the gain is shown, plotted against over-voltage. It is still dependent on temperature, but due to reliable breakdown-voltage calculation, the spread is much smaller than, if plotted against bias-voltage. The same conversion is done to transform relative gain into an absolute gain with sensible units. When parametrized with over-voltage, the gain is essentially temperature independent.



**Figure 31:** Gain of the HPK S13360 pixel, plotted against over-voltage , bias-voltage and temperature.

### 6.3.2 Dark Count Rate

The DCR of two similar HPK S13360 devices is shown in figure(32). The bars show the difference between the two devices, the results of one device is used as a reference, while the deviation is illustrated with the filled bar. The DCR of HPK S13360 follows the expected behaviour, mostly linear in the significant range and rising with increasing temperature. Below an over-voltage of 2.5 V the gain is suspected to be low enough for larger noise peaks to be misinterpreted as events. Thus the regression line calculation is unreliable in this range.

The turn-up at high over-voltages is most prominent at 0 °C(teal) after an over-voltage of 9 V. This is also the point where the OCT rises very rapidly. It is not pulse related, being at a DCR of 1 MHz it would be visible earlier for higher temperatures, but their slope is linear.

The datasheet values from the manufacturer cover a large range of the DCR at an over-voltage of 3V making it difficult to compare against, the manufacturer determines the DCR by measuring the current.

A standard counting error of the DCR is largest in the lower bias-voltage range. Despite the low DCR at an over-voltage of 2 V of  $\leq 0.5$  MHz, in a measurement window of  $100\ \mu\text{s}$  there are still  $\geq 50$  pulses detected. This means an experimental run of 500 segments of the  $100\ \mu\text{s}$  measurement window shows a standard counting error in the DCR of 0.003 MHz, below 0.1%. This is lower than errors related to analysis or data acquisition and not visible given the size of the datapoints.

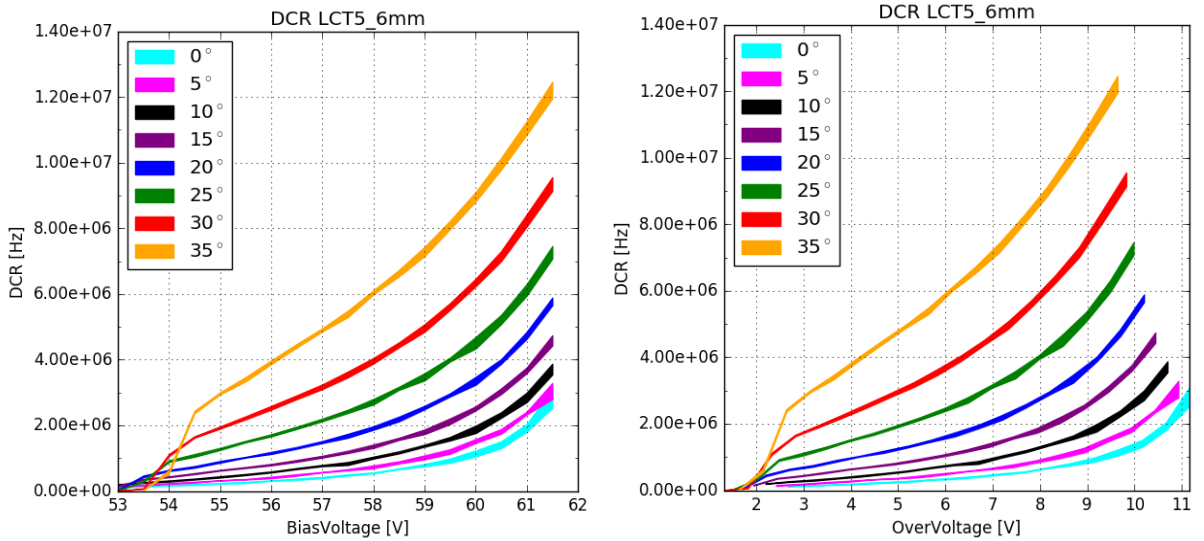


**Figure 32:** Dark Count Rate of the HPK S13360 pixel, plotted against over-voltage , bias-voltage and temperature. The Datasheet values cover a very large range between a DCR of 2 - 6 MHz at an over-voltage of 3 V at  $25^\circ\text{C}$ , to wide to compare to reliably, and is measured by current.

### 6.3.3 Optical Cross Talk

The measurements of the HPK S13360 SiPM done at the Nagoya University[19], Japan fig(33) (faded green bar), correlate very strong with results from this work of the OCT in the over-voltage range between 2.5 V and 9 V. The OCT in this range is linear and independent from temperature, with minor deviations attributed to the breakdown-voltage calculation from the regression line, causing the horizontal shift. In contrast to the dark counts measurements in this thesis, the measurements at Nagoya University followed a pulsed light source approach, reading out a time-window after the laser incident. This could have consequences, since OCT with a longer delay time could be missed. Deviations below an over-voltage of 2.5 V are expected, they are very likely caused by the regression line calculation being unreliable in this range due to the analysis method misinterpreting noise as dark count events. Above an over-voltage of 9 V, which is also the point of the turn-up of the DCR, the OCT is no longer linear and the deviation from the results of Nagoya University increase very rapidly. The rapid increase in both DCR

and OCT is suspected to be caused by the over-voltage reaching ranges, where interpretation of noise as a 1 p.e. pulse becomes more likely. This, joint together with the usage of the MiniCircuits amplifier supplied with 13 V, makes false interpretation of noise as pulses even more likely. These two reasons in conjunction are suspected to be responsible for both, the sudden rise of the DCR as well as the deviation of the OCT from linearity and the results of Nagoya University, above over-voltages around 9V. In summary, the correlation between the two measurements, conducted by two different methods of data acquisition and analysis, is evident.

The S13360 series is the first to incorporate physical barriers, called trenches, effectively insulating the cells from each other. This drastically reduces the prompt cross-talk, while increasing the percentage the delayed cross-talk contributes to the overall cross-talk shown. This could also be the reason for the up-turn, compared to data from the University of Nagoya; at higher over-voltages the contribution from delayed cross-talk is higher[14]. With the trenches effectively reducing the prompt cross-talk and the difference in analysis, the effect could be partially explained by increased contribution of the delayed cross-talk. More on this subject in section(7).

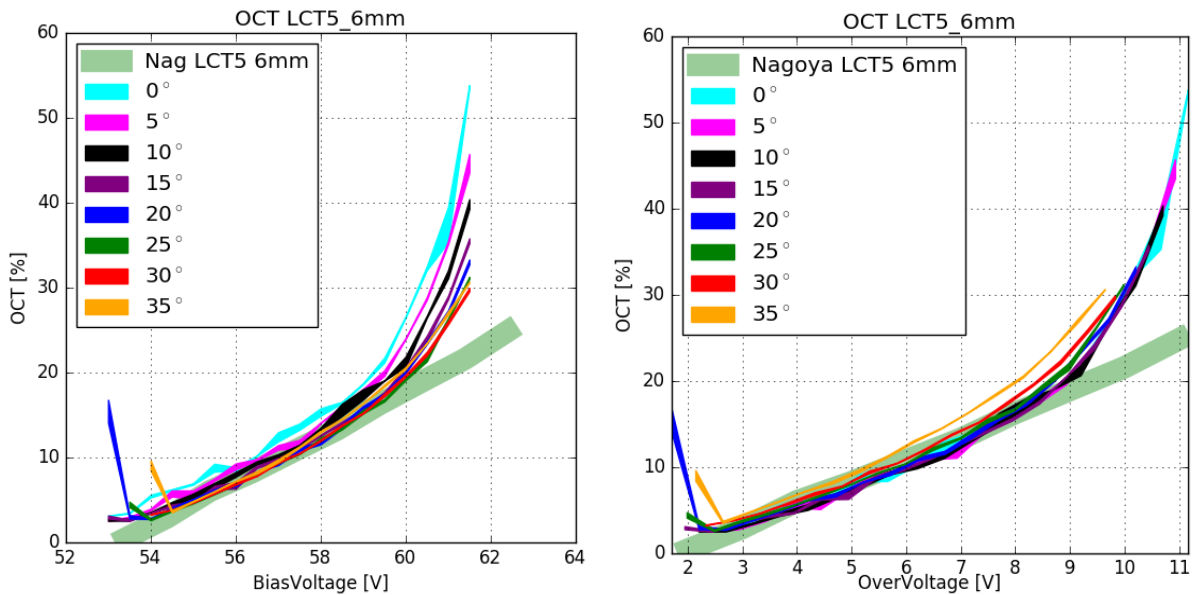


**Figure 33:** Optical Cross Talk of the HPK S13360 pixel, plotted against over-voltage , bias-voltage and temperature.

## 6.4 Hamamatsu LCT5 75 $\mu$ m 7mm

The device named 6.975MM-SIL Single (fig(34)) is a larger LCT5 prototype SiPM of the same design as S13360-6050CS. With an increase in cellsize to 75 $\mu$ m, the device gains a higher fill-factor than 50 $\mu$ m devices. The pixel-area is also expanded to 6.915x6.915 mm<sup>2</sup>, which will result in a higher fill-factor (less deadspace), both size increases together will presumably result in a higher PDE but also a higher OCT. Since it is a prototype device, there is limited data from datasheets. The ID number suggests, that it is also a wire-bond device with a UV-transparent silicon-resin coating. It is also a single pixel test device, so external amplification is necessary with the MiniCircuits PreAMP, supplied with 8V during this test. The signal is shaped by a differently modified CHEC-S shaper, which results in a pulse shape similar to S12642, but with a much lower amplitude (fig(35)).

## LCT5 7mm



Figure 34: HPK LCT5 7mm pixel

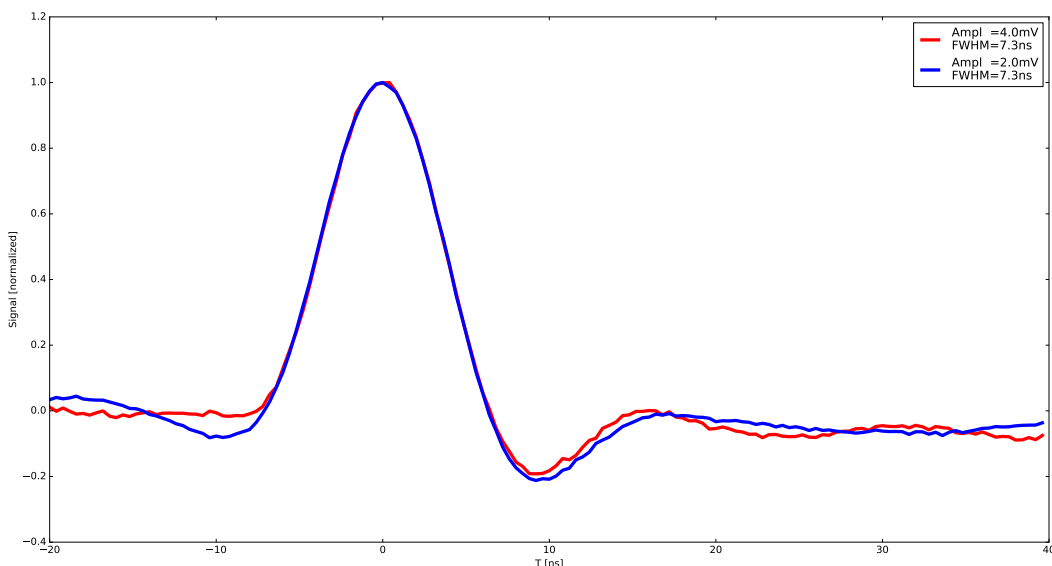
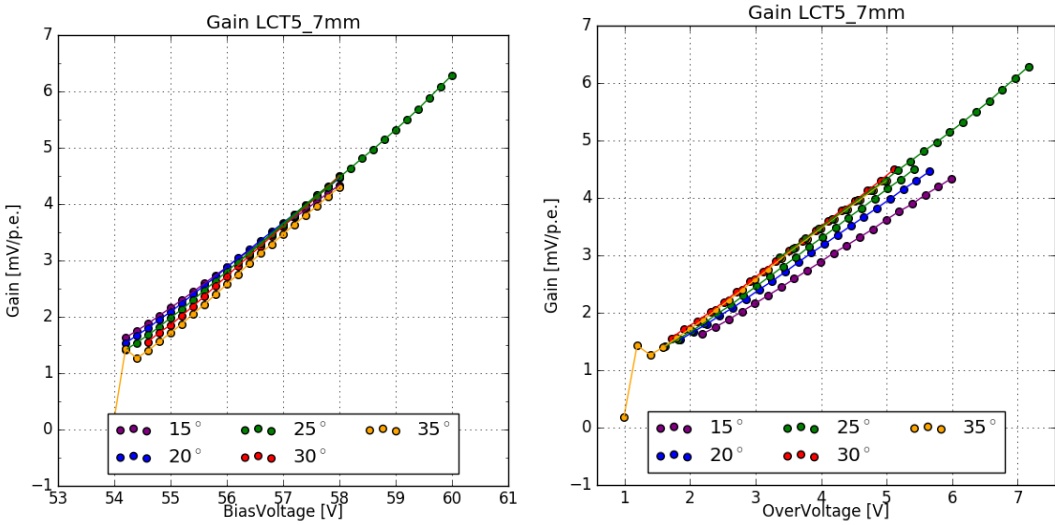


Figure 35: The average pulse shape of the 1 photoelectron in blue and the 2 photoelectron pulse in red of HPK LCT5 7mm at 25° C and at point of operation. Both pulses have a FWHM of around 7ns and an undershoot of 20%, with no ringing.

### 6.4.1 Gain

Figure(36) shows the gain of the LCT5 7mm device. Two sets of measurements are done for 25 °C to extend the measured range. The first set of measurements covers the lower over-voltage range, where the low gain makes external amplification necessary, realized with a MiniCircuits



**Figure 36:** Gain of the HPK LCT5 7mm pixel, plotted against over-voltage , bias-voltage and temperature.

PreAMP supplied with 8 V. The lowest possible amplification of the PreAMP is chosen, so that reaching the point of saturation of the oscilloscope input is as late as possible as the over-voltage rises. Saturation of the oscilloscope occurs due to the possibility of generating very large p.e. ( $>10$  p.e.) events at the higher over-voltages, which are saturating the input. Joint together, the LCT5 7mm device and the MiniCircuits PreAMP at 8 V reach this point at an over-voltage of  $\sim 6$  V. In figure(36) the results from the lower range measurement are displayed as the lower-range green line extending between an over-voltage of 1.6 V to 5.4 V. The configuration for the second test removes the PreAMP from the setup, which makes the lower over-voltage range inaccessible, but extends the range to higher over-voltages. This configuration reaches the point of saturation at an over-voltage of  $\sim 8$  V. The higher range measurement results are displayed as the second green line ( $25$  °C) extending from 3.4 V to 7.2 V over-voltage in figure(36). There is a clearly visible overlap of the two measurements between  $\sim 3.4$  V and  $\sim 5.4$  V . It also seems, that the gain dependency on temperature is reversed. While for all other devices, the gain lowers with rising temperatures, the LCT5 7mm device seems to show inversed behaviour. This inverse behaviour is caused by the calculation of the breakdown-voltage from the gain-regression line and is likely an error. Plotting the gain versus bias-voltage, however, shows the expected behaviour of the gain.

#### 6.4.2 Dark Count Rate

The behaviour of the DCR of the HPK LCT5 7mm device is shown in figure(37) and is as expected. It follows a linear progression in the relevant range and increases with rising temperature. I suspect the over-voltage range above  $\sim 2.5$  V to be relevant. The extended range measurement at  $25$  °C confirms this behaviour. LCT5 7mm shows a linear DCR over an over-voltage range of 4 V. The faded green bar in figure(37) shows results from measurements undertaken

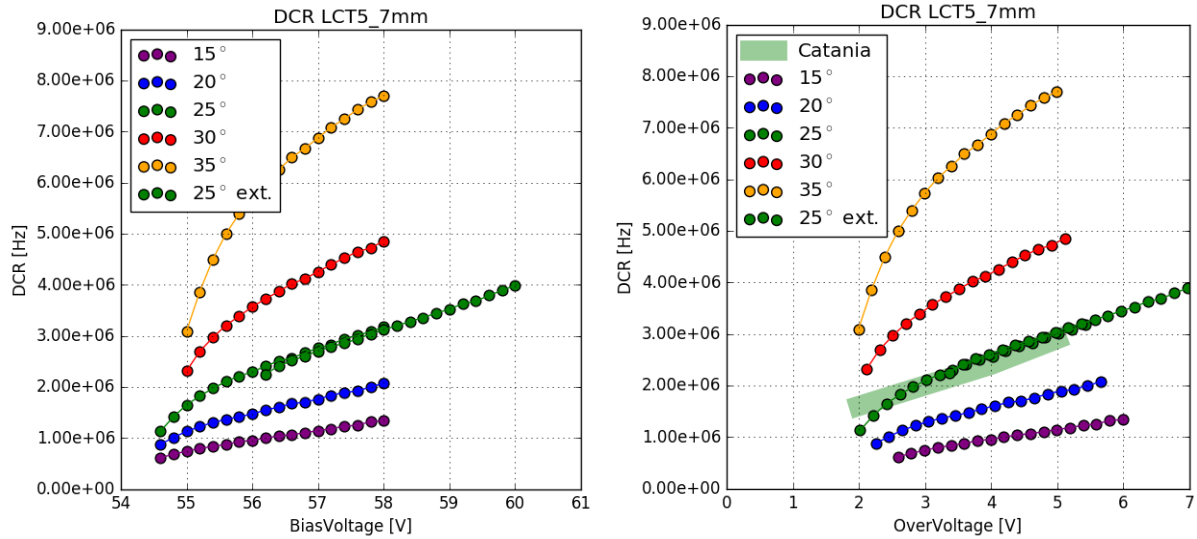


**Figure 37:** DCR of the HPK LCT5 7mm pixel, plotted against over-voltage , bias-voltage and temperature.

by the Department of Physics and Astronomy at the University of Catania. Those measurements were conducted on the exact same device, which is an important point, but with a different method of data acquisition and data analysis. Analysis techniques are discussed in section(7). The correlation between the two experiments is evident, although there is differences in the acquisition and analysis process.

#### 6.4.3 Optical Cross Talk

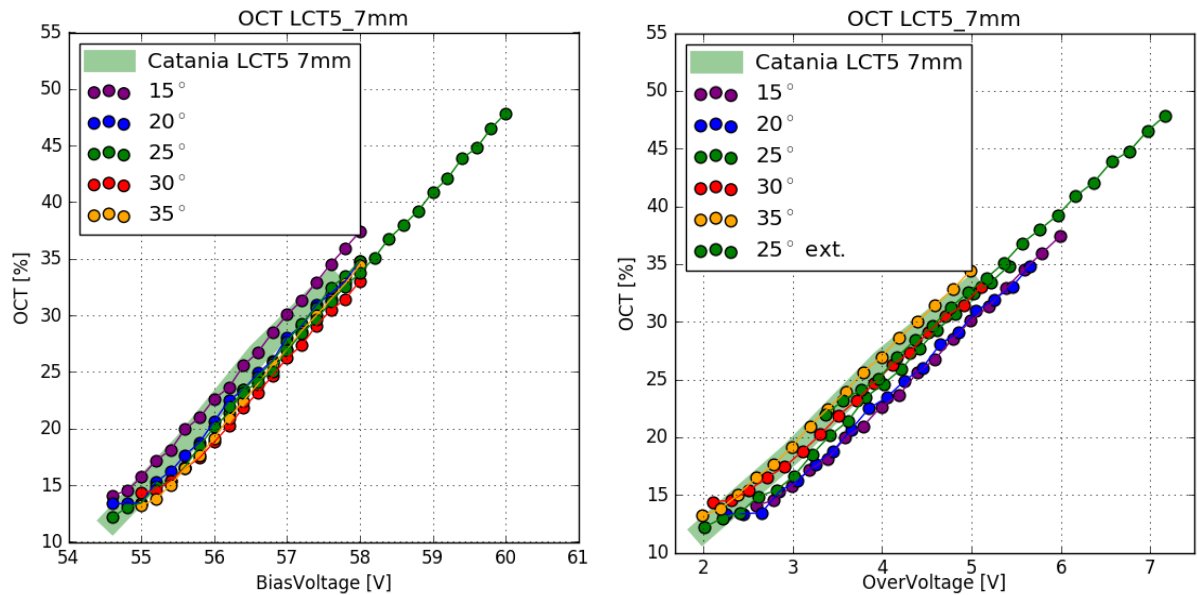


**Figure 38:** Optical Cross Talk of the HPK LCT5 7mm pixel, plotted against over-voltage , bias-voltage and temperature.

---

The OCT is expected to be linear and independent from temperature. This is the case in the, in section(6.4.2) established, relevant over-voltage range of above  $\sim$ 2.5 V (fig(38)). Minor deviations are attributed to the calculation of the breakdown-voltage from the gain-regression line. The over-voltage is calculated from the former and the supplied bias-voltage, which in turn causes a slight horizontal shift. With that, comparing the results from this work to the measurements at 25 °C (faded green bar) from the University of Catania shows a strong correlation.

## 6.5 Hamamatsu LVR 50 $\mu$ m 6mm

The SiPM by Hamamatsu Photonics with the designation 6050HWB-LVR-LCT is a special prototype of the LCT5 design. LVR is an abbreviation of Low Voltage Range, meaning the device is meant to be operated at much lower operation voltages than other LCT5 devices. It has the same physical size as an LCT5 device (S13360 section(6.3)), a pixelsize of 6mm pixel with a cellsize of 50 $\mu$ m. The recommended point of operation however is  $\sim$ 15V below that of the S13360 device, specifically at 40.2 V(LVR) instead of 54.7 V (S13360). It uses the TSV technology for electrical connection.

The unshaped signal is similar to other LCT5 devices, therefore using the a modified CHEC-S shaper is feasible in this case, resulting in a similar pulse shape fig(40). After that the signal is amplified with the same MiniCircuits PreAMP supplied with 8.5V.

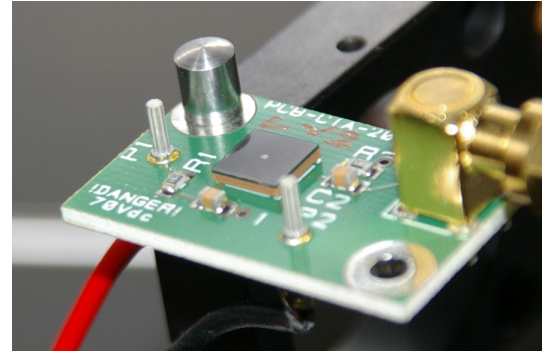


**Figure 39:** HPK LVR 6mm pixel

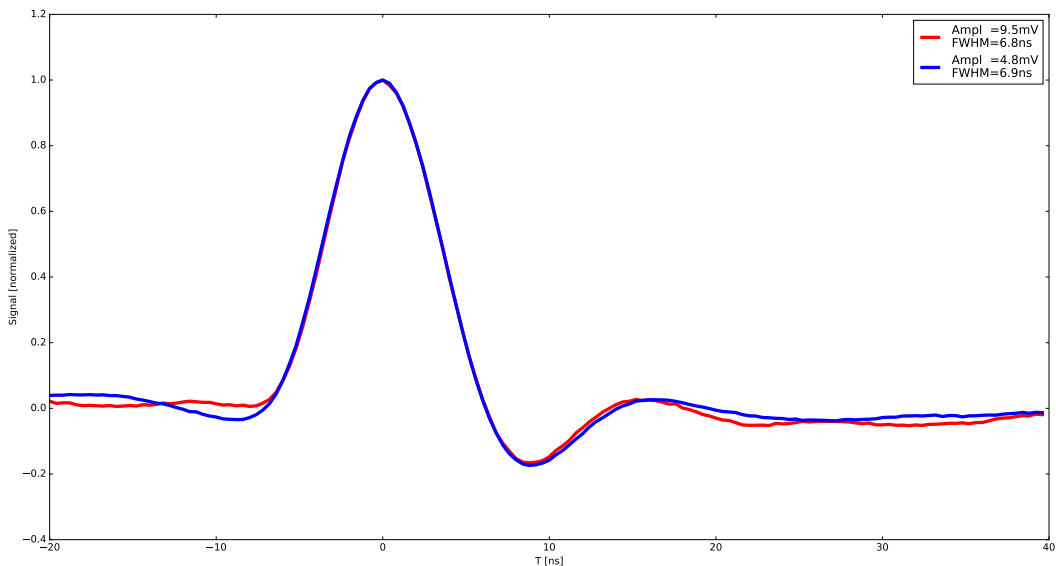


**Figure 40:** The average pulse shape of the 1photoelectron in blue and the 2photoelectron pulse in red of HPK LVR 6mm at 25° C and at point of operation. Both pulses have a FWHM of around 7ns and an undershoot of 20%, with no ringing.

### 6.5.1 Gain

Figure(41)(right) shows the gain of the LVR 6mm device. It is, as expected, linear over a long range and nearly independent of temperature when parametrized with over-voltage. The flattening of the slope to a plateau shape in the lower over-voltage range is caused by noise

pollution. Only taking into account the linear region, limits the range, where the results are relevant to an over-voltage range above  $\sim 2.5$ V. Saturation of the oscilloscope in this range is not visible, but a check with a more expanded range revealed, that the point of saturation of the oscilloscope is at an over-voltage of  $\sim 5$ V. The apparent overlap of the gain, when plotted against over-voltage, is based on the calculation of the breakdown-voltage being very reliable due to the large linear range. Plotted versus bias-voltage fig(41)(left) the expected behaviour of the gain, lowering with increasing temperature, is visible.

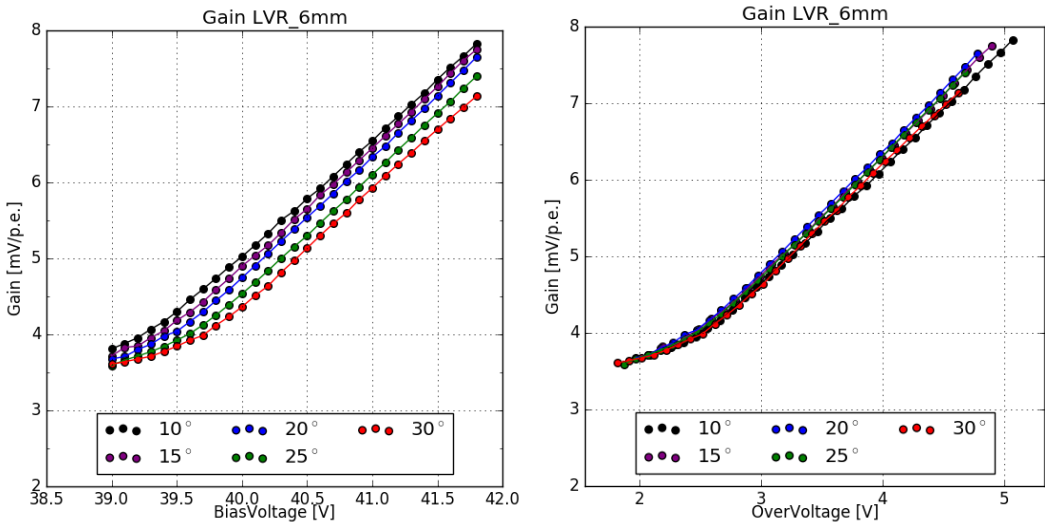


**Figure 41:** Gain of the HPK LVR 6mm pixel, plotted against over-voltage , bias-voltage and temperature.

### 6.5.2 Dark Count Rate and Optical Cross Talk

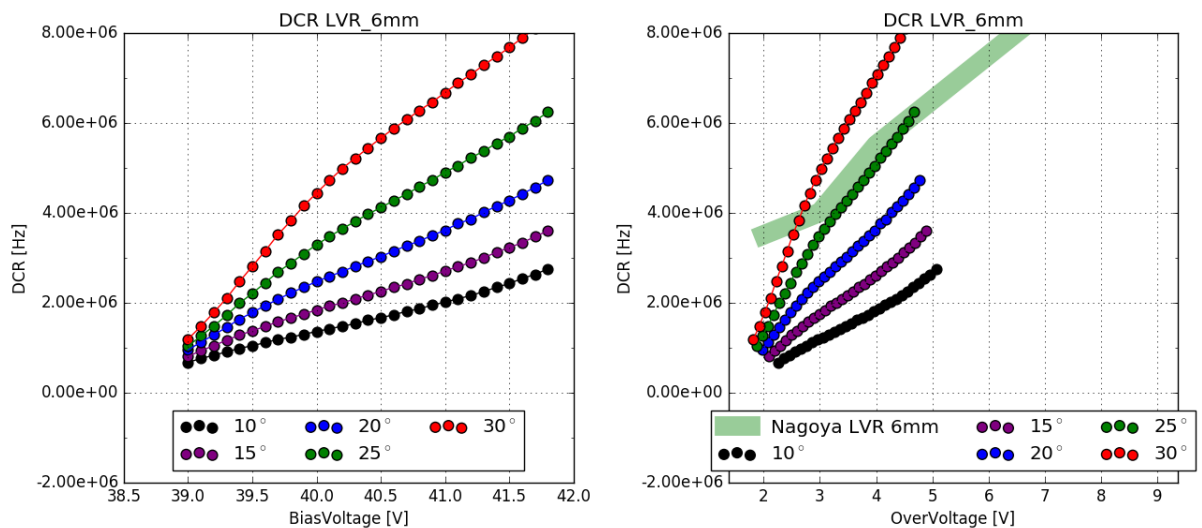


**Figure 42:** Dark Count Rate of the HPK LVR 6mm pixel, plotted against over-voltage , bias-voltage and temperature.

The DCR fig(42), taking into account only the relevant over-voltage range of  $>\sim 2.5$ V seems to correlate, while the resulting OCT fig(43) is very high compared to results from the University of Nagoya, which also cover a much wider range. Only taking into account the previously established relevant over-voltage range of  $>\sim 2.5$ V, the resulting OCT is a factor of two higher. The device being a prototype, it could be the case, that there are physical differences, a difference in coating, which combined with the TSV technology could lead to the present uncorrelation[20]. This uncertainty is a contrast to results from previous devices, where strong correlations between different groups and measurement techniques are evident.

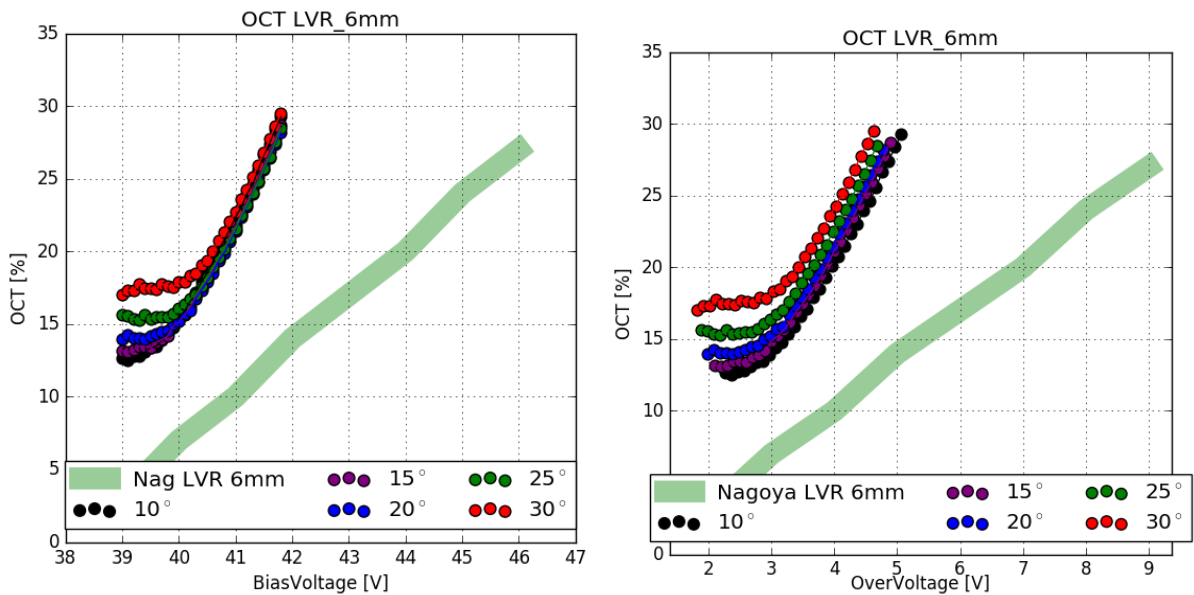


**Figure 43:** Optical Cross Talk of the HPK LVR 6mm pixel, plotted against over-voltage , bias-voltage and temperature.

## 6.6 SensL FJ60035 6mm 35 $\mu$ m

The SiPM by SensL with the designation FJ-60035 is another candidate device for use to populate the focal plane of CHEC-S. It is also a 6mm device, but with a much smaller cellsize of 35 $\mu$ m, using the TSV technology, so there are no wire-bonds present. This results in 22292 cells on a single pixel with a fill-factor of 75% . It is coated with plain glass. The recommended point of operation is around 30V bias-voltage, lower even than that of the HPK LVR prototypes. The device is, by the manufacturer, pre-mounted on a printed circuit board, called a test array. This test array contains a fast output, that directly couples to the cells, and a slow output, conventionally read out via the quench resistor. For the conducted tests, I used the fast output amplified with the MiniCircuits PreAMP supplied with 12V. The SensL device was the first device measured, therefore the analysis procedure used was an older iteration compared to the procedure for the Hamamatsu devices.

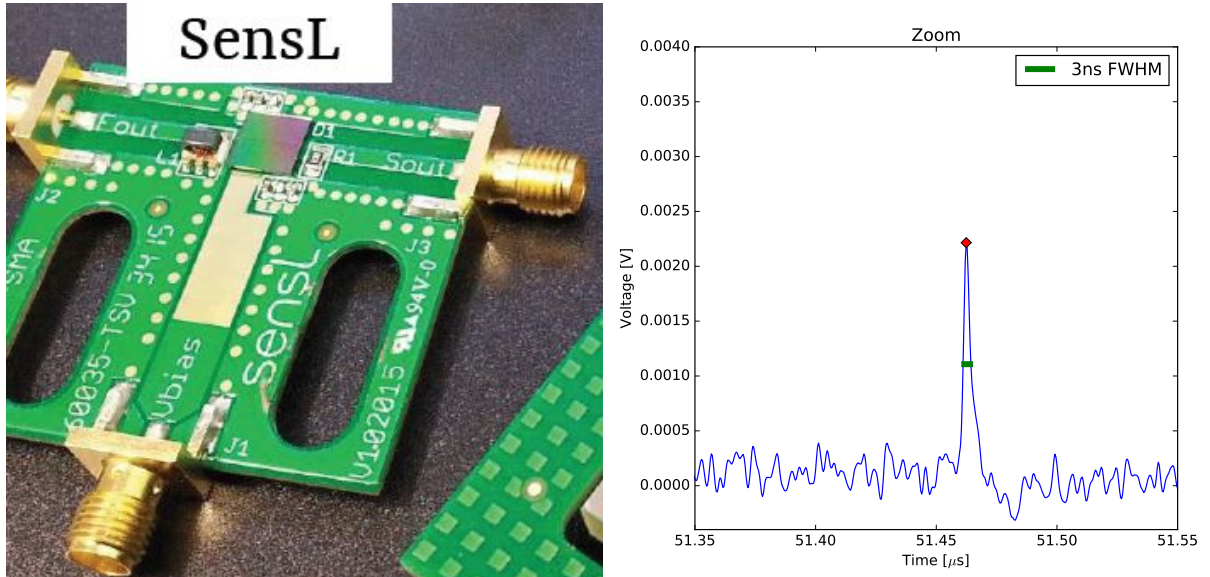


**Figure 44:** SensL Test Array and the average pulse shape at a bias-voltage of 29V

### 6.6.1 Gain

Evaluating the SensL pulse area spectra shows the 1 p.e. position and  $\Delta$ p.e. overlapping, so using the older analysis iteration introduced no error when evaluating the gain of the SensL device. It is clearly linear over a wide temperature range from -5°C to 35°C over an over-voltage ranging from 2V up to 8V. When plotted versus over-voltage the spread of the gain is even tighter signaling slight temperature independency, but still following the expected behaviour of decreasing with increasing temperature.

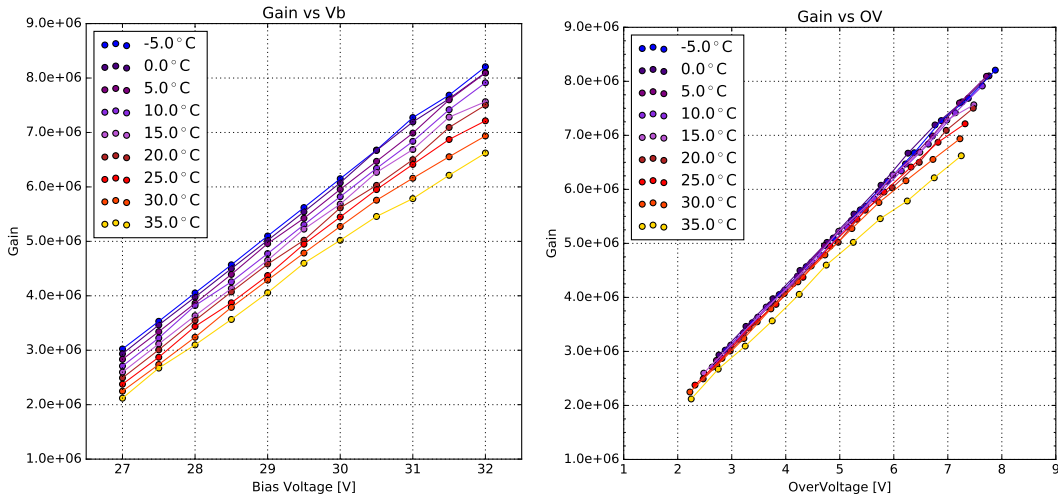


**Figure 45:** Gain of the SensL FJ-60035 test array, plotted against over-voltage , bias-voltage and temperature.

### 6.6.2 Dark Count Rate and Optical Cross Talk

The DCR fig(46) also shows the expected behaviour. At very low temperatures the changes in rate over the over-voltage range is minimal. Increasing the temperature shows a rapid increase in thermally induced dark counts. The OCT fig(47) on the other hand is independent of the device temperature, also as expected. In both cases, the values agree with values derived from the datasheet.

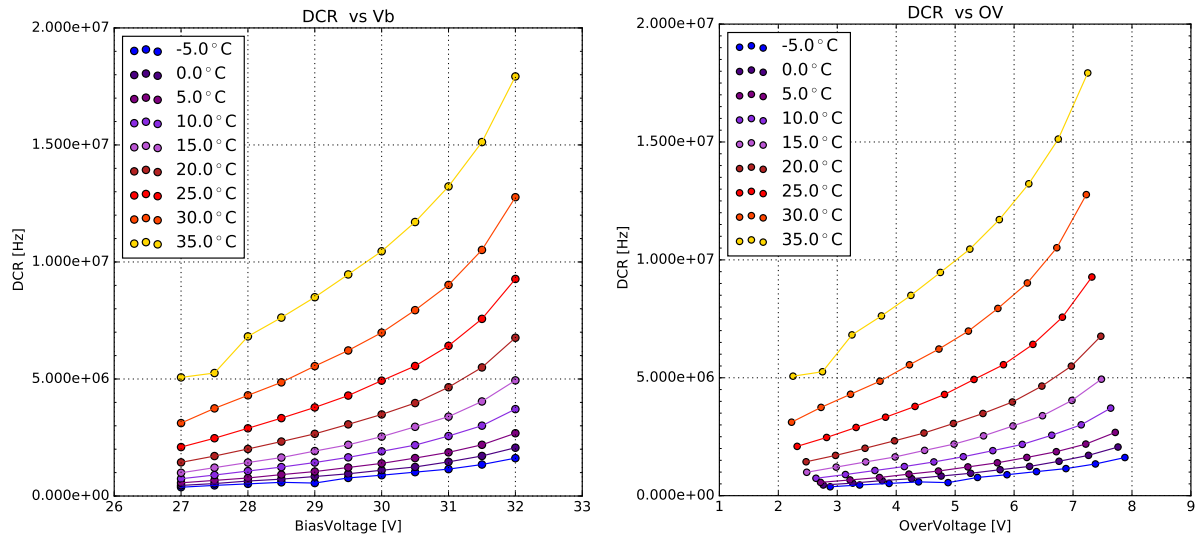


**Figure 46:** Dark Count Rate of the SensL FJ-60035 test array, plotted against over-voltage , bias-voltage and temperature. Datasheet values at  $V_{OV} = 2.5$  V and 5 V at 25 °C are between 1.6 - 2.7 MHz and 2.9 - 5.7 MHz respectively.

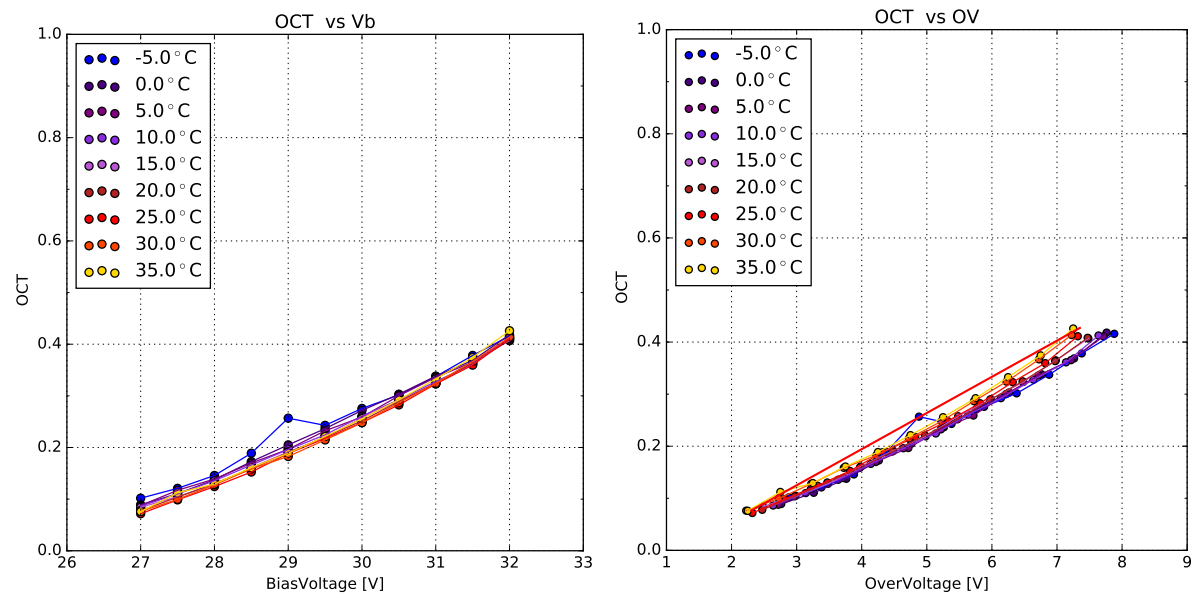


**Figure 47:** Optical Cross Talk of the SensL FJ-60035 test array, plotted against over-voltage , bias-voltage and temperature. OCT results of Nagoya University marked by the red line. Datasheet values at  $V_{OV} = 2.5$  V and 5 V at 25 °C are 7% and 22% respectively.

---

## 7 Comparison

---

A comparison of the performance of all devices is the significant step for choosing the SiPM later to be used in CHEC-S. In order to do this, all measured characteristics are compared versus over-voltage. Operation of the CHEC-S camera in GCT will come down to a decision between two operational points. The first point will be marked by an OCT of under 15%. Every other attribute of the SiPM at this over-voltage is then compared. This point will trade off precision for efficiency, a lower OCT makes real event detection easier, on the other hand, a lower PDE may forfeit a lot of potential data.

The second point of operation is marked at the highest achievable PDE. This work does not involve PDE measurements, other groups are commissioned to determine the point of highest PDE. This point will assure the highest detection of event photons, but will trade that for an increase in detector noise, due to the higher DCR and more importantly OCT.

Comparing results to other groups is shown in figure(48), using different experimental setups and procedures and therefore also entirely different analysis techniques. The groups, that evaluate SiPMs, the University of Leicester, the University of Nagoya and the University of Catania, are all conducting fixed window readout of the SiPM after an expected light-pulse from a flasher-LED or pulsed laser.

---

### 7.1 Dark Count Rate

---

Comparing the DCR of the measured devices and results from the other groups is shown in figure(48). The differences in analysis procedure will only have a slight impact on the presumed DCR, since all experiments record dark-count events over their respective acquisition time windows. On the other hand, if the readout window is sufficiently small, events originating from afterpulsing or delayed crosstalk could be missed. All groups experience the same multi-hit coincidence, meaning a light-event or dark-event coinciding with another, forming a (partial)multi p.e. event.

Only two of the five measured devices have measurements result from other groups to compare, as it is not their focus. In the case of both, the LVR 6mm and the LCT5 7mm results can be discussed to some degree as matching. While the correlation is obvious for the LCT5 7mm device figure(48)(red), where the covered measurement range in this work exceeds the external results, while matching and showing the same trend, the LVR 6mm results deviate. Between an over-voltage of 3 V and 4 V the results overlap, the trend on the other hand is obviously different. Additionally the limit on the higher range due to noise makes it impossible to compare

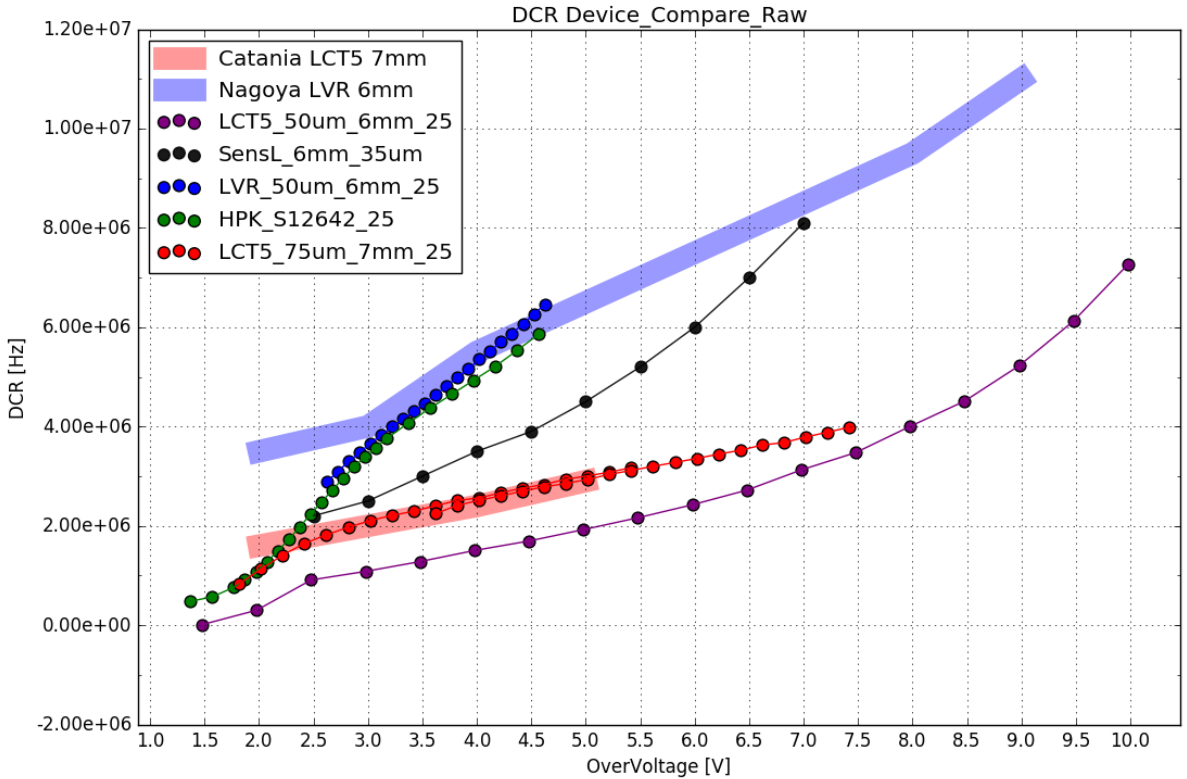


**Figure 48:** Dark Count Rate comparison of measured devices at 25°C. Description

against the full range measured by the external group, so the DCR for LVR 6mm must be labeled as not matching.

## 7.2 Optical Cross Talk

The comparison of the OCT between the different groups and the results presented in this work are dependent of the analysis and acquisition procedure. Extended trace analysis, utilized in this work captures all aspects of the OCT, prompt and delayed as well as afterpulsing. The procedure of time window analysis, utilized by the groups being compared to, are, due to their limited window, either biased towards the prompt cross talk or in extreme cases, will not be able to capture delayed cross talk or time-delayed afterpulsing at all. Comparing data analysis techniques, for example, at the University of Leicester is therefore a vital step. Their approach utilizes a pulsed laser as light source and involves no cooling of the SiPM tile. The waveforms are extracted from the scope and a small time window is defined from the known time position window of the incident pulse to search for peaks, find their value and generate a histogram. To the pulse area histogram, a theoretical model of contributing factors is fitted. This theoretical model simulates characteristics, updating continuously to find their correct values. Those values are the full set of characteristics of the device in testing, among them: gain curve, breakdown-voltage, OCT, PDE, noise, dynamic range, crosstalk probability.

There are a number of differences in their approach compared to the one utilized in this work,

most important is the time window size. If the window after an incident pulse is too short, data loss is a possibility, depending on the delay time of delayed cross-talk and afterpulsing assisted by traps with long lifetimes. This is a problem, especially with devices of the LCT5 generation implementing physical trenches isolating the cells and effectively reducing the prompt cross-talk, here the contribution from the prompt cross-talk to the overall OCT is lowered. Missing data from delayed cross-talk and afterpulsing, because it will not be recorded yet, would lead to errors in the overall OCT results being lower than expected.

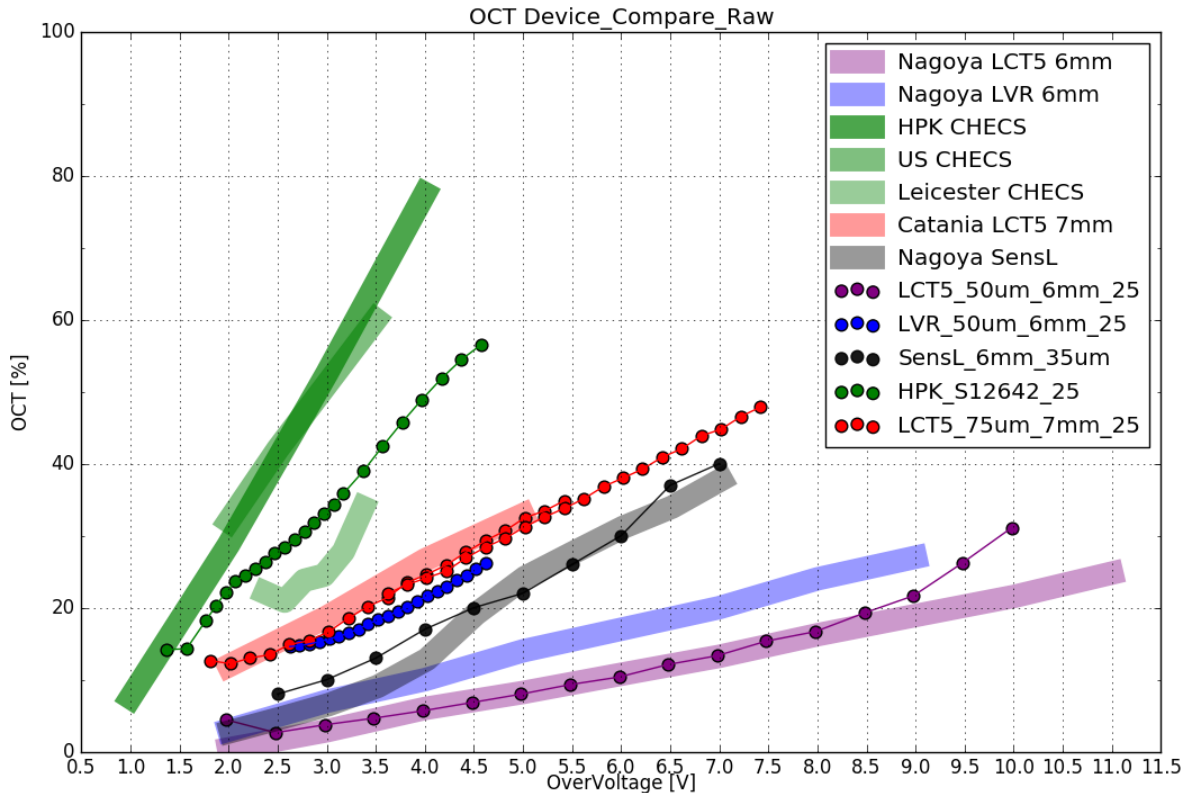


**Figure 49:** Cross Talk comparison of measured devices at 25°C. Description

This is indeed the case for the S12642 tile in figure(49)(green). The light green bar below (negative y-axis) the dotted data presented in this work shows the results from the University of Leicester indeed being lower. In purple results of the LCT5 S13360 device with physical trenches are shown. Compared to results from the University of Nagoya, there is a prominent upturn at around an over-voltage of  $\sim 8V$ . This could be due to the differences in analysis technique. The University of Nagoya also employs time window analysis.

LCT5 possesses lowered prompt cross-talk probability, so the contribution of delayed cross-talk to the overall cross-talk is higher than for S12642. With rising over-voltage the ratio between prompt and delayed cross talk shifts towards a higher contribution from delayed cross-talk[14][20]. While at lower over-voltages ( $\sim 0.5V$ ) the cross-talk is nearly entirely dominated by the prompt cross-talk with nearly no contribution of delayed cross-talk, at ( $\sim 2V$ ) contribu-

tions are mostly equal and at high over-voltages ( $\sim 7V$ ) the contribution of delayed cross-talk is expected to be above 80%, probably due to higher penetration depth and avalanche probability. Results of the LCT5 7mm device from both groups mostly overlap, the slight shift between them is most likely caused by a small error in the breakdown-voltage calculation, due to no cooling of the tile in experiments involving light. In addition, the slope of both results seems to be mostly equal, and the extended range measurement, overlapping with the low-range results confirms that.

Even though results from three different groups mostly correlate for four devices, or have at least partially understood differences, the OCT of LVR 6mm figure(49)(blue) compared to the results from the University of Nagoya do not show any correlation at all. This is concerning, because comparing S13360 (purple) to the same group showed strong correlation over a wide over-voltage range. Since there is also no datasheet present yet, this device is a prototype, the assumption is that the device examined is physically different than the device present at Nagoya. It may just be a difference in coating, which combined with the TSV technology could lead to the present uncorrelation[20].

### 7.3 Point of Operation Comparison

Device	Min. OCT			Max. PDE		
	OCT	DCR	PDE	OCT	DCR	PDE
CHECS	15%	0.5 MHz	25% (DS)	50%	5 MHz	48% (DS)
LCT5 6mm	15%	3.4 MHz	49% (Nagoya)	22%	5 MHz	51% (Nagoya)
LCT5 7mm	15%	2.0 MHz	42% (Catania)	25%	2.5 MHz	53% (Catania)
LVR 6mm	15%	2.5 MHz	43% (Nagoya)	>27%	>6MHz	>50% (Nagoya)
SensL	15%	3.0 MHz	37% (Nagoya)	30%	6 MHz	40% (Nagoya)

**Figure 50:** Comparison table of the measured devices based on the two proposed operation points for CHEC-S. First point represents minimal achievable OCT, second point represents maximum achievable PDE. PDE values taken from results of other groups and datasheet values. Note that the LCT5 6mm device can achieve even lower OCT values ( $\sim 3\%$  at  $V_{ov} = 2.5$ )

A different method of comparison involves the two proposed points of operation, illustrated at the beginning of section(7). By adding the PDE measured by external groups, all three characteristics can be illustrated together. Figure(??) shows the comparison result of the SiPMs examined in this work. A minimal OCT point of 15% in the left column, and the maximum PDE points in the right column, both include external PDE measurements.

At the first, minimal OCT, operation point the LCT5 6mm (S13360) device is favorable, since it possesses a high PDE of 49% with a fairly low DCR below the expected NSB. The currently used SiPM in CHEC-S only reaches 25% according to datasheet values.

The four HPK devices (the first four in the list), all have a maximum achievable PDE around the same level, ~50%. The difference in DCR and OCT at this level is the deciding factor. While the current CHEC-S SiPM reaches a very high OCT level of ~50%, the newer generation HPK SiPMs, with physical trenches, are well below at ~25%. The DCR on the other hand seems to be similar for each device. The LCT5 7mm SiPM at this point of operation seems to have the lowest DCR among them, but the measurements of this device have not yet reached the maximum PDE value and will be extended, higher PDE is possible.

In both cases, the low PDE of the SensL SiPM makes it not competitive.

---

## 7.4 Photon Detection Efficiency

---

The measurement technique in this work utilizes only dark counts and aims at giving an understanding of the OCT and temperature dependencies of the different SiPMs proposed, therefore no PDE measurements are possible. The point of operation with the highest PDE as well as the PDE versus OCT behaviour is determined by a different group in Japan, at the University of Nagoya. A figure showing the behavior of PDE versus OCT is the usual procedure of comparing SiPMs, it gives a correlated overview of the two most significant characteristics. This gives insight of the capabilities of the different devices compared to the two proposed points of operation in section(7.3). For consistency and to make comparison between group results easier, the PDE ascertained by the groups, of devices in common, compared to the resulting OCT from this work produces figure(51).

Comparing all devices at the two proposed points of operation produces the table in figure(50). This table together with figure(51) of the five measured devices in this work, where PDE data is accessible, is used to confirm results between groups and assist in the decision on the most viable SiPM for CHEC-S. The final decision will be taken by the GCT group based on measurements on substantially more devices (see section(H), for the complete list).

The PDE of SiPMs, when plotted versus the corresponding OCT at a common over-voltage point show the behaviour in figure(51). A clearly visible saturation after a certain OCT marks the point, from where an increase in power no longer increases photon-detection capabilities. An increase in OCT without rising PDE would have an adverse effect on the detectors resolution.

The prototype LCT5 7mm fig(51)(red) device reaches the highest PDE. This is expected for de-

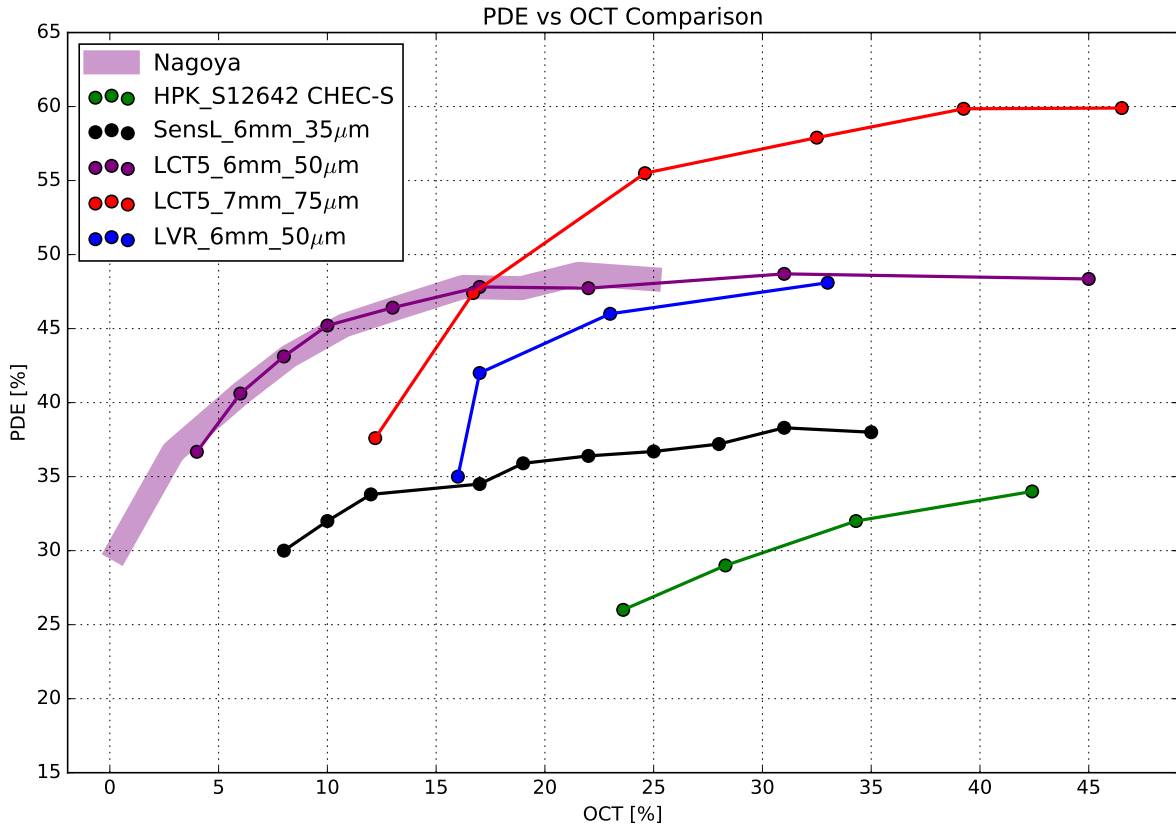


**Figure 51:** PDE results from the University of Nagoya parametrized with OCT results from this work, where available. PDE measurements at  $\lambda = 400\text{nm}$ . The faded purple bar shows an example measurement of the University of Nagoya. An optimum device for IACT application would be in the upper left region.

vices with larger cell-size and pixel-size, leading to a higher fill-factor. The increase in size and therefore PDE comes with a trade-off, increasing size comes with a rise of DCR and OCT, which are very high at this point (at  $\sim 25\%$ ).

The commercially available LCT5 6mm (HPK S13360) SiPM shows the most promising results. It reaches a high PDE very quickly compared to its OCT, with  $\sim 47\%$  before the OCT reaches 20%. Compared to this, the OCT of the LVR 6mm at a point where the PDE saturates and reaches the same PDE is very high.

The LCT5 6mm device seems the most promising for the low-OCT point, while the LCT5 7mm device would be the choice at the high PDE point. Being a fairly new technology, the LVR device is being developed and will be competitive.

Due to the low fill-factor, the PDE of the SensL FJ60035 device makes it not competitive. In conclusion, the HPK S12642 device is clearly sub-optimal for CHEC-S, but will still be used for initial tests. It shows a very low PDE compared to a very high OCT at this point.

---

## 8 Conclusion and Outlook

---

Over the course of this work five new-generation SiPMs have been examined in dark conditions, for their possible use in single photon detection for the high energy instrument of the Cherenkov Telescope Array.

A lasting experimental teststand has been developed, that is capable to be upgraded for future illumination tests. It is a reference to the involved groups, who will build similar setups to test the SiPMs for mass-production of the CHEC camera. The teststand involves a climate chamber for temperature regulation, that functions as a light tight box. For each SiPM pre-existent shaping electronics has been modified in order to achieve a preferred signal. Data acquisition code was developed to control the experimental parameters of the teststand remotely, and storing all experimental data from the internal memory of the oscilloscope on a Lab-PC. A data analysis procedure has been designed and developed to analyze the data offline, both were developed in python. The analysis method showed performance issues with measurements of devices at higher OCT levels. Illumination tests will make it easier to reach lower over-voltage ranges, due to the lower dependency of dark counts with low gain, that is characteristic in that region.

Experimental studies of the SiPMs showed better performance at lower temperatures. In observation conditions, temperatures lower than 25 °C are unfortunately not expected. Even at those temperatures SiPMs are a strongly considered candidate. For the examined devices, the temperature dependence of the dark noise and the gain has been studied.

By now, only dark measurements can be conducted, but once a tunable lightsource and monochromator is installed, light measurements are possible. Before that, a solution for the potential warm-up of the SiPM surface must be found.

The work on both, the teststand and the analysis method, will be expanded in the future. Following this work the involved groups start to exchange the physical devices for better coverage of the measured characteristics.

For part of the measured devices, strong correlations between the involved groups have been found, the other part contained discrepancies, that are only in part understood. The exchange of physical devices will clarify the source.

Comparing the devices measured in this work showed the LCT5 generation to be favorable for both proposed points of operation of CHEC-S. There is a new technology, LVR, that is promising and still being developed.

---

## **9 Glossary**

---

1. IACT - Imaging Atmospheric Cherenkov Telescope
2. VHE - Very High Energy
3. CTA - Cherenkov Telescope Array
4. LST - Large Sized Telescope
5. MST - Medium Sized Telescope
6. SST - Small Sized Telescope
7. GCT - Gamma Cherenkov Telescope
8. CHEC - Compact High Energy Camera (CHEC-M based on MAPMs, CHEC-S based on SiPMs)
9. SiPM - Silicon Photomultiplier
10. MAPM - Multi Anode Photomultipliertubes
11. p.e. - photoelectron
12. DCR - Dark Count Rate
13. OCT - Optical Cross Talk
14. PDE - Photon Detection Efficiency
15. HPK - Hamamatsu Photonics K.K.
16. SensL - Sense Light
17. LCT - Low Cross Talk
18. LVR - Low Voltage Range

---

## 10 Bibliography

---

### References

---

- [1] Jim Hinton et al. *Teraelectronvolt Astronomy* Ann. Rev. Astron. Astrophys., 47:523
- [2] The CTA Consortium *Design Concepts for the Cherenkov Telescope Array CTA, An Advanced Facility for Ground-Based High-Energy Gamma-Ray Astronomy* ; arXiv:1008.3703v3 [astro-ph.IM] 11 Apr 2012
- [3] Teresa Montaruli et al. *The small size telescope projects for the Cherenkov Telescope Array* arXiv:1508.06472v1 [astro-ph.IM]
- [4] *The ASTRONET Infrastructure Roadmap* ISBN: 978-3-923524-63-1
- [5] Jim Hinton et. al *Seeing the High-Energy Universe with the Cherenkov Telescope Array* Astroparticle Physics 43 (2013) 1-356
- [6] R. López-Coto for the HAWC collaboration *Very high energy gamma-ray astronomy with HAWC* arXiv:1612.09078v1 [astro-ph.IM] 29 Dec 2016
- [7] John Murphy *SensL J-Series Silicon Photomultipliers for High-Performance Timing in Nuclear Medicine*
- [8] A. N. Otte et al. *Characterization of three high efficient and blue sensitive Silicon photomultipliers* arXiv:1606.05186v2 [physics.ins-det] 26 Jan 2017
- [9] A. Bouvier et al. *Photosensor Characterization for the Cherenkov Telescope Array: Silicon Photomultiplier versus Multi-Anode Photomultiplier Tube* ; arXiv:1308.1390v1 [astro-ph.IM] 6 Aug 2013
- [10] V. Vassilieva , S. Fegan *Wide field aplanatic two-mirror telescopes for ground-based gamma-ray astronomy* Astropart. Phys. 28 (2007) 10, [astro-ph/0612718] arXiv:astro-ph/0612718v2 12 Apr 2007
- [11] A. Zech, J.-P. Amans, S. Blake et al. *SST-GATE: A dual mirror telescope for the Cherenkov Telescope Array* arXiv:1307.3035v1 [astro-ph.IM] 11 Jul 2013
- [12] Julien Rousselle et al. *Construction of a Schwarzschild-Couder telescope as a candidate for the Cherenkov Telescope Array: status of the optical system* arXiv:1509.01143v1 astro-ph.IM
- [13] J. Rosado S. Hidalgo *Characterization and modeling of crosstalk and afterpulsing in Hamamatsu silicon photomultipliers.* arXiv:1509.02286v2 [physics.ins-det] 21 Oct 2015
- [14] K. Boone, Y. Iwai, F. Retiere, C. Rethmeier *Delayed avalanches in Multi-Pixel Photon Counters* arXiv:1703.04651v1 [physics.ins-det] 14 Mar 2017

- 
- [15] Robert G. Wagner et al. *The Next Generation of Photo-Detectors for Particle Astrophysics* arXiv:0904.3565v1 [astro-ph.IM] 22 Apr 2009
- [16] *Opto-semiconductor handbook Chapter 03 Si APD, MPPC*. Hamamatsu Photonics K.K.
- [17] Jonathan Biteau et al *Performance of Silicon Photomultipliers for the Dual-Mirror Medium-Sized Telescopes of the Cherenkov Telescope Array* arXiv:1508.06245v1 [astro-ph.IM] 25 Aug 2015
- [18] Richard White *private communication*. 2017
- [19] Hiro Tajima *private communication*. 2017
- [20] Koei Yamamoto *private correspondence*. 2016
- [21] Luigi Tibaldo *Initial testing at MPIK (wb July 18 2016)* July 2016
- [22] T. C. Awes et al. *Configurable electronics with low noise and 14-bit dynamic range for photodiode-based photon detectors* Nuclear Inst. and Methods in Physics Research, Mai 2006
- [23] Maurice Stephan. *Design and Test of a Low Noise Amplifier for the Auger Radio Detector* Diploma Thesis, RWTH Aachen University, July 2009
- [24] [http://astro.desy.de/gamma\\_astronomy/cta/index\\_eng.html](http://astro.desy.de/gamma_astronomy/cta/index_eng.html)
- [25] <http://www.ung.si/en/research/laboratory-for-astroparticle-physics/projects/cta/>
- [26] <http://www.ung.si/en/research/laboratory-for-astroparticle-physics/projects/fermi-lat/>
- [27] [http://212.71.251.65/aspera//index.php?option=com\\_content&task=blogcategory&id=111&Itemid=234](http://212.71.251.65/aspera//index.php?option=com_content&task=blogcategory&id=111&Itemid=234)

## 11 Appendix

### A CTA

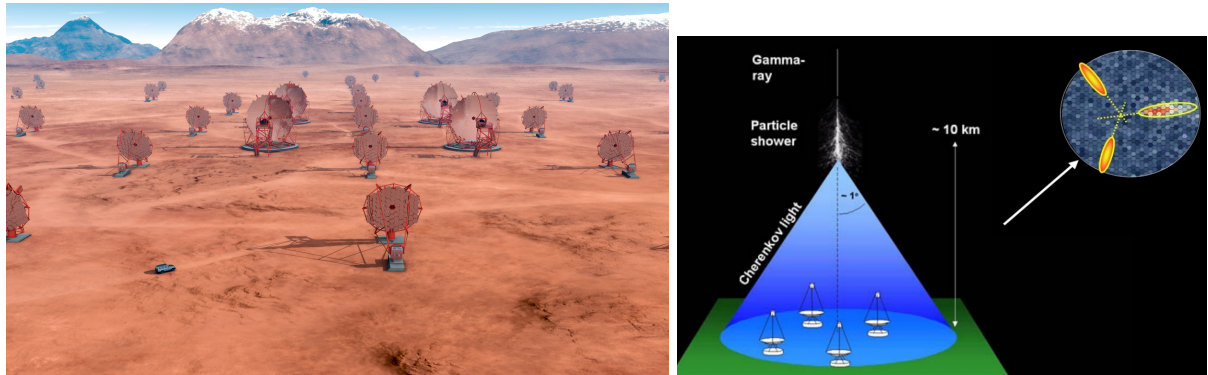


**Figure 52:** A render of the finished CTA Array at the site in Chile (left) with visible LSTs and MSTs, and the Shower Path Reconstruction technique of the stereoscopic view employed by current IACT experiments like HESS, MAGIC, VERITAS (right).

### B progenitor experiments of CTA



**Figure 53:** IACT Projects: HESS in the Khomas Highland, Namibia. MAGIC at the Roque de los Muchachos Observatory on La Palma , one of the Canary Islands. VERITAS at Mount Hopkins, Arizona, USA

## C OCT dependency on cellsize

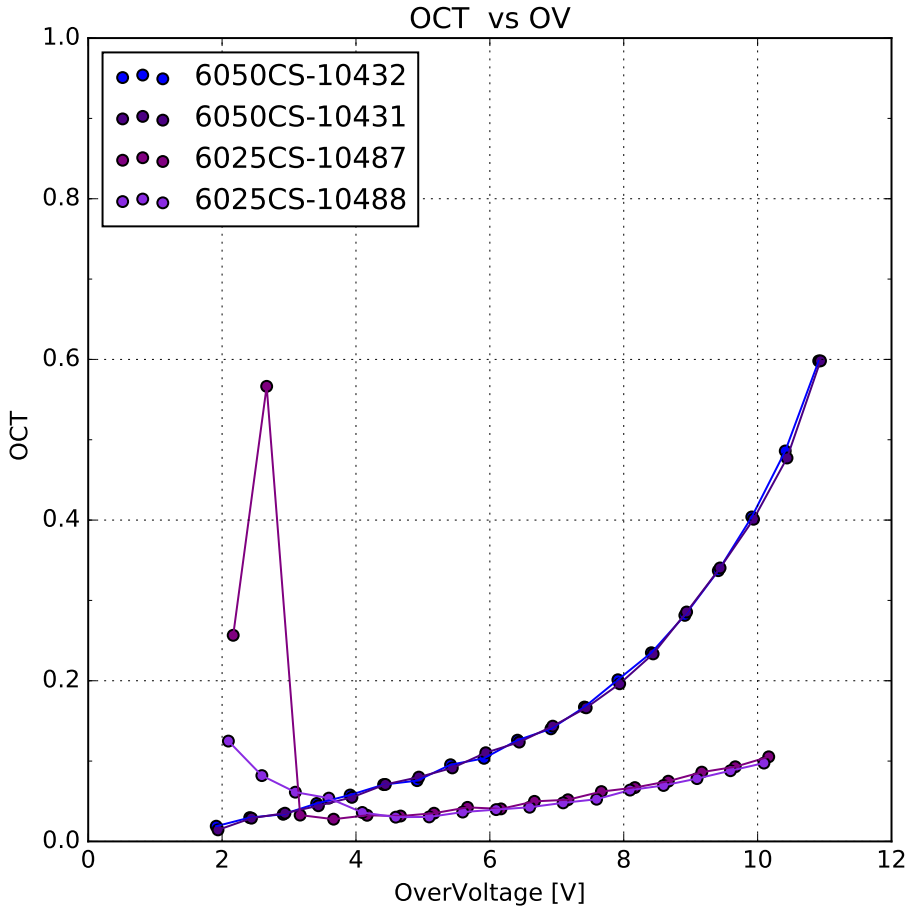


**Figure 54:** Results of the OCT of two sets of two similar HPK S13360 devices, that only differ in their respective cell-size. HPK S13360 is the first device incorporating physical trenches in the upper layer, optically isolating each cell. Consequence to this is a drastic reduction in prompt cross-talk. Delayed cross-talk and afterpulsing are basically unaffected. Upscaling of the  $25\mu\text{m}$  results shows an overlap between the two, see text.

In figure(54) the results of the complete OCT of two sets of  $50\ \mu\text{m}$  and  $25\mu\text{m}$  HPK S13360 devices are shown. Plotting the results of two similar devices, only different in their cell-size, and then multiplying the  $25\ \mu\text{m}$  results by the factor derived from their difference in area, here  $\times 4$ , a correlation is visible. Scaling up the OCT of the  $25\ \mu\text{m}$  cell, shows an overlap between the two cell-sized pixels. This means, that the OCT is directly area and therefore cell-size dependent. Research by J. Rosado and S. Hidalgo [13] on the cross-talk probability of Hamamatsu SiPMs showed through Monte Carlo simulation, that the prompt crosstalk mostly takes place in a small area of pixels ( $\sim 8$ ) around the primary one. Which means, that the cross-talk is directly increasing with increasing cell-size, or in other words: with chance to diffuse to a neighboring cell. Small cells reduce the chance, as there is less area to a neighboring cell to pass through. Since the measurements conducted in this work do not differ between the range of secondary

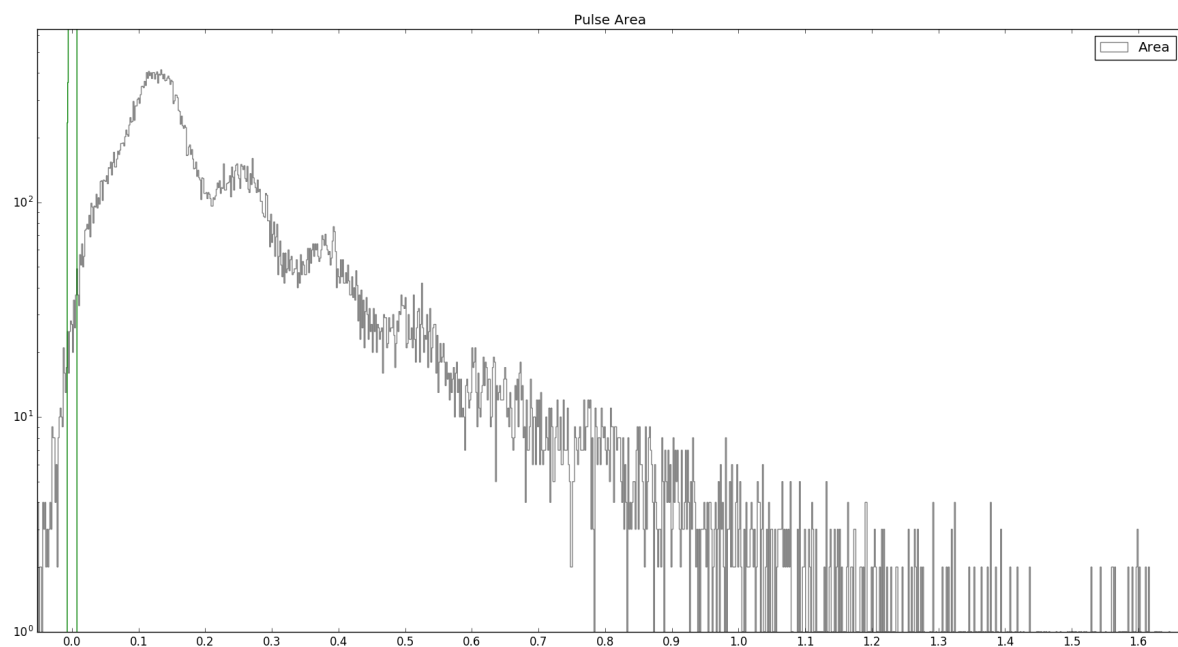
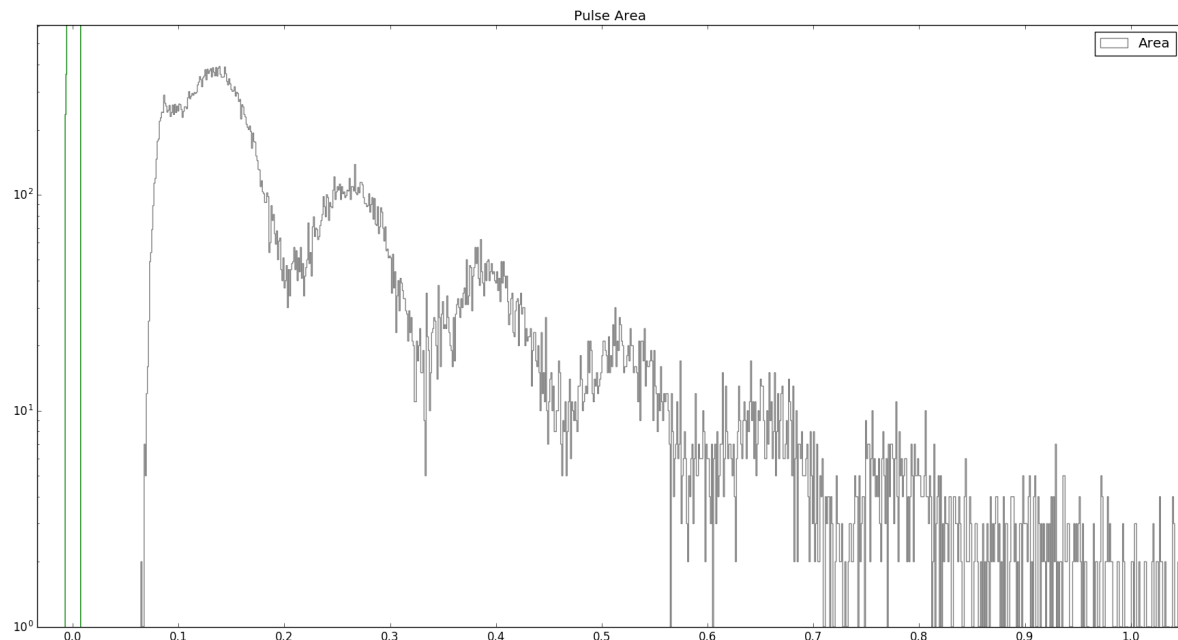
---

avalanche effects, the OCT shown contains every aspect, prompt and delayed as well as after-pulsing.

---

## D Pulse Area Spectra of different integration window widths

---



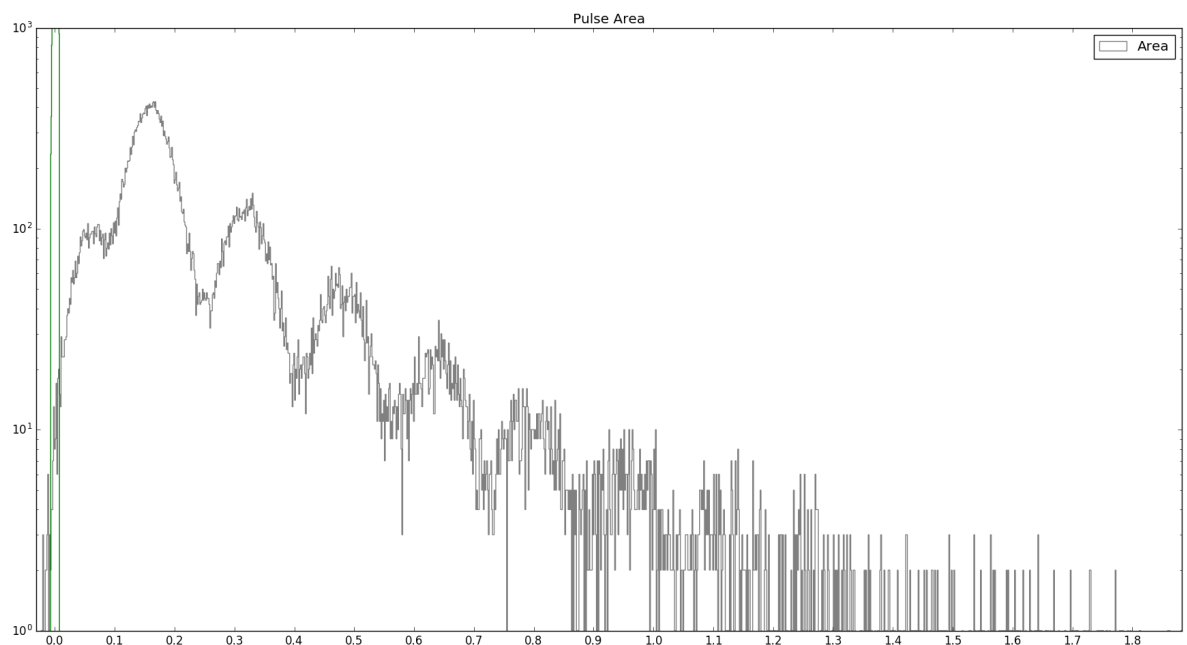


**Figure 55:** Pulse Area Spectra with window widths of 5 left 5 right (top), 5 left 20 right (middle), 10 left 10 right (bottom) bins respectively. Left of the 1p.e. peak of the top picture a part of the 0p.e. peak is visible. The middle figure shows the distortion an asymmetrical integration window causes. The bottom figure is the employed integration window to derive the pulse area histogram.

## E Pulse Area Spectra examples

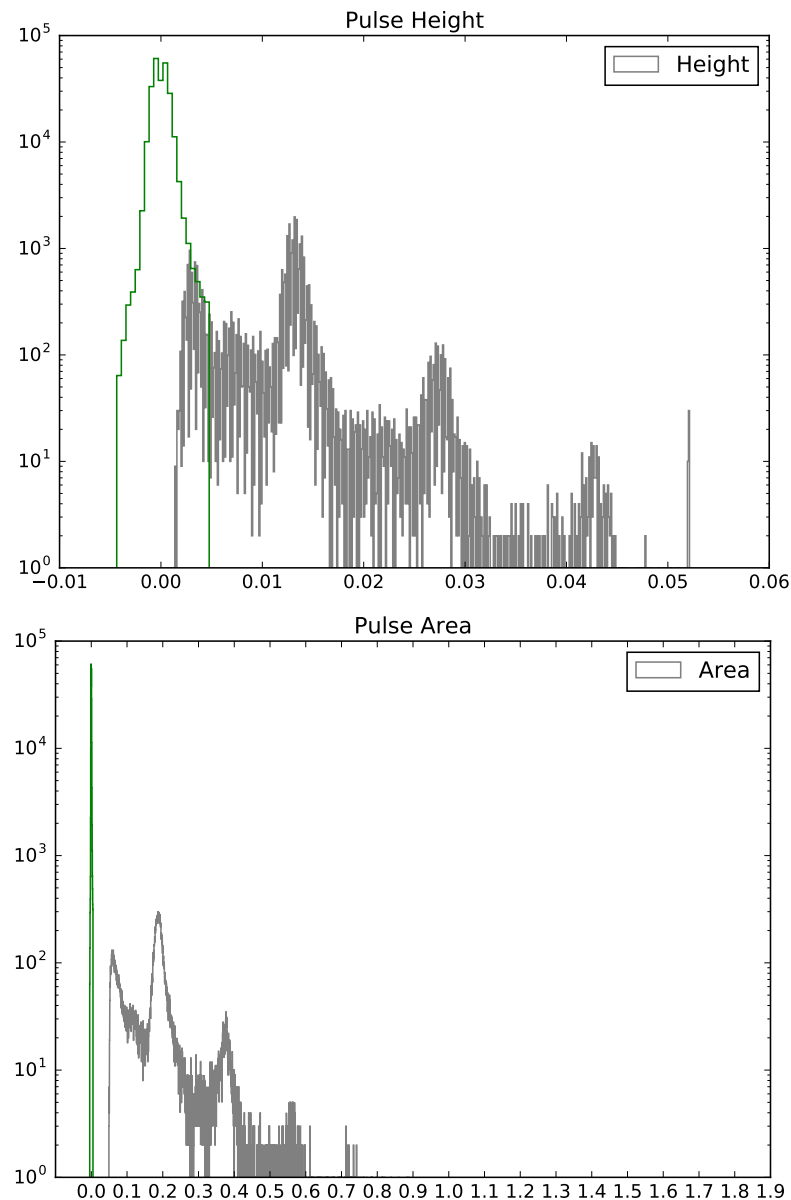


**Figure 56:** Pulse height and pulse area spectrum of the S12642 device at  $V_b = 58V$  and  $T = 25^\circ C$ . The x-axis is pulse height and pulse area respectively and the y-axis is number of counted pulses

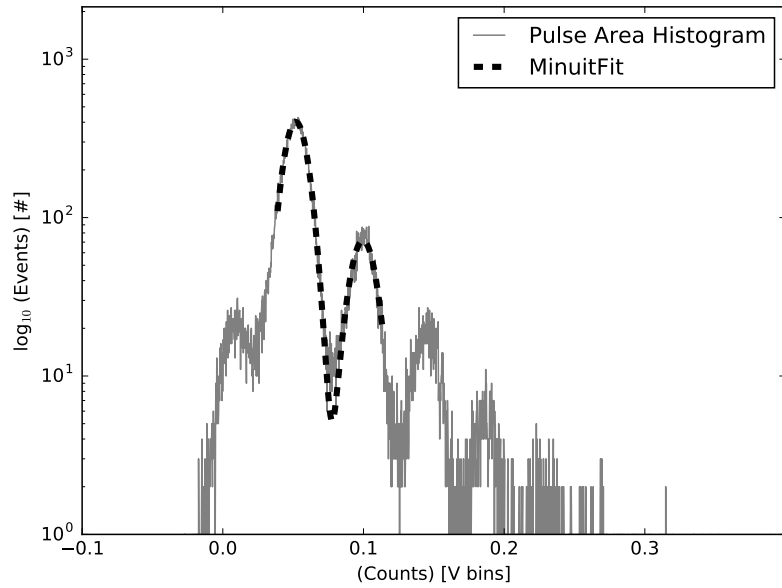


**Figure 57:** Pulse area spectrum of the S13360 LCT5 6mm device at  $V_b = 56.2\text{V}$  at  $T = 25^\circ\text{C}$ . The x-axis is pulse height and pulse area respectively and the y-axis is number of counted pulses. The dashed black line shows the fitted function.

## F BreakdownVoltage

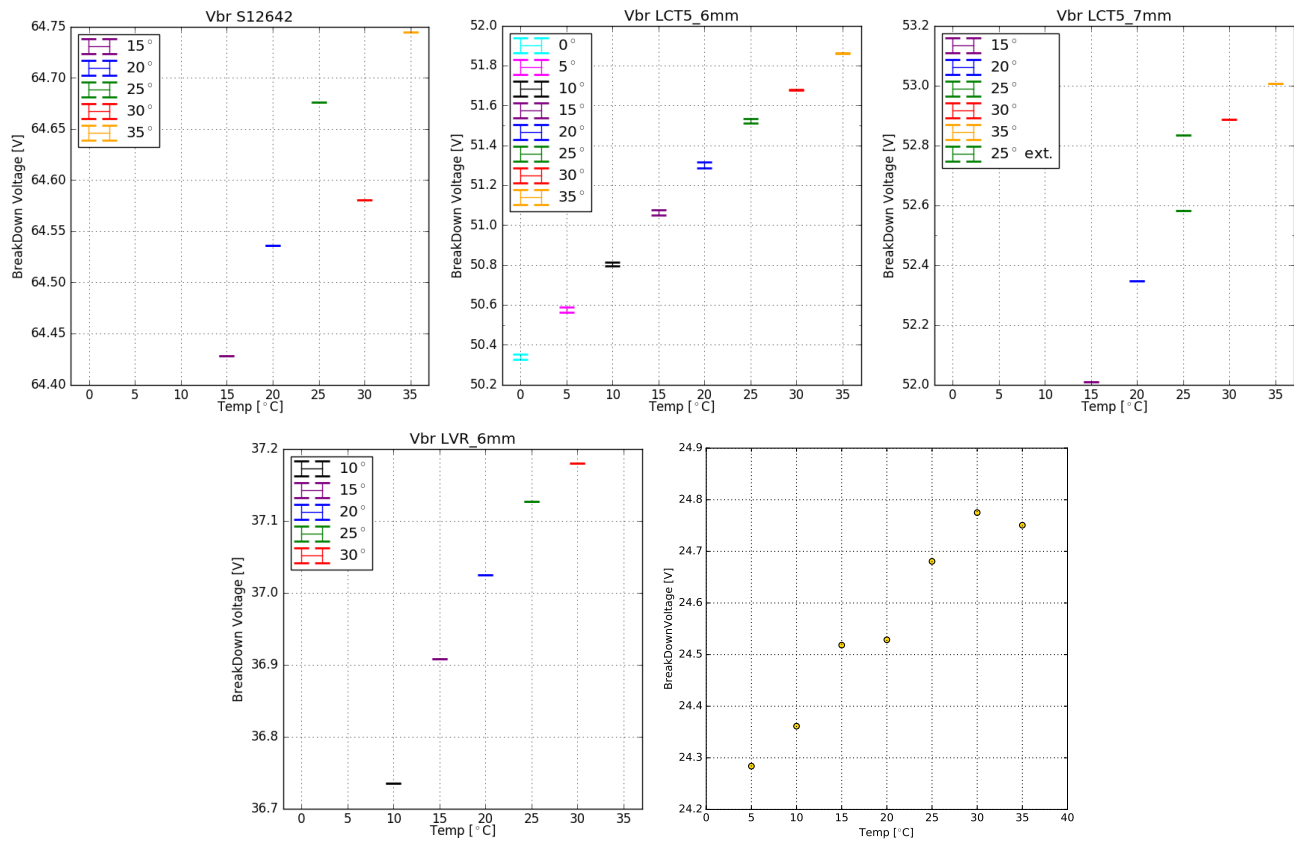


**Figure 58:** Dependency of the breakdown-voltage of temperature for the 5 measured devices.

For LCT5 7mm , the extended range measurement adds an extra datapoint at 25 °C  
 HPK S12642 (CHEC-S) (top left) ; HPK LCT5 6mm (top middle) ; HPK LCT5 7mm (top right) ; HPK LCT5 LVR 6mm (bottom left) ; SensL FJ60035 (bottom right).

Device	$\Delta V / T$ [mV/°C]
CHECS	$13.1 \pm 4.1$
LCT5 6mm	$43.5 \pm 0.4$
LCT5 7mm	$53.0 \pm 4.0$
LVR 6mm	$25.6 \pm 2.6$
SensL	$15.0 \pm 1.1$

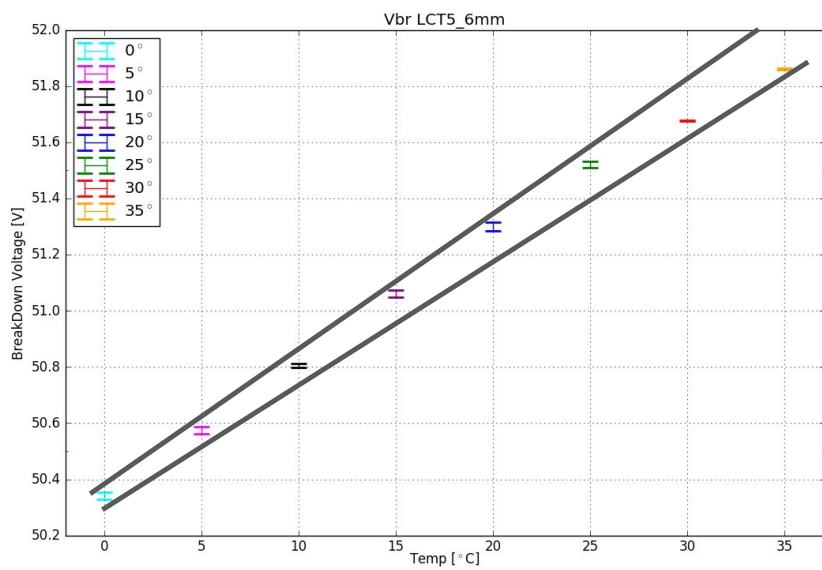


**Figure 59:** The extracted breakdown-voltage dependence of all measured devices, derived from two regression lines and their mean. For some devices the breakdown-voltage dependency is known through datasheet values. S12642 = 60 mV/°C, S13360 = 54 mV/°C, SensL FJ60035 =<21.5 mV/°C

## G Shaper

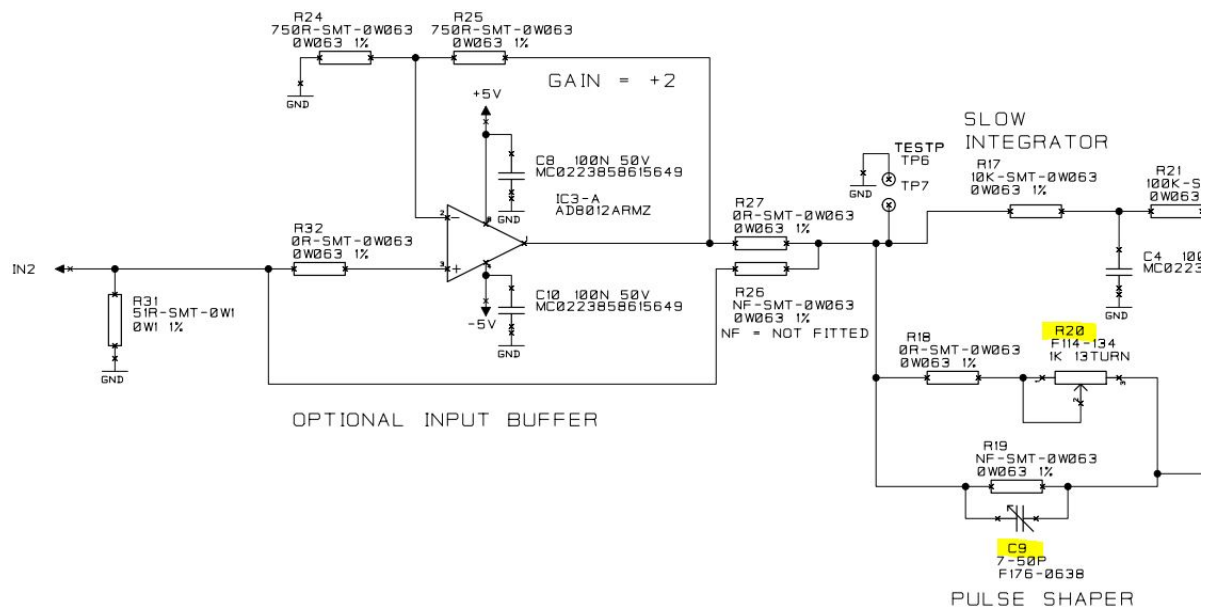


**Figure 60:** Full schematic of the shaper developed at the University of Leicester. With tuneable components C9 and R20 highlighted.

## H SiPM list tested at University of Nagoya

Manufacturer	pixel size [mm]	cell size [μm]	technology	coating
HPK S12642-1616PA-50 *CHEC-S SiPM	3	50	standard	silicon
HPK LCT5 S13360-6050CS	6	50	LCT5	silicon
HPK LCT5 6.975MM-SIL Single	6.915	75	LCT5	silicon
HPK 6050HWB-LVR-LCT	6	50	LVR	silicon
SensL FJ60035	6	35	TSV	glass
HPK S12572-050C	3	50	standard	silicon
HPK S13360-3050CS	3	50	LCT5	silicon
HPK S13360-3050VE	3	50	LCT5	epoxy
HPK S13360-3075CS	3	75	LCT5	silicon
HPK S13360-6075CS	6	75	LCT5	silicon
HPK LVR-3050CS	3	50	LVR	silicon
HPK LVR-6050CS	6	50	LVR	silicon
HPK LVR-6075CS	6	75	LVR	silicon
FBK NUV (reference device)	6	30	NUV	?
HPK LVR-S-50-3	3	50	LVR	silicon
HPK LVR-S-50-6	6	50	LVR	silicon
HPK LVR2-S-50-6	6	50	LVR 2	silicon
HPK LVR2-N-50-6	6	50	LVR 2	none
HPK LVR2-S-50-7	7	50	LVR 2	silicon

**Figure 61:** List of SiPM device candidates for CHEC-S measured by involved groups. \*(LCT5: Low Cross Talk 5th iteration , LVR: Low Voltage Range , TSV: through silicon via , LVR2: Low Voltage Range 2nd iteration , standard: no trenches) [19]

## I CHEC-S pixel comparison

Comparison of results from 10 different pixels on the CHEC-S (HPK S12642-1616PA-50) array. Every pixel is analyzed with the same technique and analysis parameters.

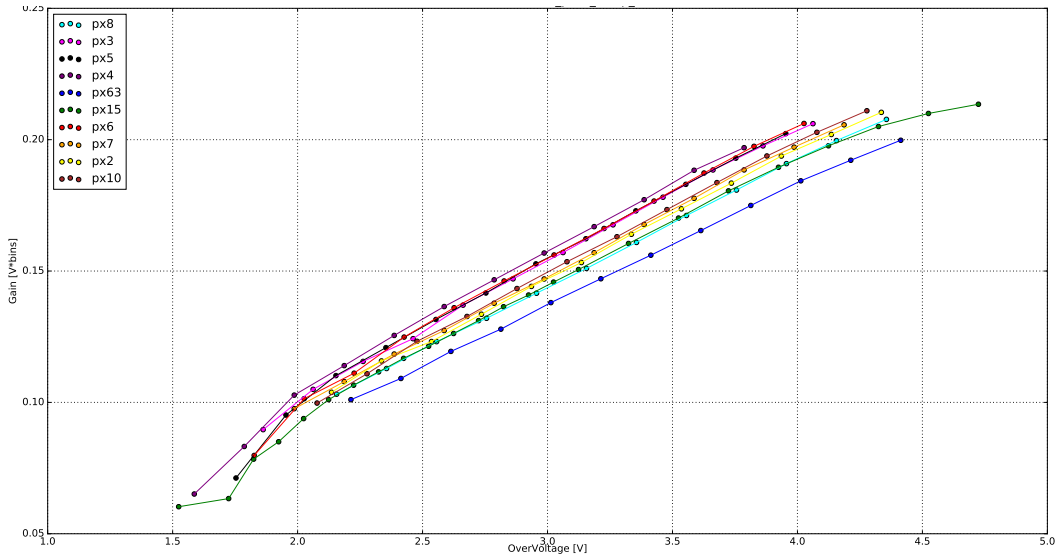


**Figure 62:** Gain comparison of 10 different pixels of the CHEC-S (HPK S12642-1616PA-50) array

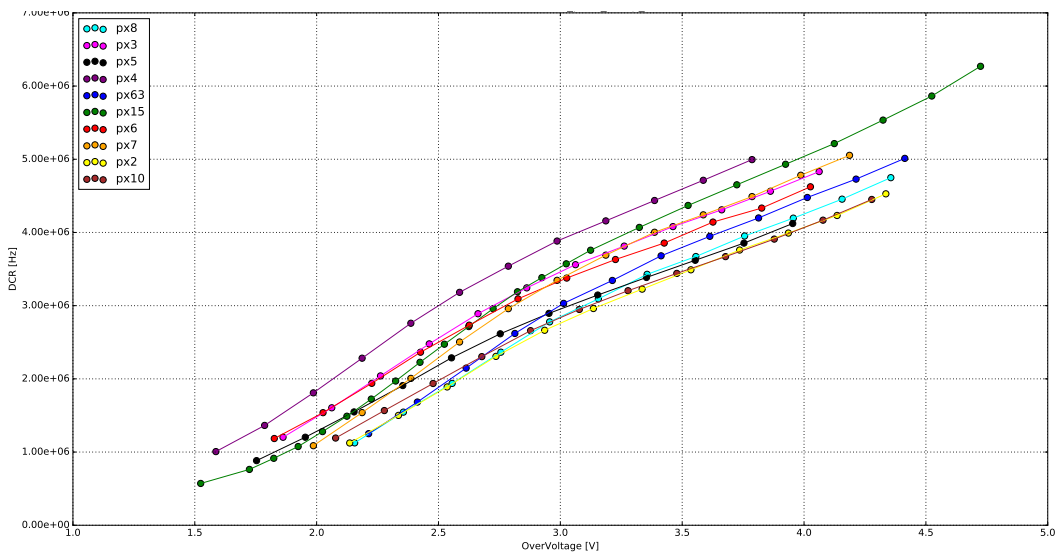


**Figure 63:** DCR comparison of 10 different pixels of the CHEC-S (HPK S12642-1616PA-50) array

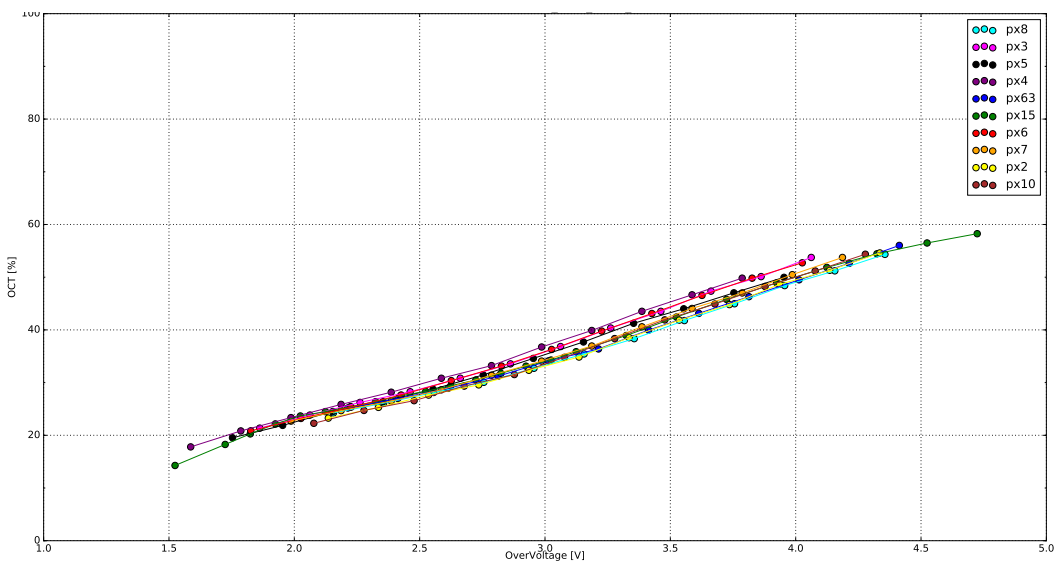


**Figure 64:** OCT comparison of 10 different pixels of the CHEC-S (HPK S12642-1616PA-50) array

---

## J Additional Data Analysis Plots

---

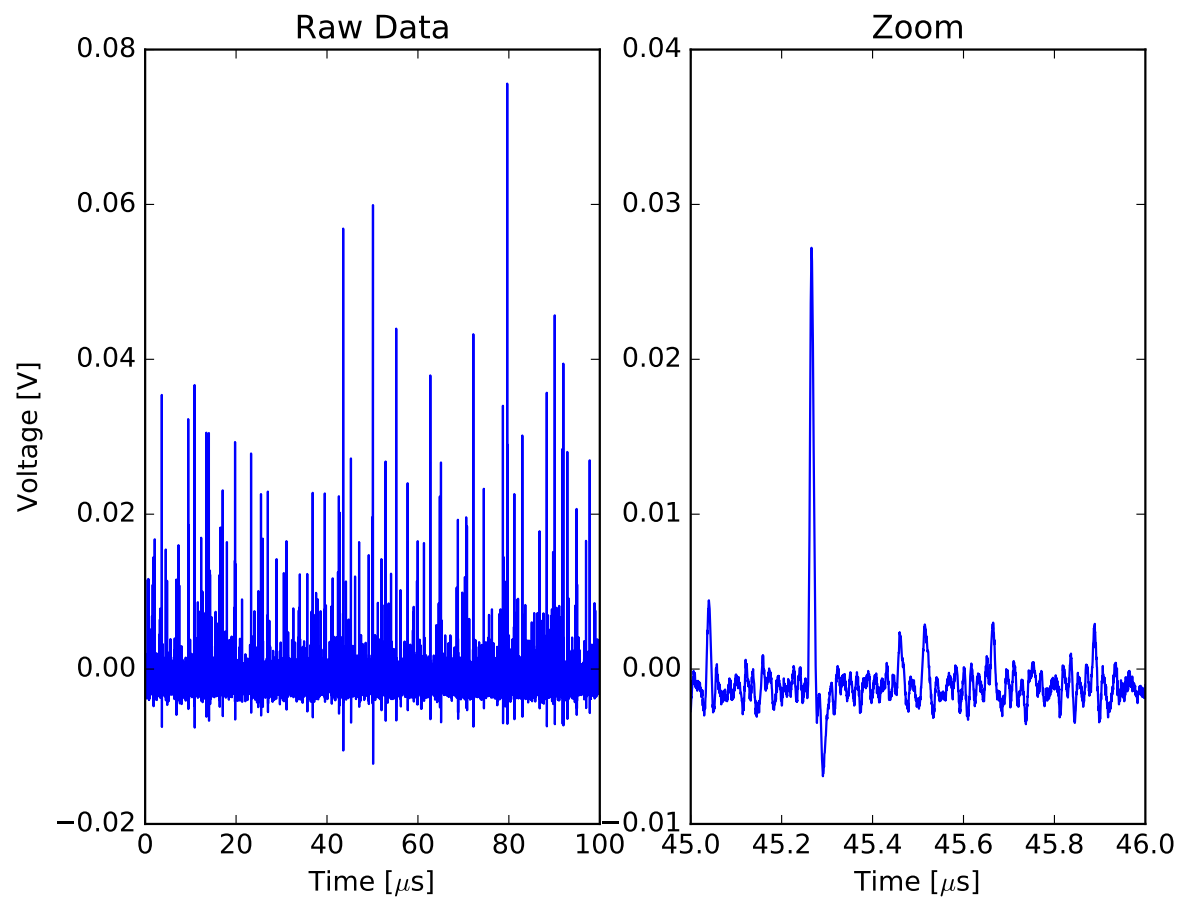


**Figure 65:** Raw data from the oscilloscope, converted, but no analysis steps taken.

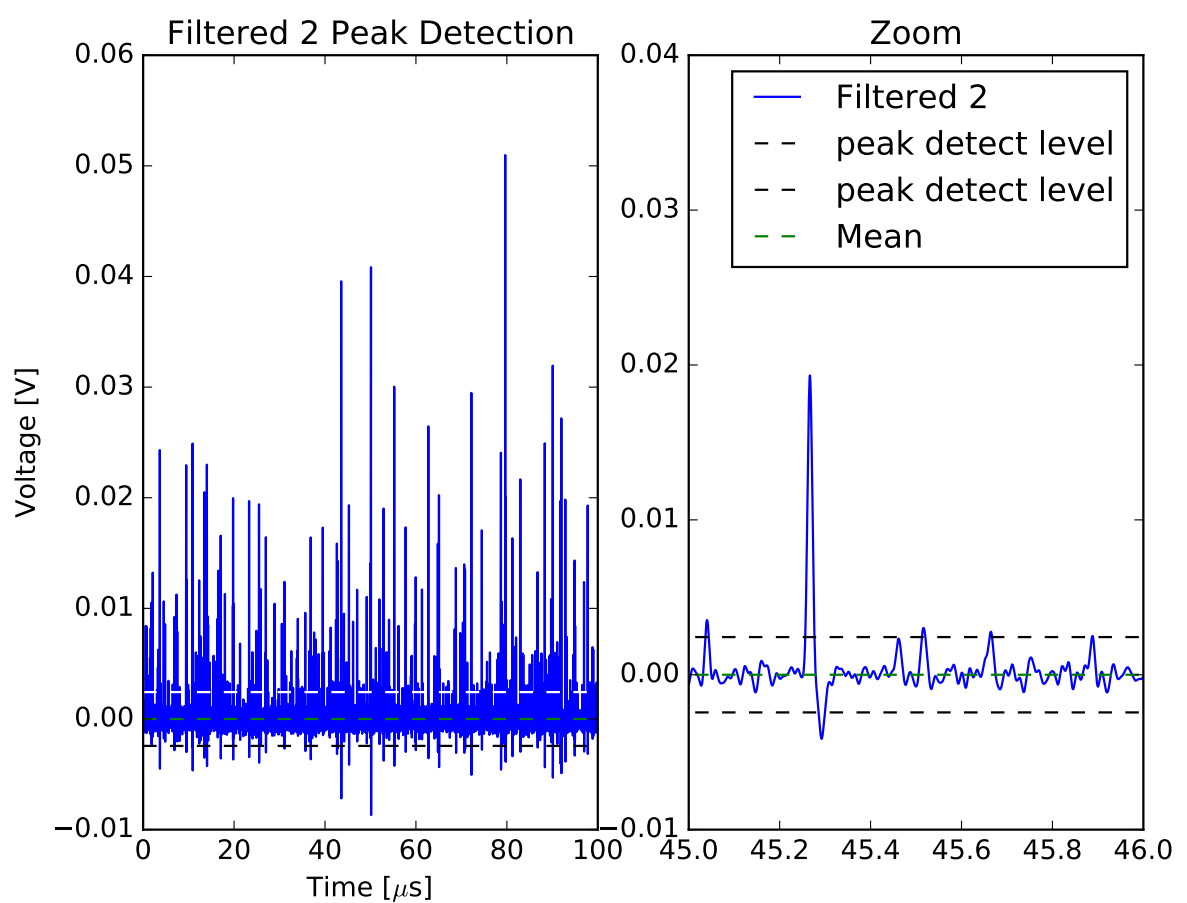


**Figure 66:** Peak detection level visible on filtered signal 2.

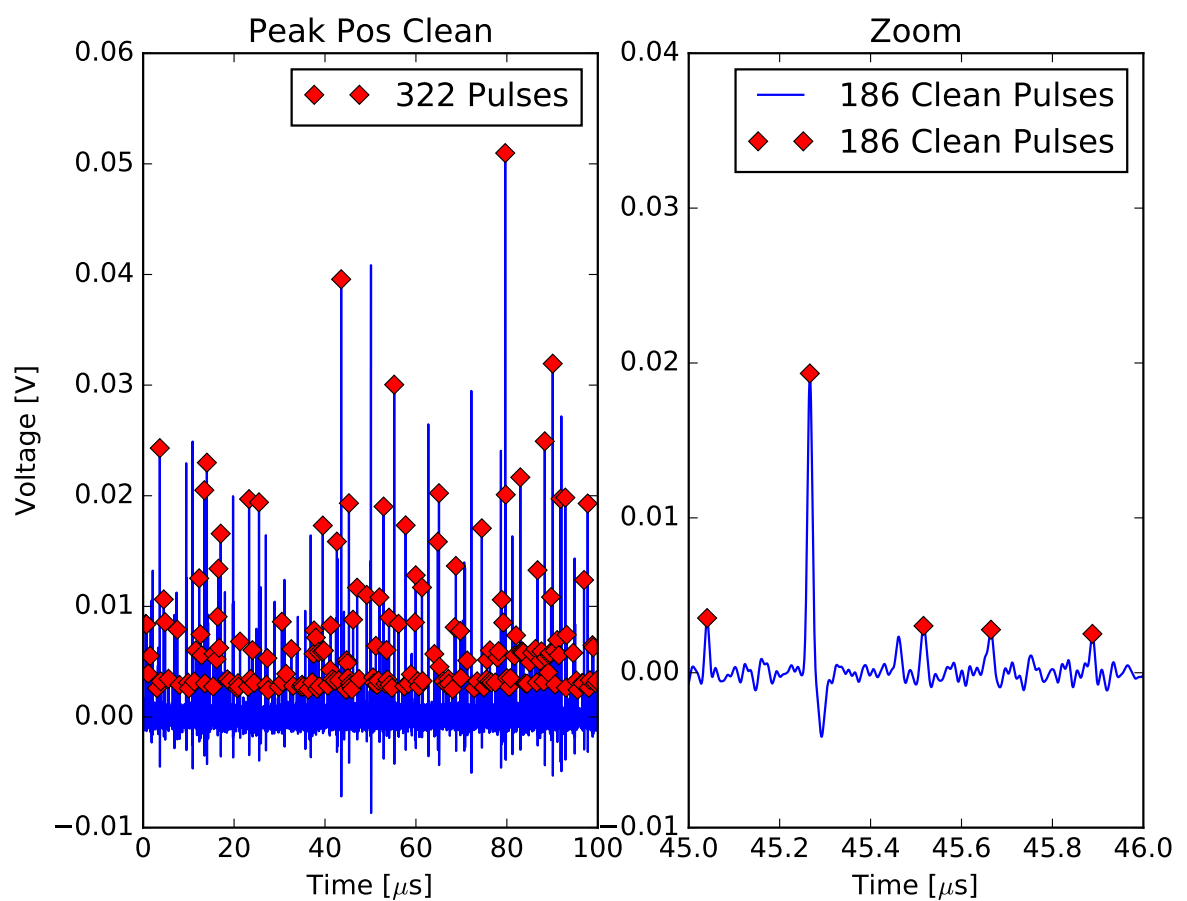


**Figure 67:** Number of peaks detected, clean keyword is to check for peak proximity.

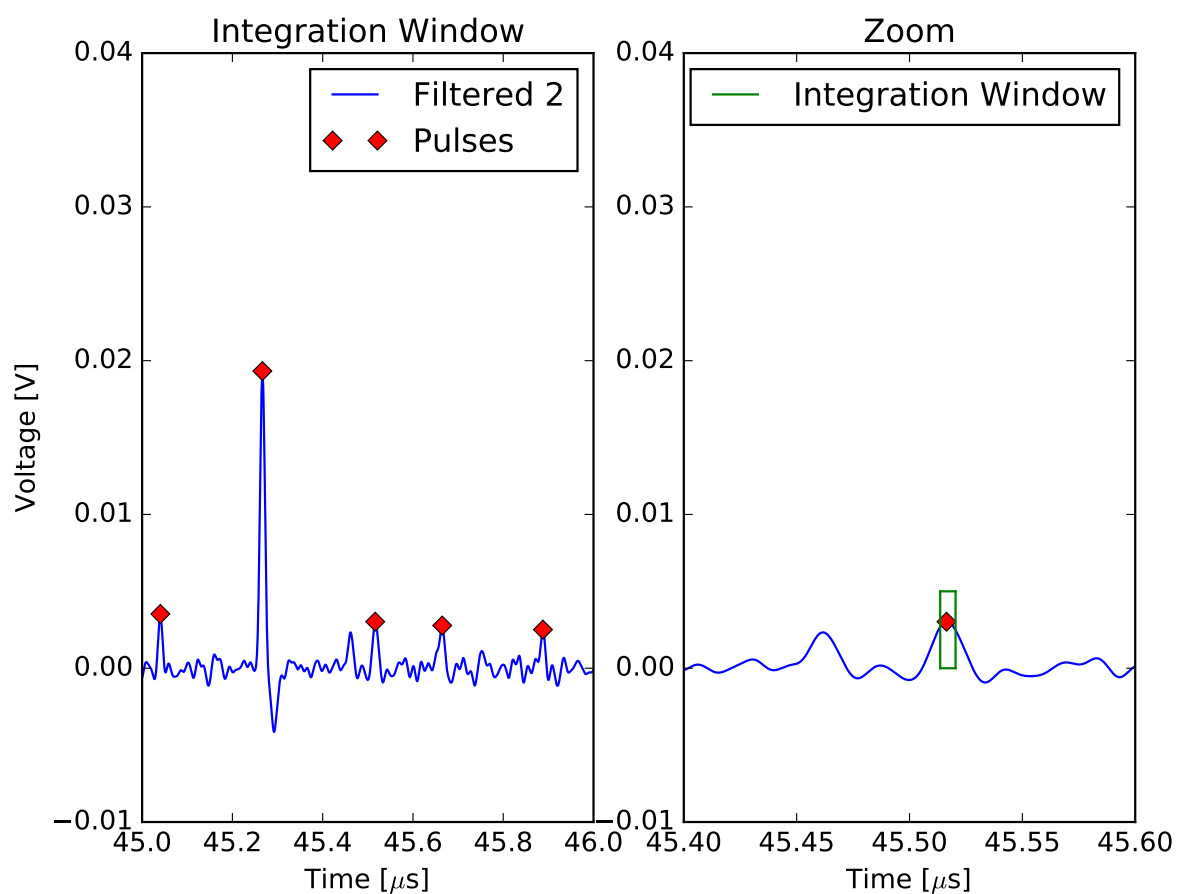


**Figure 68:** Illustration of an integration window applied to the pulse.

---

## K Multi incident probability and Optical Cross Talk

---

With increasing DCR the probability of two dark events happening at the same time rises with increasing bias-voltage. This has an effect on the calculated OCT. In the event of two 1p.e. pulses coinciding with each other, they could be misinterpreted as one dark incident and it's cross-talk. Taking, for example, the DCR of S13360, 4 MHz at  $V_{ov} = 8V$  and  $T = 25^\circ C$ , with the FWHM of the characteristic pulse as 5.6 ns we can calculate the probability of two coinciding pulses as  $\sim 2.2\%$ . This probability has a direct effect on the calculated OCT (eq:7), in reducing it compared to the calculation. It was stated as to high, due to the labeling of the second incident actual dark event as cross-talk. The OCT at this point is only  $\sim 17\%$ , but a  $\sim 2.2\%$  shift of the number of events  $N_{events(\geq 1.5p.e.)}$  to  $N_{events(\geq 0.5p.e.)}$  lowers the OCT by  $\sim 0.75\%$ . Even though the multi hit coincidence is low, this shows that there are analysis related problems with high DCRs.

For devices with high DCR and OCT like S12642 this effect grows in magnitude. At only  $V_{ov} = 4.5V$  at  $25^\circ C$  the DCR is 6 MHz. With the pulse FWHM of 9 ns this leads to a coincidence of 5.4%. The OCT at that point is 55%, so a reduction of 5.4% of the  $N_{events(\geq 1.5p.e.)}$  towards the  $N_{events(\geq 0.5p.e.)}$  leads to a reduction of the OCT by 5.6%.

This is an extreme case, where the peak positions of the two dark events are separated by their FWHM length, in reality every overlap window is possible.

---

# **Erklärung zur Master-Thesis**

Hiermit versichere ich, die vorliegende Master-Thesis ohne Hilfe Dritter nur mit den angegebenen Quellen und Hilfsmitteln angefertigt zu haben. Alle Stellen, die aus Quellen entnommen wurden, sind als solche kenntlich gemacht. Diese Arbeit hat in gleicher oder ähnlicher Form noch keiner Prüfungsbehörde vorgelegen.

Darmstadt, den April 27, 2017

---

(B. Gebhardt)